INFLUENCE OF OXYGEN FLOW ON THE MICROSTRUCTURE, RESISTIVITY, AND FARADAY ROTATION OF REACTIVE RF SPUTTERED NIO AND FE-DOPED NIO THIN FILMS.

by

Md Abdul Ahad Talukder, B.S.

A thesis submitted to the Graduate Council of
Texas State University in partial fulfillment
of the requirements for the degree of
Master of Science
with a Major in Materials Physics
December 2017

Committee Members:

Wilhelmus J. Geerts, Chair

Mark Holtz

Ravi Droopad

FAIR USE AND AUTHOR'S PERMISSION STATEMENT

Fair Use

Duplication Permission

ACKNOWLEDGEMENTS

I would like to thank Dr. Wilhelmus Geerts for guiding me during my thesis research. I'm thankful to the undergraduate students Brian Collier and Chandler Hutton for helping me with Magneto-Optical and Electrical characterization. Furthermore Drs. Mark Holtz and Ravi Droopad are thanked for serving on my thesis committee. Shane Arabie of Engineering Technology is acknowledged for help with machine-shop tasks. Furthermore, I would like to thank Dr. Casey Smith, Dr. Dimitry Layshanko and Peter Walker for training and helping me with solving the instrumental problems.

This work was supported by a DOD grant (HBCU/MI grant W911NF-15-1-0394) and by a thesis support fellowship from the graduate college.

Part of this thesis was published in the following conference proceeding and journal articles:

[1] Md. Abdul Ahad Talukder, Wilhelmus J. Geerts, "Tilt angle dependence of the modulated interference effect in Photo-elastic Modulators", AIP Advances, vol. 7, 056719 1-4, 2017; doi: 10.1063/1.4975999.

[2] Md. Abdul Ahad Talukder, Wilhelmus J. Geerts, "Jones matrix description of Fabry-Perot interference in a single axis photoelastic modulator and the consequences for the

magneto-optical measurement method", AIP Advances 7, 085320 (2017); https://doi.org/10.1063/1.4999517.

Part of this thesis was presented at the following conferences:

[1] Md Abdul Ahad Talukder**,** Yubo Cui, Wilhelmus J. Geerts, Study of the Crystal Properties of Iron Doped NiO using an X-ray Diffractometer, oral presentation at the 7th international research conference for graduate students, Texas State University Nov. 17-18, 2015.

[2] Md Abdul Ahad Talukder, Wilhelmus J. Geerts, "Tilt angle dependence of the modulated interference effect in Photo-elastic Modulators", poster presentation MMM conference October 2016, New Orleans.

[3] Md Abdul Ahad Talukder, Wilhelmus J. Geerts, "Interference effects in Photo-elastic modulator when using highly coherent light", oral presentation at the Fall-2016 Joint meeting of the four corners and Texas Sections of the American Physical Society, Las Cruces, New Mexico.

[4] Brian Collier, Wilhelmus Geerts, Ahad Talukder, James Nick Talbert, Aaron Medina, Andres Oliva, Magneto-Optical Faraday Effect in NiO and NiFeO Thin Films, oral presentation TSAPS Fall-2017 meeting, Richardson (TX).

[5] Chandler Hutton, Ahad Talukder, Nick Talbert, Wilhelmus Geerts, “Electrical Characterization of Thin Films, oral presentation TSAPS Fall-2017 meeting, Richardson (TX).

TABLE OF CONTENTS

Page

LIST OF TABLES

Table **Page**

LIST OF FIGURES

Figure **Page**

ABSTRACT

The effect of oxygen flow during deposition on the crystallinity, resistivity, and magneto-optical properties was studied for reactive sputtered thin NiO and Fe-doped NiO films. A series of NiO and Fe-doped NiO samples with different oxygen concentration were made using the RF sputtering technique at room temperature on different types of substrates. In terms of deposition pressure two types of sample were made: one type was sputtered at ~1mTorr and the other at ~7-8mTorr. Film thickness and roughness were measured using the variable angle spectroscopic ellipsometry and the XRR technique. Thickness values determined with both techniques are found to be close to each other. From the XRD peak analysis of both type of samples crystal size was calculated using the Scherrer equation and the inhomogeneous micro-strain was calculated using the Stokes and Wilson approximation. A Pole Figure Analysis method which shows the dominating textures in the thin film was also done. A near surface analysis was done to get a true idea of the defects i.e. oxygen or metal vacancies in the thin films by using the Rutherford Backscattering Spectrometry (RBS). To measure the electrical properties, specifically the resistivity, the four-point probe method was used. The magneto-optical (MO) hysteresis loop were measured to determine the magnetic properties of the films. The MO Faraday data on the samples confirm preliminary results obtained by Twagirayezu using VSM [109] on these types of samples. As the magnetic signal on these samples was expected to be very small if at all present, a large effort

was spent on improving the magneto-optical measurement setup. A thorough analysis was done to better understand the Fabry-Perot interference in the Photo-elastic modulator (PEM) and the effect on the measurement method.

When using a Photo-elastic modulator (PEM) in combination with a coherent light source, in addition to the modulation of the phase, Fabry-Perot interference in the PEM's optical head induces large offsets in the 1ω and 2ω detector signals. A Jones matrix which describes both the phase and amplitude modulations simultaneously, was derived and used to find an expression for the detector signal for two different MO Kerr setups. The effect of the PEM tilt angle, polarizer angle, analyzer angle, and retardation, on the detector signal offsets show that offsets can be zeroed by adjusting PEM tilt angle, polarizer angle, and retardation. This strategy will allow one to avoid large offset drifts due to the small retardation, intensity, and beam direction fluctuations caused by lab temperature fluctuations. In addition, it will enable one to measure in the most sensitive range of the lock-in amplifiers and to adjust measurement parameters to optimize S/N ratio.

I. INTRODUCTION

1.1 Research Concentration

The requirement for larger, faster, and more energy efficient non-volatile computer memory forces researchers to find out a replacement for flash memory, which has reached its scaling limit and cannot be scaled down further without compromising data retention. For the next generation computing system, it is highly necessary to improve the performance and the power profiles of the traditional memory hierarchy. Researchers are making significant efforts for the developments of emerging memory technologies. In the memory world of the computing regime the non-volatile memory technology is drawing much more attention than others. Due to scalability issues of currently used flash technology (lowest scaling of NAND flash is $14x14nm^2$) industry is looking for a new technology that will be scalable below the 14nm technology node. RRAM (Resistive Random Access Memory) is a promising candidate. RRAM is based on a two-terminal resistive switching device made of oxide material sandwiched in between two metal electrodes. Upon setting the device, highly conducting filaments are formed between the top and bottom electrodes. Part of these highly conductive filaments can be formed and removed reversibly, providing in a non-volatile memory cell that for some materials can be rewritten over a million times. RRAM has a much smaller latency, a higher density, a lower energy consumption, and a higher re-writability than currently employed Flash memory. Because of their large ion diffusion coefficient Transition Metal Oxides (TMO) are

becoming more of an interest and have been studied more during the last years for application in RRAM devices. This thesis focuses on reactively sputtered NiO and $Ni_{(1-x)}Fe_xO$ for possible application in RRAM devices. The sputtered films are polycrystalline and have good resistive properties so might be suitable for application in RRAM.

Specifically, this thesis report on how the oxygen flow during the sputtering process influences the structure, the electrical and magneto-optical properties of reactive sputtered RF sputtered thin films. The main two parts of the thesis are: (a) characterization of the crystal structure, grain size, micro-strain, texture and morphology of reactive ion beam sputtered NiO and Fe doped Nickel-Oxide thin films; (b) an investigation of the magneto-optical properties of NiO and Fe doped NiO films.

The first task includes methods and modifications of the deposition system and process to obtain more homogeneous thin films with better defined interfaces. The method of choice in making these films is RF (Radio Frequency of 13.56 MHz) magnetron sputtering which has good compatibility to be used for metals, semiconductors and insulators and is a technique often used in industry [1]. Samples were investigated by X-ray diffraction using two different diffractometers. The crystal structure and morphology of the samples is important for the RRAM application, as filaments are expected to form at grain boundaries, and grain boundary diffusion depends on the crystal orientation. Crystal structure and morphology depend strongly on sputter parameters including substrate temperature, sputter pressure,

and oxygen flow rate [2]. The work builds on preliminary results obtained with the old departmental X-ray diffractometer. This X-ray system was replaced with a new Rigaku Smartlab X-Ray system in spring 2016. The new diffractometer has a much better signal to noise ratio and allows for wide angle scan (10^o-120^o) to be completed in 1 hour compared to 10 hour scans over a small angle range (30^o to 90^o) with the old instrument.

For the chemical analysis of the samples two different techniques were applied. X-ray Photoelectron Spectroscopy (XPS) technique was used to study the effect of substrate cleaning. From the binding energy and intensity of the XPS peaks, the elemental identity, chemical state, and quantity of a detected element can be determined. The chemical properties of the sputtered thin films, specifically the oxygen to metal atom ratio were estimated from the results of Rutherford Backscattering on two samples. This technique allows for the determination of the metal to oxygen atom ratio and thus for the determination of the metal or oxygen vacancy concentration [3][4]. These measurements were not performed at Texas State University but by a company, EAG.

The 2nd objective of this thesis is the study of the magneto-optical properties of the NiO and $Ni_{1-x}Fe_xO$ films. It was shown recently that RF sputtered NiO and Fe doped NiO films have a magnetic moment at room temperature when they are sputtered at low oxygen flow rate. To confirm these experiments that were conducted by means of a vibrating sample magnetometer, here the magnetic properties of NiO and Fe-doped NiO thin films are studied by Magneto-Optical (MO) Kerr Magnetometry [5]. It

has already been reported that nanocrystals of rock-salt NiO show ferromagnetic behavior [6] and individual lattice defects can have ferromagnetic [7]. The Room temperature magnetization of NiO result revealed a ferromagnetic-like behavior. The ferromagnetic-like properties are attributed to the lattice distortion and broken bonds in the NiO nanocrystallites [8]. The result of the refractive index difference and the retardation determined by the Optical Kerr effect convinced that nanocrystallites of NiO might be anisotropic [9]. Measurements in low fields at room temperature were done on thin films deposited on glass microscopic slides and fused silica substrate. The Verdet constant of Fe doped NiO was determined for the first time. The dependence of the magnetic properties on oxidation and iron concentration was determined.

1.2 Defects in Materials

Based on the periodic array of the crystal structure solid materials are divided into two categories: 1) Crystalline Solids and 2) Amorphous Solids.

1) A crystalline solid is a kind of solid material whose atoms are ordered in a three-dimensional periodic array. Depending on the continuity and discontinuity of the periodic arrangement there are two types of crystalline solids: a) Single Crystalline solids and b) Poly crystalline solids.

For a single crystalline solid, the crystal orientation is continuous and similar everywhere in the materials (bulk or thin films etc.). On the other hand, poly crystalline solid materials have the same crystal structure, but there are

discontinuities in the periodic arrangements. The polycrystalline materials consist of many small single crystals which are called grain and the discontinuity occur at the boundaries of the adjacent grains. The crystal structure in neighboring grains can have similar orientation. Such materials are called textures materials.

2) Amorphous solids are the examples of the total failure of the periodic atomic arrangement, the atoms are randomly oriented and do not show long range order. However, the atomic arrangement in the solid crystalline materials are not always perfect; the crystalline regularity is interrupted by the defects. A considerable number of defects and imperfections can significantly affect the materials properties, such as physical, mechanical, optical, magnetic and electronic properties of the material. Although defects change the original properties of a pure material, they can play some important roles in the materials research field. By a proper control of them, called defect engineering, one can sometimes enhance specific materials properties desired for a particular application.

<u>There are four types of defects:</u>

1) Point defects: It's a type of defects in atomic dimensions e.g. an atom is missing, replaced by impurity atom or placed in an irregular crystal lattice point. A host atom that is replaced by an impurity atom at a regular lattice site is called a substitutional impurity atom. A host atom or an impurity atom that sits at another position than a regular lattice site is referred to as an interstitial defect. Adding impurities to a perfect crystal adds point defects. These defects are called extrinsic defects. Schottky defects occur in an ionic crystal when positive and negative ions leave their

lattice sites. These defects do not affect the overall stoichiometry of the matrix since the number of positive and negative ion vacancies is the same and charge balance is maintained in the solid. For non-ionic crystals, a Schottky defect means a simple vacancy. For non-ionic materials a Schottky defect is created if an atom moves to the surface of the material [10].

Frenkel defects occurs in a solid when an atom or ion is displaced from its lattice position and is lodging at an interstitial position, causes the vacancy and the interstitial defects without changing the chemical properties [10] [11].

Antisite defects occur when different types of atoms exchange their positions in a lattice. It happens specifically in the alloy or compound materials [12].

2) Line defects: When there is a distortion centered in a row of the lattice points, then this is called the line defects or dislocation. Two types of line defects exists: edge dislocations and screw dislocations.

An edge dislocation occurs when a plane of atoms is discontinued in the crystal and the adjacent planes bend at the edge of the terminated plane to adjust the crystal structure. Materials having edge dislocations can be easily stressed because the dislocation moves parallel to the direction of the stress.

Screw dislocation occurs when a spiral path is observed along the dislocation line which is perpendicular to the direction of the applied shear stress.

3) Planer defects: This type of defects are deviations from the perfect periodic crystal that have a planar form. Examples are stacking faults and grain boundaries.

Stacking fault occurs when there is an abnormal stack of atoms in an orderly

sequence of planes. An example is the stacking faults in a face centered cubic crystal structure perpendicular to the [111] direction. In a perfect crystal the planes perpendicular to the [111] direction are closed packed with three different atom arrangements, often labeled as ABCABCABC. A stacking fault occurs when one of the layers is missing such as the structure ABCABCABABCABC.

Grain boundaries are another type of planer defect. They occur when two single crystals begin growing separately from different direction and then meet.

4) Bulk defects: A macroscopic defect in the crystal such as pores, cracks etc.

Voids are the small area in the crystal with vacancy of atoms.

Clusters of atoms (impurity etc.) can also be found in the crystal cause different phase.

It is expected that all these defects are present in RF sputtered NiO and FeNiO films and a filament are expected to form near defects, they are expected to influence switching properties. The number of bulk defects increases with sputter pressure according to Thornton's sputter model [13]. Although PyO can be grown epitaxially on MgO, the RF magnetron sputtered films in this thesis are all polycrystalline. Crystal size and texture can be modified by deposition parameters. Both NiO and FeNiO grown under low oxygen pressure have the rocksalt crystal structure which is FCC, so stacking faults perpendicular to the [111] direction can be expected. Rocksalt FeO is non-stochiometric and also numerous reports exists on NiO with metal or oxygen vacancies depending on the growth conditions.

1.3 Effects of Doping

In semiconductor science, the term doping is used to infuse some foreign atoms into the intrinsic semiconductor. The doped materials are called the extrinsic materials. Dopants are added in parts per million (ppm) range. Sometimes the term substituent is used when deliberately some host atoms are replaced by the impurity atoms [14]. Although impurities and dopants are mainly used to modify the electrical properties, they have some other effects on crystal. Interstitially dissolved foreign atoms normally affect the strain in the lattice. In ionizing states the electronutrality condition changed by their charges.

Substitutionally dissolved impurity or dopant atoms with different size and charges from the host atoms have effects on the properties of the host compound. Two different types of substitution occur in the crystal:

1) In isovalent substitution the foreign atom that is substituting the native atom has the same oxidation state or valence electrons.

2) In aliovalent substitution the foreign atom that is substituting the native atom has the difference in valence electrons. This will affect the electronutrality and the defect equilibrium condition. Since the material has to be neutral some form of charge compensation takes place, resulting in ion vacancies or change of the oxidation or reduction state of some of the metal ions [15].

1.4 NiO Thin Film

1.4.1 Formation and Structure of NiO

Pure Stoichiometric NiO is an fcc lattice adopts rocksalt crystal structure (NaCl) with

octahedral Ni^{2+} and O^{2-} sites, although a slight trigonal distortion was found at low temperature. It is antiferromagnetic with Néel temperature at ~525K [16] [17]. It has a perfectly filled Ni 3d band (8 of a possible 10 orbitals are occupied by Ni) and is strongly insulating. At 0℃ the resistivity may be ~10^{17} Ω cm [18] and at room temperature ~10^{13}Ω cm [19]. The perfect stoichiometric NiO surface is weakly reactive but if imperfect it is a perfectly useful oxidation catalyst. This inertness of the perfect surface is in accordance with the non-metallic surface of bulk NiO [20]. The band gap of NiO is ~3.6eV [18].

For the Non-Stoichiometric NiO ($Ni_{1-\delta}O$, $NiO_{1-\delta}$, $Ni_{1+\delta}O$, $NiO_{1+\delta}$) the metallic vacancies or the oxide vacancies plays very important role on electrical transportation. In $Ni_{1-\delta}O$ the dominant defects are Ni^{2+} cation vacancy cause the transformation of two adjacent Ni^{2+} ions into Ni^{3+} ions and a slight lattice distortion [21] [22]. For the excessive oxygen people also expect the cation vacancies [23] [24].

1.4.2 Literature Studies of NiO

This section contains an overview of recent publication on NiO.

Jang et al. worked on NiO thin films which were deposited by RF magnetron sputtering using a NiO target at 10mTorr and 100 degree Celsius. The Oxygen flow rate was controlled at 40 sccm. 50, 100, 200, and 300 nm thick films were deposited on the substrate. The XRD data shows that the peak corresponding to NiO decreases with the thickness decreases only the Ni peak was found for the film thinner than 100 nm. The dominant point defects were determined in sputtered NiO film by analyzing the CN change and the composition profile of the sputtered NiO films. The

result shows that the non-stoichiometry of sputtered NiO film is determined by the number of nickel atoms rather than by the number of oxygen atoms. Nickel vacancies are the dominant point defects in sputtered NiO films. The decomposition of NiO deposited at 100W and films prepared through thermal oxidation were studied. According to previous studies, the non-stoichiometry of NiO film increases with decreasing RF power. Conversely, the non-stoichiometry of a thermally oxidized NiO is very small. The value of y in $Ni_{(1-y)}O$ is about 10^{-4} for NiO equilibrium at 900 degree Celsius and O_2 at 1 atm [25].

Park et al. deposited NiO on Pt/Ti/SiO2/Si by RF sputtering using a Ni target at 300W with 5mTorr pressure. The sputter temperature varied from RT to 400 degree Celsius. Film thickness was about 1μm. The Ar/O_2 flow rate ratio was 20/4. As the growth temperature increased, NiO peaks became stronger and the XRD Bragg angles of the NiO (111) plane were shifted to that of bulk NiO in the JCPDS database. These peak shifts imply shrinkage in the lattice constant of $Ni_{(1-x)}O$ film. It is due to sufficient thermal energy for diffusion and redistribution of adatoms at substrate surface during film deposition. In the nickel oxide film grown at low temperature, the diffusion and redistribution of adatoms cannot be sufficiently achieved and many defects may be generated, while adatoms at the substrate surface can move to their stable sites and the number of defects was decreased as the substrate temperature was increased [26].

Bruckner et al. made thin films of NiO by RF magnetron sputtering using a stoichiometric NiO target at room temperature with a total constant gas flow of 10

sccm. Where the oxygen series was 0.5, 1, 1.5, 2, 4 and 6 sccm. The sputtering pressure was 555mTorr. at RF input power 700W. The film thickness was 100nm. The dominant (111) peak with weak (200) were found. Both peaks height decrease with oxygen concentration increases [27].

Guziewicz et al. NiO films were deposited by RF magnetron sputtering using NiO target at 700˚C substrate temperature while the sputtering pressure was $3.75x10^{3}$-$7.5x10^{3}$Torr. The RF source power was at 150-200W. Doping of NiO by carbon was done by co-sputtering using a Carbon target supplied by a DC source with power of 50W. The analysis of the structure of deposited NiO films reveals fcc structure of polycrystalline NiO grains with texture depending on oxygen content in plasma and on substrate temperature. XRD spectra of NiO films deposited at RT and RF power of 200W showed the (200) peak with the oxygen flow on. With the argon flow on only the (111) peak dominated with very little (200) peak observed. The lattice parameter was calculated 4.28 or 4.276A for Si or Quartz substrates [28].

Chen et al. produced NiO thin films with a thickness of 100nm were deposited at 5mTorr on glass substrates by RF magnetron sputtering of the NiO (1:1) target with oxygen ion source from an ion gun at 40sccm. The voltage of the ion source was 355V and the discharge current varies from 0.22A to 0.42A with the substrate rotation rate 10rpm. All the NiO films displays (111, 200, 220) peaks. The crystallinity of the NiO decreases (grain size) with increasing the discharge current. This result attributed to the excess of oxygen in non-stoichiometric NiO films resulting in decrease in the amount of NiO phase in the films. NiO films create vacancies to

occupy the Ni^{2+} ions, a vacancy forms at the Ni^{2+} site. The more vacancies there are in the NiO film, the lower the crystallinity of the film [29].

Yun et al. analyzed 50 nm NiO_x deposited on SiO_2 Substrate by RF sputtering using NiO target with O_2 gas flow rate at 50 sccm at 7mTorr. $NiO_{1-\delta}$ was deposited at room temperature at various sputtering powers (25, 75, 150, 225, 300W) and at 150W for various temperatures (RT, 100^{o}C, 200^{o}C). The XRD data shows the amorphous states with weak peaks assigned to (111, 220, 200) of NiO. No Ni^{3+} peak was observed and it appears that Ni^{3+} state exists as an amorphous state [30].

Karpinski et al. investigated NiO thin films which were deposited on glass substrate by DC magnetron sputtering using Ni target at the pressure 3.37-3.81mTorr with different discharge currents (110, 80, 50mA). The intensity of (111) peak decreases with increasing oxygen content from 8.2 to 9.9%. In general, the predominant peak is transferred from (111) to (200) with the oxygen concentration increasing [31].

Lu et al. deposited NiO thin films was on silicon and glass substrate by using magnetron sputtering system. The sputtering was conducted with a sintered Ni target. The applied RF power was 75-200 Watts. And the temperature varied from 100-400 degree Celsius. Only (200) peak was observed getting little bit larger with the oxygen flow rate increases [32].

Peng et al. worked on NiO thin films which were deposited by DC magnetron sputtering using Ni target on Si substrate at 500^{o}C. Sputtering was performed at a constant power of 120W for 2h. Deposition pressure was 6 mTorr. The Oxygen to argon ratio was 1:4, 1:2, 1:1. The rock salt structure of NiO and the fcc structure of Ni

are identified in sample #1 and sample#2. For sample#3, only the rock salt of NiO is identified. All the samples show the presence of diffraction peaks from the (111, 200, 220) lattice planes of the NiO lattice. The presence of peaks from the Ni (111) plane for (1:2, 1:4) indicates that there are a few metal clusters in sample#1 and sample#2. It can be concluded that no pure NiO film would be formed in the experimental conditions of sample#1 and sample#2. In the DC reactive sputtering process, the Ni clusters are difficult to be fully oxidized due to lack of oxygen with the increasing partial pressure of oxygen, the Ni metal clusters are fully oxidized to NiO. Hence, the peaks from Ni lattice planes are not found in the diffraction pattern of sample#3 [33]. Karpinski et al. deposited NiO thin film by DC magnetron sputtering on glass substrate using pure Ni target. The sputtering pressure was at 3mTorr and the discharge current was kept constant at 110mA. The nature of the deposited NiO thin films was polycrystalline with thickness varies from 50-1000nm. The XRD pattern shows two diffraction peaks (111, 200). With increasing oxygen content the (200) peak intensity increases. At 23.5% oxygen the (200) peak started getting smaller than previous. A Ni(111) metal peak was also found but after 9.9% oxygen concentration the phase seems changes to polycrystalline. After 23.5% oxygen content the peaks are getting smaller, probably due to a partial amorphous [34].

Fasaki et al. prepared NiO thin film by reactive pulsed laser deposition(RPLD) process using Ni target on Si substrates. Pulses from a KrF excimer laser (wavelength- 248 nm, 10ns pulse duration) source at 10 Hz repetition rate were focused on the surface of Ni targets. To deposit each film 60000 subsequent laser pulses were applied in

75mTorr oxygen ambient atmosphere. The deposition was performed at RT, 100^{o}C, 200^{o}C, 300^{o}C, 400^{o}C. The (111) peak started dominating after 200^{o}C deposition temperature. A Ni (002) peak was found shows the metallic Ni existence. Higher temperature atoms get more kinetic energy to reach in the equilibrium state. Therefore, there is more probability to form a more perfect crystalline structure. The grain size of NiO increases with the substrate temperature [35].

Saadati et al. produced NiO films of different thicknesses by Electron beam evaporation technique at room temperature with different thickness 285, 515, 595, 645nm. The substrate temperature was varied from 575-775K. The deposition rate was 2.5nm/s. NiO (111, 200, 220, 311) peaks observed. With the increasing thickness the (111) peak intensity decreases and (220, 311) peak disappears and (200) peak only dominates which means the single crystal NiO [36].

Ashok et al. made NiO thin film by DC magnetron sputtering using a Ni target at the substrate temperature 200 degree Celsius while the pressure was at 1.5-15mTorr in an Ar/O2(60/30sccm). The samples were deposited for 10, 20, 60 minutes. XRD data shows the polycrystalline NiO with (111, 200, 220) peaks. The lattice constants calculated for different thickness was 4.216, 4.193, 4.191A. They also calculated the microstrain and dislocation density by XRD [37].

Venter et. al. deposited NiO using Ni shot which was resistively heated in a Al_2O_3 coated tungsten basket. The Ni layer was subsequently annealed in oxygen for a period of 1-2.5h. in the temperature range from RT-600 degree Celsius. The oxygen flow rate was 200 cm^3/min. The deposition rate was 2.0-3.0 A/s. The thickness was

1000A. The XRD data shows the (111, 200) polycrystalline NiO peaks. With the temperature increasing the metallic Ni peak (111) intensity decreases and after 400^{o}C it vanishes. But with increasing temperature the NiO (111) peak is getting prominent as well as (200) peak. For layers oxidized at 400˚ and 550˚ the lattice parameter was calculated 4.5nm and 8.5nm respectively [38].

Yang et. al. NiO and K_2CO_3 powder were mixed together and pressed. The $Ni_{1-x}K_xO$ thin films were made by PPD (Pulsed Plasma Deposition). XRD Patterns of $Ni_{0.75}K_{0.25}O$ thin films. At room temperature the structure is amorphous but starting from 100 degree Celsius the structure shows the polycrystalline phase. Increasing the temperature makes the peaks (111 & 200) more sharp and larger in between of these two 200 peak was prominent. In other words, it shows the better crystallinity. The theory behind is that the ablated atoms obtained more kinetic energy when they arrived at the substrate surface because of the extra thermal energy provided by the heated substrate. Hence, they have higher probability to reach the equilibrium positions and this leads to form a more perfect crystalline structure [39].

Chen et. al. NiO-Cu Composite target was used to RF sputter Cu-doped NiO on glass substrate at the deposition power 80W while. The deposition rate was 0.055 nm/s without Cu but it started increasing to 0.057, 0.062, 0.063, 0.064, 0.068, 0.077 and 0.078nm/s with the increasing number of Cu chips 2, 4, 8, 12, 16, 20, 24 respectively. The composition ratio of Ni to O in a NiO target was 1:1. The deposition pressure was 5mTorr. Un-doped NiO showed (111,200, 220) sharp peaks which is decreasing with gradually increasing the Cu content specially after 6.97 at%. This is due to the

substitution of Cu (0.96 A) for Ni^{2+} (0.78A) ions in the NiO lattice, resulting in the reduction of the NiO amount in NiO-Cu composite films and the degradation in the crystallinity of the NiO films. No Cu peak found [40].

Reddy et. al. synthesized NiO-Cu Composite target was used for DC reactive magnetron sputtering and Cu-doped NiO was sputtered at 0.2 pascal on glass substrate while the power was 90W. By increasing the temperature the predominant (220) peak is decreasing and the (111) peak is dominating. No Cu peak found. When increasing the substrate temperature, absorbed atoms gain extra thermal energy and tend to move to another preferred site. High substrate temperature can offer more kinetic energy for mobility of particle on surface to achieve better crystalline growth. The crystallite size increases from 7.06 to 8.27 nm with (220) preferred orientation and 9.84 to 10.86 nm with (111) preferred orientation by increasing the growth temperature [41].

1.5 Fe-Doped NiO Thin Film

1.5.1 Structure and Formation of Fe-Doped NiO

When Fe is added or substitutionally doped in NiO the Fe^{2+} ions either replace the Ni^{2+} ions or fill in the Ni^{2+} vacancy. The radius of Ni^{2+} ion is 0.69A whereas the Fe^{2+} is 0.74A. Since the radius of these two ions are very close so the shift of the lattice constant is very unlikely. Due to the ionization energy of the Fe^{3+} (~33eV or 2957 kJ/mol) [42] is less than the ionization energy of Ni^{3+}(~35eV or 3395kJ/mol) [43] it is also expected that if there are more Fe ions than the Ni ions close to the Ni^{2+} vacancy two Fe^{3+} ions are created to compensate that vacancy. John et al. showed that an

oxygen vacancy most likely to sit next to an Fe-atom than the Ni atom.

1.5.2 Literature Studies of Fe-doped NiO

Ati et. al. synthesized Ferrites nanomaterials with composition $Ni_{1-x}Co_xFe_2O_4$ (x= 0.0, 0.2, 1.0) by chemical co-precipitation method. The X-Ray diffraction pattern of the different chemical compositions $Ni_{1-x}Co_xFe_2O_4$ (x= 0.0, 0.2, 1.0) product at 600 degree Celsius for 8h show a pure-phase with a cubic spinel structure $NiFe_2O_4$ and Co doped nickel ferrite. All the samples exhibit a poly-oriented structure with several peaks with several peaks characteristic of other crystallite planes (220, 311, 222, 400, 422, 511, 440), which explain the single phase cubic spinel structure of $Ni_{1-x}Co_xFe_2O_4$. The most intense peak (311) are used to estimate the sizes of the $Ni_{1-x}Co_xFe_2O_4$ nanocrystallites and are found the range of 16,19, 17nm for (x= 0.0, 0.2, 1.0) respectively. The lattice constants are 8.330, 8.335, 8.361A. The lattice parameters are found to increase almost linear by increase of Co content. The show linear increase in lattice constant can be explained by the basic of the ionic radii. The ionic radius of Ni^{2+} (0.69A) is replaced by the slight larger Co^{2+} (0.74A) in the system of $Ni_{1-x}Co_xFe_2O_4$ [44].

Chang et. al. deposited a series of single-crystalline Fe-Ni oxide alloy thin films, $Fe_{1-x}Ni_xO_y$ (x=0.15, 0.3, 0.35, 0.5, 0.56, 0.65, 0.71), are grown by an MBE system. Notice that if the structure is spinel then the notation should be $Fe_{3-x}Ni_xO_4$ ($0<x<3$) but if the structure is rocksalt then $Fe_{1-x}Ni_xO_y$ ($0<x<1$) is more appropriate [45].

Landon et. al. synthesized mixed $Ni_{1-x}Fe_xO$ (x= 0.05, 0.1, 0.2, 0.25, 0.5) powders produced by EISA (Evaporation-Induced Self Assembly) method. As the Fe content is

increased up to 10 mol% the peak positions from the NiO lattice remain constant. The lattice constants from each of these XRD patterns, excluding pure iron oxide, yielded a value of 4.18A. This suggests Fe was not substitutionally incorporated into the NiO lattice as the lattice constant would have changed with Fe composition. As the concentration of the Fe increased a peak at 35^{o} started growing. This peak is due to the formation of the NFe_2O_4 spinel phase. The peak intensity for the spinel phase increases with increasing Fe content up to 25 mol% Fe. At higher Fe compositions, peaks associated with Fe_2O_3 begin to be observed, which continue to grow with increasing Fe composition [46].

Anup et. al. synthesized metastable polycrystalline permalloy monoxide films PyO with NiO-type rocksalt crystalline have been fabricated by reactive dual ion beam sputtering(RDIBS). The PyO thin films were deposited on top of the Si/SiO_2 substrate followed by the Py metal film. The films were fabricated at substrate temperature 350K (for the Py film), and 473K or 673K (for the PyO layer) and also rotated for heating and deposition uniformity. Ion beam sputtering of the $Ni_{81}Fe_{19}$ (Py) metallic target was done with a focused dual grid source operating at 800eV (~18mA beam current) producing a mono-energetic Ar^+ or Kr^+ beam impinging at ~45degree with respect to the target normal direction. All PyO samples exhibit diffraction peaks comparable to rocksalt-type NiO (111, 200) diffraction peaks. However, they found that the RDIBS NiFeO samples can be fabricated with greater crystalline texture than those previously fabricated by magnetron sputtering [47].

Liu et. al. deposited pure NiO and Fe-doped NiO nanofibers with different doping concentration were synthesized by electrospinning. The XRD patterns of $Ni_{1-x}Fe_xO$ (x= 0, 0.01, 0.02, 0.05) shows five diffraction pattern at the angles of 37.2, 43.4, 62.9, 75.2, 79.4 degrees correspond to (111), (200), (220), (311), (222) characteristic peaks of cubic crystalline NiO. The lattice constant of the Fe-doped NiO nanofibers hardly shifted with the increase of Fe content since the ionic radii of Ni^{2+}(0.69A), Fe^{2+}(0.74A), and Fe^{3+}(0.64A) are quite close [48].

Dixit et. al. investigated nanopowder of $NiFe_2O_4$ synthesized by using the nitrates of nickel and iron along with citric acid as the host. The powder was then pressed in the pellet which was sintered at 1200^oC for 3h. A lambda physic KrF excimer laser of wavelength 248nm was used for deposition. Pulse energy was 220 mJ, pulse duration 20 ns, and repetition rate was kept 10Hz. The substrate temperature was 600^oC. In order to maintain the stoichiometry oxygen gas was flowed during deposition under a pressure of 100mTorr. Four samples were deposited for 16, 20, 30, 40 min to get different thicknesses. The XRD pattern confirms that the target has pure spinel phase of nickel ferrite. The films also show the spinel phase of nickel ferrite but there are some extra peaks appear at ~39 and ~48 degree in 16 and 30 minutes samples. These peaks are alpha-Fe_2O_3. The peak appearing at ~29 degree in 16, 30, 40 minutes films are attributed to (220) peak of nickel ferrite phase indicating a shifting of towards the lower angle. All films are polycrystalline [49].

Luders et. al. analyzed $NiFe_2O_4$ films grown by off-axis target-facing-target RF sputtering. (001)-oriented STO single crystals were used as substrates and heated to

800˚Celsius before film growth. For the lattice mismatch there is a compressive strain induced on the film. The films were grown at temperatures from 450-550^{o}C in a pure Ar atmosphere at a pressure of 0.01mbar and with an RF power of 50W. Two peaks were found at 43.6 and 95.6 degrees with the planes (004) and (008) respectively. The absence of the other reflections confirms that the films grow textured along the (001) direction [50].

Rios et. al. used a modified dual ion beam sputtering system for sample fabrication. Atomically smooth Si (001) substrates capped with a thermally oxidized SiO2 layer(190nm) were used for the polycrystalline PyO layer growths. Epitaxial NiFeO (100) films were obtained using epi-ready MgO (100) substrates. For all of exchange bias bilayer structures, the PyO was fabricated on top of the thermox layer, followed by the Py metal film. They discovered that the optimized Radical assist-ion beam sputtering (RA-IBS) approach can produce textured polycrystalline films with either enhanced (111) or (100) fiber-texture compared to traditional reactive ion beam sputtering [51].

Perera et. al. deposited permalloy oxide thin films on Si/SiO_2 substrates by DC magnetron sputtering using Py targets. The typical film deposition rate was 0.1-0.2nm/s at 7mTorr sputtering pressure. Where $Ar:O_2$= 6sccm : 1sccm. The XRD data shows the predominant randomly oriented single phase NiO. The Debye-Scherrer formula suggests an average PyO grain size of ~12nm [52].

Seifikar et. al. employed Chemical solution deposition to grow biaxially textured $NiFe_2O_4$ thin films on (001) sapphire substrates. To grow the NFO films, a 0.5M NFO

solution is spun onto a pre-cleaned substrate. The films are pyrolyzed at 400^{o}C for one minute and crystallized at 750 degree Celsius for 10min in air, resulting in 60nm thick film. A randomly grown NFO film is grown on a Si/SiO_2 substrate using similar processing conditions for comparison. XRD pattern of NFO films on the sapphire indication the presence of an inverse spinel cubic structure without any detectable interfacial or secondary phase. While the Si/SiO_2/NFO film shows random crystallographic orientation, the Al_2O_3/NFO film reveals a high degree of out-of-plane preferential growth in the <111> direction with Lotgoring orientation factor of ~93% [53].

II. SAMPLE PREPERATION

2.1 Introduction

In this chapter substrate choice, the substrate cleaning process, and the deposition process and parameters are discussed. Bare microscopic slides, fused Quartz, and Si/SiO_2 wafers, and NaCl crystals were used as substrate. Spectroscopic Ellipsometry and XPS was used to determine quantitative cleanliness of the sample surfaces after each type of solvent and plasma cleaning. RF magnetron sputtering was used to deposit the thin films.

2.2 Substrate Choice

Several types of substrates were chosen as template for the thin film samples. Silicon is very flat and provides a conducting path to the substrate making it an ideal

substrate choice for SEM, C-AFM, or perpendicular electrical characterization studies. Films on silicon are also ideal for ellipsometry studies. The large difference between the optical constants of Si and the TMO allows for a more accurate determination of the film thickness and optical properties. Microscope slides and fused quartz are good substrate choices for linear 4-point-probe studies. Although microscope slides are cheaper, fused quartz substrates are also allowing for transmission studies up and beyond 5 eV. Also for the first time NiO and PyO were deposited on thin NaCl substrates. These substrates allow us to create a thin film membrane and measure properties of just the thin film material.

1) Si/SiO_2 (2.21nm)
2) Si/SiO_2 (~500nm)
3) Microscopic Glass
4) Fused Quartz Substrate
5) NaCl

2.3 Substrate Cleaning

Since human beings and air contain various kinds of atoms and among them some are very reactive in contact with other materials when they are exposed in air, therefore, material contamination is the main obstacle to the way of processing devices fabrication. In order to obtain high performance and high reliability semiconductor devices, and to prevent contamination of process, clean environment is the prerequisite for reproducible device manufacturing. The next step is to use a clean substrate on which the device will be made otherwise the contaminants will

mess up the whole device by keeping away from getting desired optical and electrical properties. For example, when a silicon substrate is exposed in air a thin layer of SiO_2 is created on the surface, when a quartz substrate is exposed to air containing contaminants devitrification can take place which makes a crystalline thin film surface, etc. There are several cleaning processes: (1) Solvent Cleaning (AMI cleaning, RCA cleaning, Piranha Cleaning etc.) (2) Plasma Ion cleaning (RF biased plasma cleaning, Copra cleaning, etc.) etc. to clean the substrate.

2.3.1 Solvent Cleaning

AMI Cleaning: First clean the substrate with deionized water. Then dip the substrate in the Acetone, Methanol and IPO consecutively. (Sonicator is used to stir up the liquid with sound wave. Spin Coater is also used to spread the liquid with the centrifugal force using rpm.).

RCA Cleaning: The RCA cleaning procedure has three major steps used sequentially:

1. Removal of insoluble organic contaminants with a mixture of H_2O:H_2O_2:NH_4OH (5:1:1) solution (SC_1).

2. Removal of a thin silicon dioxide layer where metallic contaminants may accumulated as a result of (1), using a diluted H_2O:HF (50:1) solution.

3. Removal of ionic and heavy metal atomic contaminants using a solution of H_2O:H_2O_2: HCl(6:1:1) (SC_2).

Piranha Cleaning: The Piranha clean is a mixture of H_2SO_4:H_2O_2 (3:1), is highly oxidative and removes metals and organic contamination.

[This clean is suitable for putting samples in a furnace without contamination; however, a few guidelines need to be followed. If a sample has a large amount of organic impurities (i.e. photoresist) the piranhas etch will form an insoluble organic layer that can't be removed. It is recommended to follow photoresist cleaning procedure first if photoresist was used on the sample. Another important factor is that the RCA1 step removes most particles strongly attached to silicon wafers by etching underlying Si/SiO_2. Thus, the RCA clean is preferred for MOS fabrication. However, the piranha clean can be applied to a large number of materials. Due to the self-decomposition of hydrogen peroxide, piranha solution should be used freshly-prepared. Piranha solution should not be stored. Immersing a substrate (such as a wafer) into the solution should be done slowly to prevent thermal shock that may crack the substrate material. Piranha solution can be explosive near or in contact with Acetone, Propanol, or any organic solvents. Mixing the solution is exothermic. The resultant heat can bring solution temperatures up to 120°C. One must allow the solution to cool reasonably before applying any heat. The sudden increase in temperature can also lead to violent boiling, or even splashing of the extremely acidic solution. Also, explosions may occur if the peroxide solution concentration is more than 50%.]

Plasma Cleaning: Plasma surface cleaning has been widely used to achieve clean surfaces in fusion energy research, in high-energy accelerators, and in materials processing. This cleaning method utilizes radical species generated in reactive gas

discharges to remove surface contaminants. The energetic radical species in these discharges consist of photons, electrons, ions, and reactive neutral species. Physically, these energetic particles impinge on surfaces to cause sputtering, thermal evaporation, or photodecomposition. Chemically, the surface heating caused by these energetic particles greatly enhances chemical reactions. These impinging particles are generally very hot; for example, 1 eV of energy is equivalent to a temperature of the order of 11,600 K. Thus, the energetic plasma particles have higher rates of chemical reactions with surface contaminants than those of thermal reactive gas particles. It is well known that reactive oxygen plasmas are very effective for removing organic contaminants from surfaces. The dominant reactive species in oxygen plasmas-hot electrons, energetic ions, atomic radicals, ozone, and ultraviolet (UV) photons-actively clean organic contaminants by physical sputtering, thermal evaporation, chemical reaction, or photodecomposition. By controlling gas pressure, applied power, and other discharge parameters, we may use such reactive plasma particles with suitable energy and flux to perform gentle, damage-free cleaning on contaminated surfaces. Several types of plasma were used to clean the substrates.

A) Experimental Arrangements

1. Quartz substrates were cleaned with the Acetone, Methanol and IPA respectively. Pyrex beakers were used as receptacles and the substrate was kept for 5 minutes in the sonicator for every cleaning step.

2. Buffered Oxide Etchant (BOE) with water to HF ratio 10:1 was used to clean the

quartz substrate. Teflon Beakers were used as receptacles and the substrate was kept into the solution for 30 seconds (etching rate = 2 A/sec).

3. Oxide plasma was used to clean quartz substrate for five minutes at the power of 100w using the plasma cleaner in the cleanroom.

4. Copra (Argon plasma) was used to clean the quartz substrate for five minutes at the power of 250w keeping the gas pressure at 2.6 sccm while the reflected power was tuned to zero value and the current flow of the DELTA ES power supply was kept at 1.9 amperes which gives the voltage value ~3V. The chamber pressure during the Copra cleaning process was below 1 mTorr.

5. Substrate Bias (Argon plasma) cleaning was also used to clean the quartz substrate for five minutes at the power of 40w keeping the argon gas flow at 100 sccm while the reflected power was minimized to (~1-3W).

X-ray Photoelectron Spectroscopy was also used to quantify the cleaning process by measuring the bonding energy of the surface electrons come from different atomic bonds. Kapton tape was used to mount the sample to the sample holder. Since XPS was installed in the ultrahigh vacuum(UHV) system each sample had to be baked at 150 degrees Celsius for more than one hour to remove the contaminants absorbed to the surface of the sample. A magnesium anode was used to generate the X-ray beam.

The XPS data are:

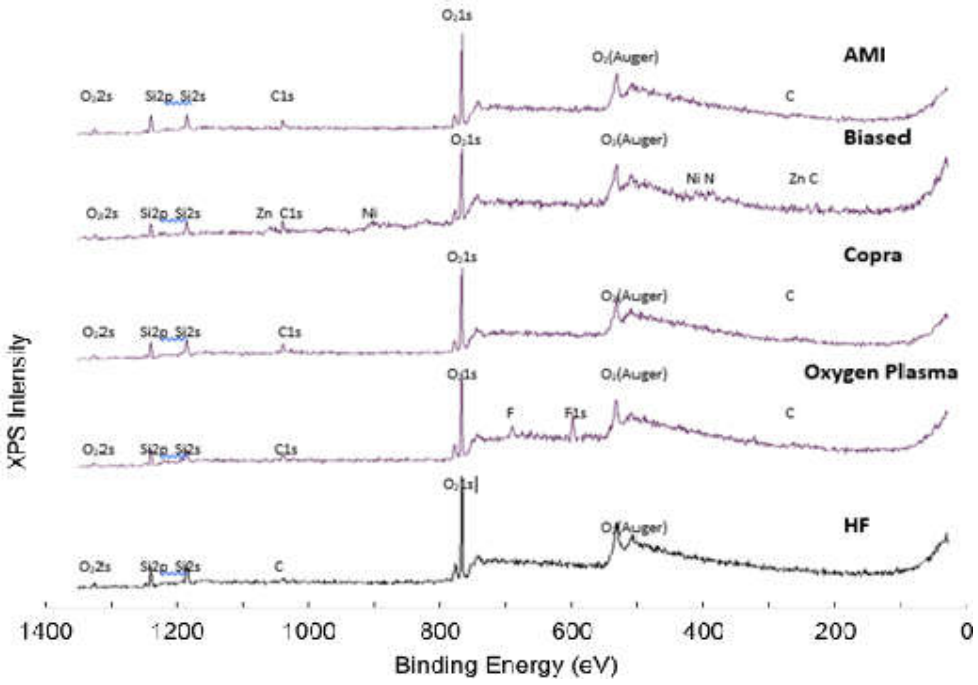

Fig. 2.1: Intensity vs Energy graph of the cleaned substrate.

Since our samples are semiconductors and poor conductors when X-Rays incident on the sample surface remove an electron from an atom it causes charging effects (short period of time) on the sample surface. These charging effects result in shifted peaks. XPS graph analysis showed that all of the samples exposed in the air after cleaning have a common contaminant Carbon(C) on it. We also found Florine(F) on the sample which was cleaned by the Oxide plasma. The substrate cleaned by substrate bias had Ni and Zn contaminants on it. It is believed that those atoms are sputtered from the sample-holder on the sample. The power is too high and will sputter the substrate holder. Part of those sputtered atoms redeposit on the substrate. The small mean free path at 13 mTorr will allow part of the sputtered atoms to be redeposited on the substrate. The HF cleaned sample showed a smaller carbon peak than the samples cleaned with the other techniques: HF cleaning is

done by an etchant so we should check the roughness of the surface before and after etching. Also we should keep in mind that we baked the substrate at around 150 degrees Celsius which vaporized some other contaminants which can deteriorate the properties of the devices if we manufacture them without heating the substrate.

2.4 Thin Film

2.4.1 Sputter Deposition Process

Sputtering, first discovered in 1852 [54] and developed by Langmuir for thin film deposition [55] in 1920, is a physical vapor deposition process. It uses the kinetic energy of the particles (generally ions, while hitting the target) to kick out the atoms or ions from the surface of a target. In the sputtering chamber, the energized particles are produced as a glow diffused plasma in between an anode and a cathode. The cathode, the electron emitter, is the target material and the anode, the electron receiver, is the chamber and the substrate. There are several types of sputtering [56]:

- DC Diode Sputtering
- Magnetron Sputtering
- Unbalanced Magnetron
- Balanced Magnetron
- RF Sputtering
- Reactive Gas Sputtering
- Ion Beam Sputtering
- Pulse DC/AC Sputtering etc.

Direct Current diode sputtering technique is the simplest technique for the sputtering process. The sputtering target works as cathode and the substrate and the chamber both act as anode, which is always kept at ground potential [58]. The applied potential appears across a region near the cathode. The plasma is generated near the cathode surface [59]. In DC sputtering the cathode must be an electrical conductor [57] otherwise for insulating material surface charging causes issues. Charging of the target by sputter ions creates an electric field that prevents or slows down further ion bombardment of the target surface. The advantage of the DC discharge is that the plasma can be established uniformly over a large area [60].
In dc sputtering the electrons that are ejected from the cathode or created in the plasma are not efficiently used for sustaining the discharge and are accelerated away from the cathode. To remove this problem, a magnetic field is added to the dc sputtering system that deflects the electrons and keeps them longer near the target surface [60]. The Magnetron Sputtering uses magnets around the cathode (the target materials) to trap the secondary electrons close to the surface of the target by the magnetic field and increase the ionization probability. A magnet is positioned at the center of the target and surrounded by a circular pattern of magnets around the periphery of the target. The pole facing the target of the center and periphery magnets is opposite creating a magnetic field parallel to the target surface in the direction of the r circular unit vector. This field will constrain the secondary electron motion close to the target. This way of trapping the electrons around the target substantially increases the probability of an ionizing electron-atom collision

occurring. These high current electrons produce a high-density plasma i.e. a plasma with a high secondary ion density. This, in turn, leads to increased ion bombardment of the target, resulting in higher deposition rates at the substrate. Furthermore, the more secondary ions achieved in the magnetron mode allows the glow discharge to be maintained at lower operating pressures and lower operating voltages than is possible in the basic sputtering mode [61][62].

RF sputtering is used when one wants to deposit insulating material. When an RF potential with a large peak-to-peak voltage is capacitive coupled to an electrode, an alternating positive-negative potential appears on the surface. During part of each half-cycle, the potential is such that ions are accelerated to the surface with enough energy to cause sputtering, while in alternate half-cycles, electrons reach the surface prevent any significant charge buildup. RF sputtering can be used to sputter insulating material [59], although the sputtering rate is low. A major disadvantage of RF sputtering of dielectric targets is that most insulating materials have poor thermal conductivity and high coefficients of thermal expansion, and are usually brittle materials. Since most of the bombarding energy produces heat, this means that large thermal gradients can be generated that can result in fracturing the target if high power levels are used or if the gun's power level is suddenly changed [59].

Reactive gas sputtering involves the addition of a reactive gas, especially O_2 or N_2, in the sputtering process to make a new product produced by the reaction of the gas and the sputtered target material. This reaction is controlled by the desired amount of gas flow allowed into the chamber. Reactive sputtering has some disadvantages

like low film growth rate and possible arcing. Special power supplies have been developed which include the arc suppression unit. Arcs often occur during the reactive sputter deposition of, for example, non-conductive oxides from a metal target in pure O_2 or mixed Ar/O_2 discharges, due to buildup of oxides on the edges of erosion groove where the sputter rate is low [62]. Low growth rates result from the decreased sputter yield of the compounds (for example oxides or nitrides) due to the higher binding energy in those compounds [63].

2.4.2 Process Window Study

An on axis reactive magnetron sputtering system from AJA Sputtering was used for the thin film deposition on various substrates including Si, Si/SiO_2, Quartz, and Glass Slides. The cylindrical shaped main chamber contains five deposition guns i.e. 3 DC guns and 2 RF guns. The main chamber interconnected with the load lock system through which a substrate holder with substrates can be transferred with a sliding stick. The background vacuum level of the main chamber is typically at ~10^{-8} Torr while in the load lock system it often stands at ~10^{-7} Torr. It is allowed to open the valve in between the deposition chamber and the load lock system to transfer the sample when the ratio of the pressures in both chambers is less than a factor 100 apart. A clasp at the end of a z-stage holds the substrate holder. The substrate holder can be rotated (highest at 60rpm) while executing the deposition process.

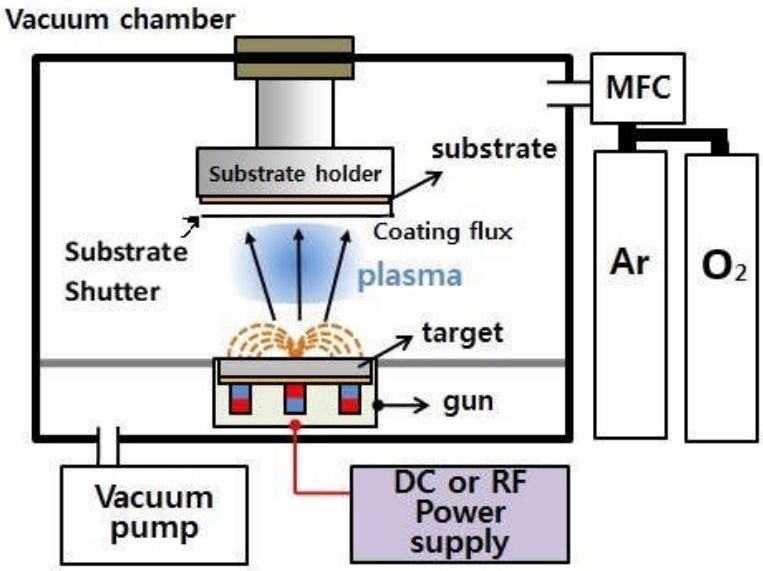

Fig. 2.2: Main chamber view of DC/RF reactive magnetron sputtering.

Inside the main chamber (see Fig. 2.2) the sputter guns are situated at the bottom while the substrate holder is hanging from the top of the cylindrical chamber. The substrate holder has a heating capacity of ~700˚C. The substrate holder and main chamber are grounded. To keep the targets cool while depositing, cold water is supplied by the chiller around the targets. Each deposition gun has its own shutter which can be opened or closed by the computer. The oxygen gas is let into the chamber at the substrate holder while the argon sputter gas is let into the chamber via the sputter guns. As a large change in deposition parameters, i.e. voltage, was observed by Cui when opening the gun-shutters, the system was modified, and an additional substrate shutter was installed. The substrate shutter is placed in between the substrate holder and the sputter guns. The substrates shutter blocks the deposition beam of any of the sputter guns. So, it is now possible to open the gun shutter and have the sputter power supplies stabilize before removing the substrate

shutter and exposing the substrate to the sputter beam. It is believed that the installation of the substrate shutter will result in samples that are more homogeneously through the film thickness. A quartz crystal monitor (QCM) is attached at the bottom of the substrate shutter which provides an estimation of the deposition rate. The crystal's resonance frequency is a measure for its mass; the change of its resonance frequency is thus a measure for the deposition rate. An impedance matching network is used to match the load impedance of the AC generator with the plasma's impedance. This is done to reduce the power reflected back into the power supply, keeping the plasma alive as well as protecting the RF generator. The impedance of the plasma is not constant but varies with the deposition parameters including pressure and power. The equivalent circuit of a plasma consists of the parallel circuit of a diode, a resistor and a capacitor whose parameters vary over time. To ensure that optimum power coupling is established, the impedance matching network is automatic.

2.4.2.1 Influence of the gas flow on different deposition parameters

A set of experiments was done with introducing the oxygen gas into the deposition chamber, to check the influence of the addition of oxygen on the plasma; specifically, the influence on the deposition rate was studied. Introducing oxygen gas into the main chamber while sputtering causes a great change in the dynamics of the plasma. Increasing the oxygen gas flow i.e. the number of oxygen molecules per unit volume, increases the probability of collisions of oxygen atoms with the target, the substrate

and with other gas atoms in the system. These collisions can result in a large number of chemical reactions.

Increasing one of the gas flow while keeping the other constant increases the chamber pressure almost linearly (see Fig. 2.3 and 2.4 below) in either case of Ar or O_2. The relation is less linear for oxygen which could be due to the deposition of oxygen in the thin film. Gettering of oxygen in the thin film depends on deposition rate and total pressure. The former depends on the thickness of the oxide layer which is different for the ascending and the descending curves in Fig. 2.3.

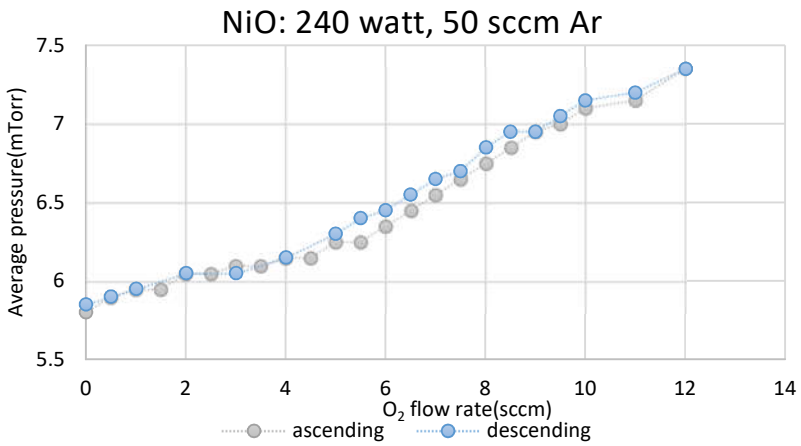

Fig. 2.3: Change of deposition pressure with the Oxygen flow. Argon flow was kept constant at 50 sccm.

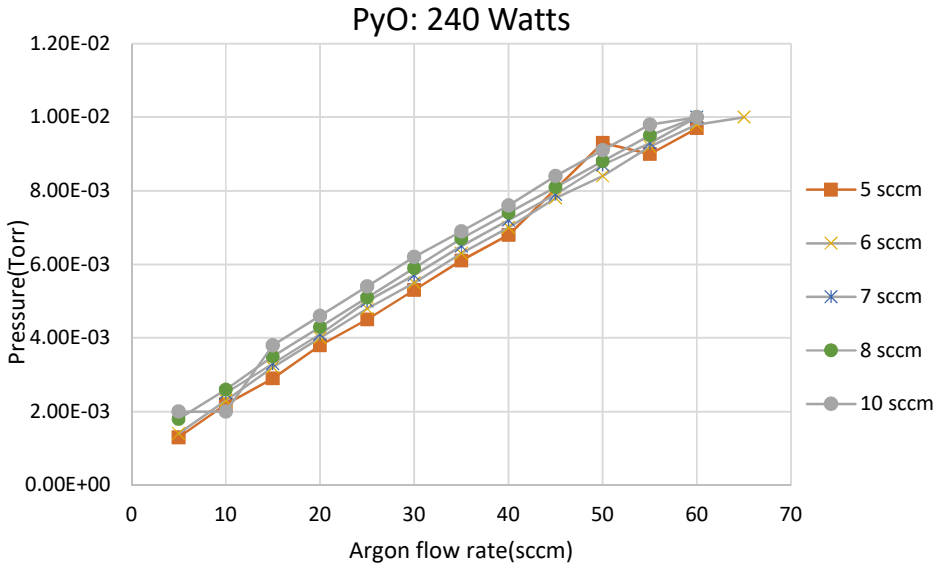

Fig. 2.4: Change of pressure with the Ar flow in different Oxygen flow.

Figure 2.5 shows the DC voltage versus the oxygen flow rate for the nickel target at 240 Watts and 50 sccm argon flow. There is initially a linear increase of the voltage with the oxygen flow until 5.5 sccm after which the DC voltage starts to decrease. For higher oxygen flow rates, the DCV curve shows hysteresis. It is believed that this hysteresis is caused by oxidation of the target. Note that at large oxygen-flow the deposition is almost impossible because of the low deposition rate. Fig. 2.6 shows the DCV as a function of the argon flow rate for different oxygen flow rates for the permalloy target. With the increase of the Ar gas flow the DC voltage decreases exponentially. This decrease is caused by the decrease of the plasma's density.

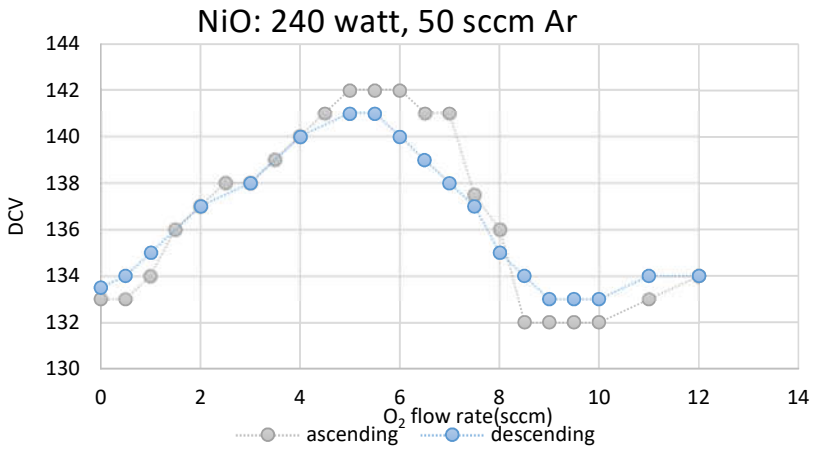

Fig. 2.5: Change of DC voltage with the Oxygen flow. Argon flow was kept constant at 50 sccm.

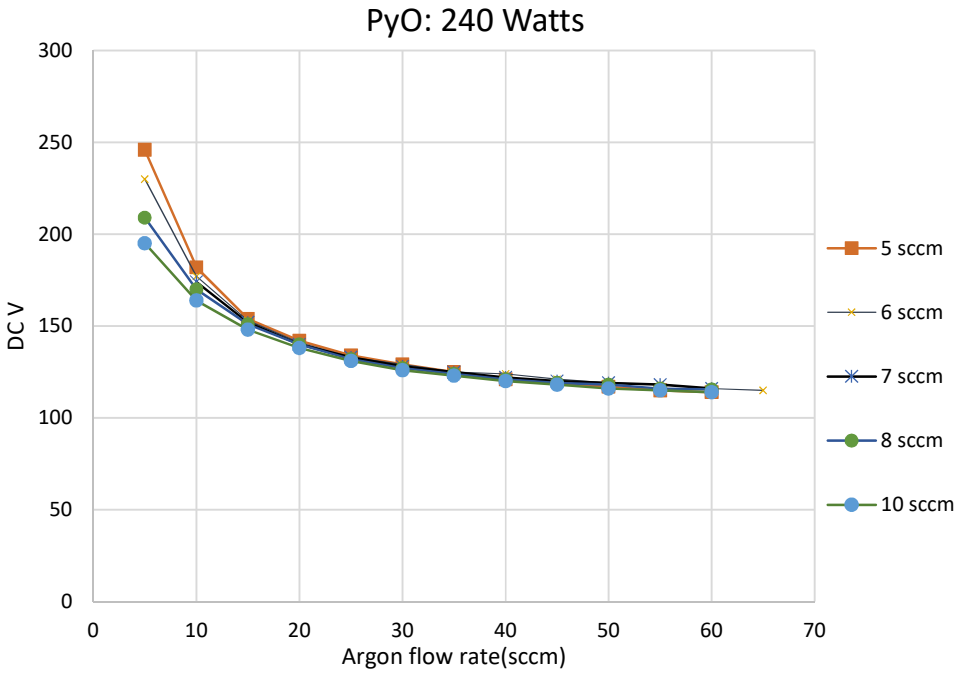

Fig. 2.6: Change of DC voltage with the Ar flow in different Oxygen flow.

There is a tremendous effect on the deposition rate while increasing/decreasing the Ar/O_2 gas flow ratio. The figure below (see Fig. 2.7) shows that the deposition rate increases while increasing the Ar flow while keeping the O_2 flow constant. This implies that increasing the Ar gas flow reduces the mean free path of the

electrons/ions i.e. increases the collision rate. Furthermore, this increases the sputtering rate of the target materials.

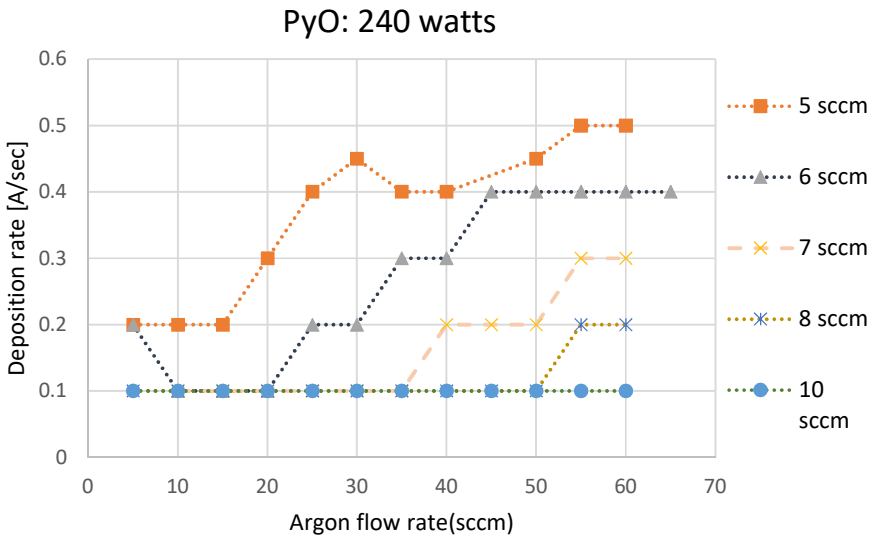

Fig. 2.7: Change of deposition rate with the Ar flow in different Oxygen flow.

On the other hand, introducing oxygen into the deposition chamber also increases the collision rate but oxygen is much more reactive than Ar. At a small level of the oxygen flow the deposition rate increases rapidly and then starts to drop with the oxygen flow. In this case, more oxygen creates a negative effect on the deposition rate. As the oxygen flow increases and reaches towards the target it starts reacting with the target materials. Whatever the target material is if the surface is not oxidized yet it starts to oxidize the surface and makes the sputtering more difficult since the binding energy of the oxide materials are larger than the binding energy of the metal. The hysteresis in the data shown in Fig. 2.8 is also an indicator for the oxidation of the target and suggest that charging effects might also slightly influence the deposition rate.

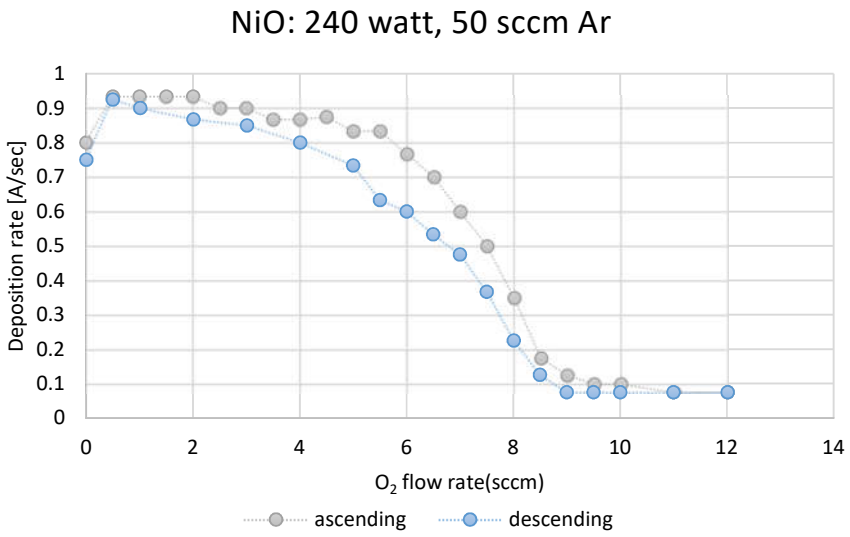

Fig. 2.8: Change of deposition rate with the Oxygen flow.

2.4.2.2 Importance of the physical models in sputtering

The mobility, in other words the energy, of the ad-atoms determines the microstructure of the thin films. The energy supply to the atoms is provided by the following mechanism: 1. thermal effect, 2. ionic bombarding and 3. chemical reactions at the substrate. So, ultimately, the morphology of the deposited films depends on the sputtering parameters such as deposition pressure, temperature, power, DC voltage, distance between the substrate holder and the targets, shape of the chamber etc. The influence of these parameters on the morphology and microstructure of the thin film growth can be explained by the structural zone model (SZM). There are several physical models that can explain these effects are following: The first model on the sputtered metallic thin films was proposed by Movchan and Demchishin in 1969 who showed that the microstructure of the thin films of Ti, Ni, ZrO_2 & Al_2O_3 is related to the normalized deposition temperature, i. e. T/T_m. T is the

temperature of the substrate and Tm is the melting temperature of the deposited thin film. They made a three-zone model for metallic thin films (see Fig. 2.9). The first zone is T/T_m <0.3. This zone is formed by small and elongated grains that form a columnar structure with porous morphology and weakly binding grains. This columnar structure is produced by a low diffusion, a low mobility of the atoms adsorbed by the substrate surface, and the atomic shadow effects; probably have low residual stress in the crystal lattice. Shadow effects are produced by the varying growth rate of the columns and the various incidence angles at which the atoms arrive at the surface of the substrate. In the second zone, $0.3 \leqslant T/T_m \leqslant 0.45$, the substrate temperature increases homogeneous which leads to a higher diffusion of the ad-atoms, which produce a denser structure with a higher degree of binding among the columns. In this zone, the size of the grain increases with substrate temperature. The broadening of the grains is equiaxial, from the interface of the substrate with the film to the film's surface. In the third zone, T/T_m>0.45, the volumetric diffusion size has a great influence on the morphology of the film, due to the increase in the diffusion into the grains, which produces growth of the grains, formation of the equiaxed grain and re-crystallization. These effects produce a greater crystalline structure.

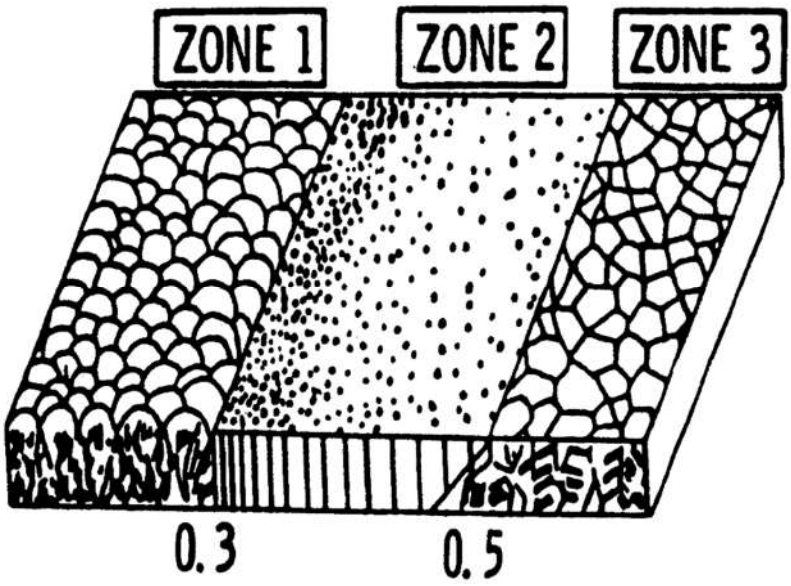

Fig. 2.9: Movchan and Demchishin (1969) three zone model.

In 1974 Thornton introduced a two-dimensional model considering the temperature and the deposition pressure. From his knowledge, pressure inside the deposition chamber influences the kinetic energy of the ion bombardment, mean free path of the ions/particles which results in increasing/decreasing of the particles deposition rate on the substrate. In the Thornton model, the T zone as a transitional zone between first and second zone discussed above was added. The T zone is formed by grains defined by the limits of the low porosity and good crystallinity. The surfaces of the T zone are denser and less rough since the grain size in this zone are smaller than the two surfaces around them [63] (see Fig 2.10).

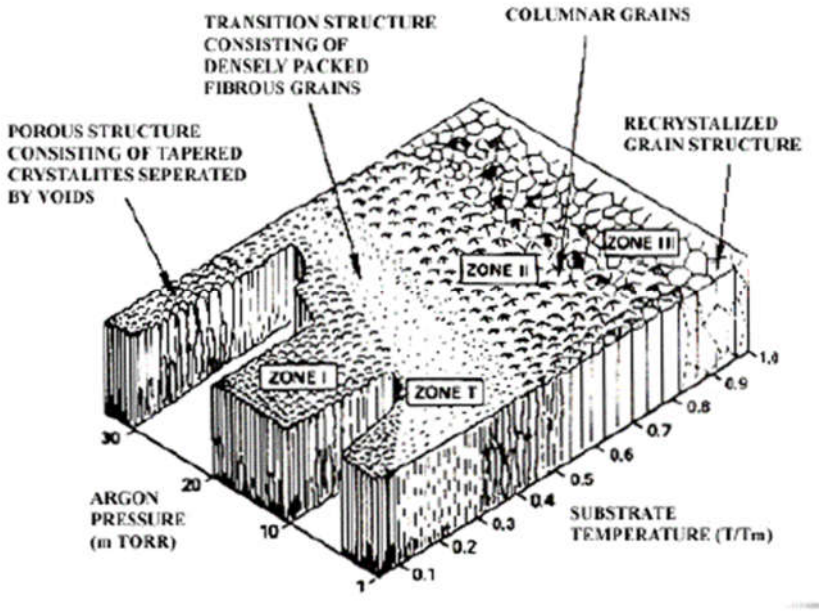

Fig. 2.10: Thornton Zone Model (Thornton 1974).

In 1984 Messier & Giri found that in thin films of TiB_2, BN and SiC there is a non-linear limit between the first zone and T zone, which is a function of the bias voltage applied to the substrate. The bias voltage of the substrate has the same effect on the mobility and adsorption of the atoms as an increase in the temperature, so when it is increased, the T zone increases and the first zone decreases, resulting in denser thin films and with a high degree of crystallinity [63].

In 1998 Kelly et. al. added another variable in the SZM model in order to explain the thin film microstructure. In their model, they showed that the relation between ion density current (J_i) and density deposited atoms (J_a) has a simultaneous influence on the deposition process and thin film crystallinity with the normalized temperature and the bias voltage. In Fig. 2.11, it can be observed that it is possible to obtain the third zone with high density using a combination of high density ionic current,

intermediate values of normalized temperature, and low bias voltage [59][60].

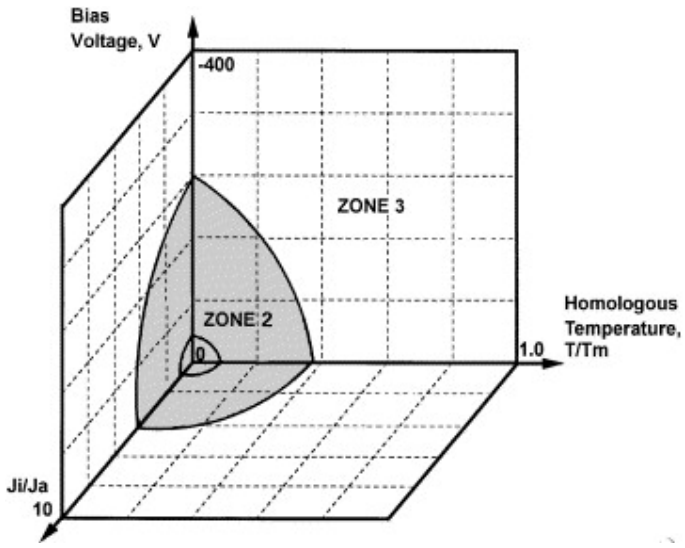

Fig. 2.11: 3D SZM of Kelly and Arnell (2000).

The films investigated in this thesis were sputtered at two different pressures. The high-pressure samples were sputtered at a pressure of approximately 8 mTorr. The other samples were sputtered at a pressure below 1 mTorr. According to the zone classification of the previous models it can be concluded that the thin film morphology of the high-pressure samples matches with the first zone i.e. there is columnar adsorption of the particles on the substrate surface with very low atomic diffusion Additionally, lots of porosity occupy the thin film. It can also be said that the chemical reaction of the metals with the oxygen may reduce this porosity. The morphology of the low-pressure samples is expected to be T-zone type. Note that both types of samples were sputtered at room temperature so T/T_m=0.13.

2.4.2.3 Optimum parameterization

To ignite the plasma and start the sputtering process several conditions must be met.

The main chamber, in other words, the deposition chamber, has to be evacuated and its base pressure should be in the 10^{-7} Torr to 10^{-8} Torr range to minimize contaminants in the thin film. The effect of small concentrations of contaminants can have a significant effect on the electrical properties of the films. To avoid contaminants, a low base pressure is important. After obtaining the desired vacuum level, the working gas (inert gas), in this case Argon, is released through an MKS mass flow controller. Simultaneously oxygen is let into the chamber via another mass flow controller. For the high-pressure samples the total gas flow rate was kept at 50 sccm resulting in a sputter pressure of around 7-8mTorr. The gas flow used for the high-pressure samples is provided in the table below.

Table 2.1: Estimated Argon/Oxygen flow rate.

Percentage of oxygen level	Ar flow +/- 1 sccm (>2 sccm)	Oxygen flow +/- 0.2 sccm (>0.4 sccm)
39%	30.5 sccm	19.5 sccm
28%	36 sccm	14 sccm
20%	40 sccm	10 sccm
14%	43 sccm	7 sccm
10%	45 sccm	5 sccm
7%	46.5 sccm	3.5 sccm
5%	47.5 sccm	2.5 sccm
3.6%	48.2 sccm	1.8 sccm
2.5%	48.8 sccm	1.25 sccm

2.4.2.4 Electron-atom/electron-molecule interaction

The interaction of energetic electrons with Ar atoms can be either elastic or inelastic. For elastic collision kinetic energy and momentum are conserved. For inelastic collisions, where kinetic energy is not conserved, the interaction is not well explained

classically. In inelastic collision, the atom gains the same amount of internal energy that is equal to the loss of electron kinetic energy. This internal energy excites an electron to a higher energy level, thereby creating an excited atom. This transferred energy must be in discrete amounts since the energy levels of the atoms are quantized. Excited states are limited in their lifetime and will decay by emitting a photon as the electron falls back to its ground state level. Excited states called metastable, however, can last for very long times and can be significant in low-pressure discharges. If there is enough energy transferred from a high kinetic energy electron, electron can be liberated from the atom producing an ion [64]. For large impacting electron energies, the process could leave the ion in an excited state, the secondary (ejected) electron could have excess kinetic energy, or the impacting electron could retain a large amount of energy.

$$e^- + Ar = Ar^+ + e\ (1^{st}) + e\ (2^{nd})$$

The interaction of energetic electrons with molecules differs from interactions with atoms because there are lots of degrees of freedom, to absorb electron energy. Low-energy electrons can attach to electronegative molecules to form negative ions [65] and since there is an abundance of low-energy electrons in plasmas, negative ions are common in plasmas when the ambient contains electronegative gases such as, oxygen [66]. A two-body reaction produces an O^- ions and a three-body reaction produces an O_2^- ion. For oxygen, the reactions leading to ion formation are [67]:

$$e^- + O_2 = O^- + O$$

$$e^- + O_2 = O^- + O^+ + e$$

$$e^- + O_2 + O_2 = O_2^- + O_2$$

Among all the dominant attachment processes is the two-body dissociative attachment process [68].

2.4.2.5 Estimation of the dependable parameters

A cylindrical shape main chamber was used for the deposition. The oxygen gas flow is provided through the opening of a circular pipeline attached around the substrate holder from the top of the chamber. At 300K with the pressure at 7-8mTorr the number of atoms/molecules present in 1 cm^3 is calculated by using the ideal gas law:

$$\boldsymbol{PV = NK_BT}$$

$$\boldsymbol{7\times10^{-3}Torr \times 1cm^3 = N \times 1.38\times10^{-23}\,{}^{J}/_{K} \times 300K}$$

$$\boldsymbol{7\times10^{-3}\times133.322\,{}^{N}/_{m^2} \times 1cm^3 = N\times1.38\times10^{-23}\,{}^{J}/_{K} \times 300K}$$

$$\boldsymbol{So, N \approx 2.25\times10^{14}\ per\ cm^3}$$

The Mean free path of the sputtered atoms can now be estimated form the collision cross section of the argon atoms and ions $\boldsymbol{\sigma}$ and the concentration of the argon atoms and ions N. Assuming that the collision cross section of Ar^+ ions is approximately $30*10^{-16}$ - $60*10^{-16}$ cm^2 it is found that the mean free path is:

$$\boldsymbol{\lambda = \frac{1}{N\sigma} = \frac{1}{2.25\times10^{14}cm^{-3}\times45\times10^{-16}cm^2} \approx 1.0125\ cm}$$

Note that this is a sputtered metal atom might collide with several argon ions before it collides with an oxygen molecule as the partial pressure of oxygen for our process is in between 1-20% of the total sputter pressure. So, for the high-pressure sputter process the total path length the sputtered atoms travel between colliding with oxygen molecules is 100 cm (1% oxygen) – 5cm (20% oxygen). The total path length

would be even larger for the low-pressure process (1 mTorr), i.e. 700 cm (1% oxygen) to 35 cm (20% oxygen). (The aforementioned estimations shows that for the low pressure process and for the high-pressure process at low oxygen flow rates the probability of the sputtered atom colliding with an oxygen molecule in the plasma is very low. So for those processes the reaction with oxygen takes place on the substrate or on the target. Only for the high-presssure high oxygen flow process the collision probability of the sputtered metal atoms with the oxygen molecules is significant. We currently do not have the experimental capability to determine the whether or not the oxidation takes place in the plasma. To confirm that we need a special spectroscopy technique which is not available in our system.

The impingement rate of oxygen atoms on the substrate surface per unit time is [69],

$$\boldsymbol{\varphi = 3.5\times10^{22}\times\frac{P*\%O2}{\sqrt{mT}}}$$

Where, P is the pressure in Torr and m is the mass of the molecule in a.m.u. At 300K the number of oxygen molecules striking a unit surface per unit time is therefore

$$\boldsymbol{\varphi_{o2} = 3.5\times10^{22}\times\frac{7\times10^{-3}*\%O2}{\sqrt{32\times300}} \approx 2.5\times10^{18}\ \%O2\#/\text{cm}^2\text{-sec}}$$

For the experiments described in this thesis this varies between $1.84*10^{16}$ and $1.84*10^{17}$ molecules/sec.

The arrival of Ni and Fe atoms at the surface can be estimated from the deposition rate, i.e. 1 A/sec. Since the lattice constant of the NiO unit cell is 4.2A, if we assume (100) texture, a 1A/sec deposition rate will result in a rate of approximately 0.5 a mono layer of NiO per second. If we assume that each metal atom sticks and that the material is stochiometric, the arrival rate of metal atoms at the substrate is

approximately $1.1*10^{15}$ atoms per $cm^{-2}sec^{-1}$. Assuming that the ad-atom mobility is negligible, the arrival rate of oxygen atoms at a substrate lattice site is a factor 20 to 200 times larger than the arrival rate of metal atoms. If it is assumed that an oxygen atom will stick when it hits a metal atom, the probability for an oxygen vacancy is rather low.

The distance between the target and the substrate was approximately 22cm. The substrate was rotated at 60rpm during deposition to get a more uniform thickness across the sample. The deposition power was kept at 240W while the voltage depended on the gas flow rate. A metallic Ni or $Ni_{81}Fe_{19}$ target was used. Note that prior to deposition the targets were pre-sputtered for 1 minute with open gun-shutters to remove contaminations and to stabilize the sputter parameters. After this minute, the substrate shutter was opened.

The standard operating procedure of the sputtering and plasma cleaning processes are provided in Appendix A.

2.5 Summary of Deposition Data of The Realized Samples

In terms of pressure, two types of polycrystalline thin films were deposited on different types of substrates. A series of samples sputtered at 1 mTorr (low pressure series) and a series of samples sputtered at 8 mTorr (high pressure series). According to the Thornton 2D sputtering model the low pressure (~1mTorr) series is expected of have a transition zone morphology whereas the high pressure (~7-8mTorr) series is expected to have a morphology similar to Zone 1. In addition, we conclude from this model, that the low pressure thin films are expected to have less porosity

compared to the high pressure thin films. In addition to that the high pressure thin films might have some fiber structure and have lots of defects.

III. THICKNESS MEASUREMENT

3.1 Introduction

This chapter reports on the thickness measurements performed on the sputtered thin films. Two different methods were used: (1) ellipsometry; (2) XRR. Both techniques are explained in the chapter and the measurement results for the NiO oxygen series samples are summarized. A comparison is made between results obtained for both techniques in the final section.

3.2 Ellipsometry

The peculiar properties of light attracted the curious minds from the early stage of the development of science. Researchers in the early 17th century like Grimaldi (1665) first described some of them and then Newton. After them Dr. Thomas Young and M. Fresnel put a significant contribution in optics. Since then, researchers observed different colors resulting from the interference effect comes from the thin film layers. In the early 18th century scientists measured the intensity of the light to measure the physical properties of the transparent materials. At the same time, the polarization of the light was developed. Drude, in the late 1800, used the phase shift between the two mutually perpendicular components of the polarized light to measure the thickness of the thin films down to the tenths of angstrom. When the

two mutually perpendicular components of the polarized light are out of phase the light becomes elliptically polarized, and hence the technique developed following Drude's early measurement came to be called 'ellipsometry'.

3.2.1 Theory of Ellipsometry

Ellipsometry is a specular optical measurement technique that characterizes the reflected (or transmitted) light from thin films [70]-[72]. The Key features of the ellipsometry is that it measures the change in polarization in between the incident and reflected (or transmitted) light upon reflection on a sample (or transmission through a sample). Since the polarized light often becomes 'elliptical' upon reflection, it is named as 'Ellipsometry'. Polarized light can be described by the superposition of two linearly polarized light waves: s-polarized light and p-polarized light. S-polarized light is polarized perpendicular to the plane of incidence; the 's' stands for the German word 'senkrecht' meaning perpendicular. The p-polarized light is polarized parallel to the plane of incidence.

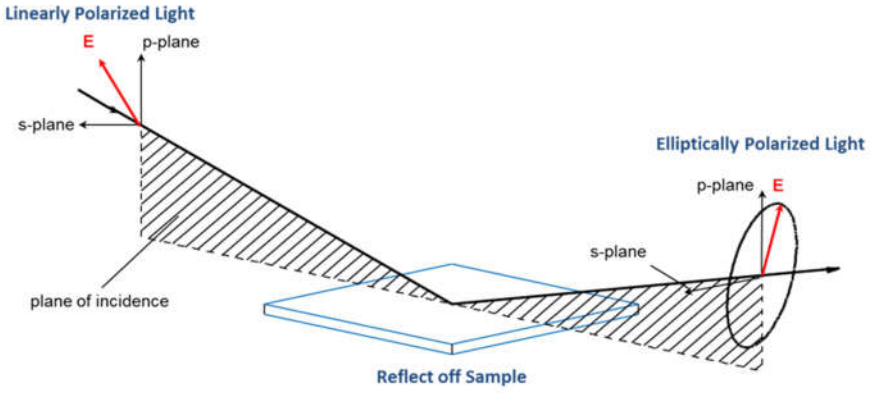

Fig. 3.1: Linearly polarized light becomes elliptically polarized light upon reflection.

Ellipsometry measures two quantities for each wavelength: Δ and ψ where Δ stands for the phase difference between 'p' and 's'-components of the beam and ψ is

related to the absolute value of the amplitude ratio between the p-polarized and the s-polarized light. Note that, at perpendicular incidence the $\Delta = 0$ and $\tan\Psi = 1$ since there is no difference between 'p' and 's' polarized light. These two values are combinedly related to the Fresnel's reflection coefficient $\tilde{R}p$ and $\tilde{R}s$ of 'p' and 's' polarized light, respectively

$$\rho = \frac{R_p}{R_s} = \tan(\psi)\, e^{i\Delta} \qquad [3.1]$$

Where, the complex ratio 'ρ' is often presented within the so-called pseudo dielectric function.

Since ellipsometry measures the ratio of two reflection coefficient it is less sensitive to scattered light than traditional reflection and transmission measurements where intensity are measured. Furthermore, it also measures the phase information which makes it extremely sensitive to the thickness of the layers. Ellipsometry can be used to detect film thickness variation on the order of an angstrom. In spectroscopic ellipsometry (SE), (Δ,ψ) spectra are measured for different wavelength of light[73]. The spectroscopic ellipsometry (SE) employs broad band light sources, which cover a certain spectral range in the infrared, visible or ultraviolet spectral region. From that the complex refractive index or the dielectric function tensor in the corresponding spectral region can be obtained, which gives access to a large number of fundamental physical properties. The refractive index can be obtained with an absolute accuracy of the order of 10^{-3} and a relative accuracy $\leqslant 10^{-4}$ (J. A. Woolam Co.). Ellipsometry is an indirect method; It's a model based technique in which the variables it directly measures are not much informative; a suitable model fit with the

experimental data though can give some very valuable information about the sample properties [74].

With ellipsometry it is possible to measure the optical properties (n,k), the film thickness and the roughness of the surface. There are two general restrictions on the ellipsometry measurement: 1) Surface roughness has to be rather small and 2) the measurement (for reflection mode) must be performed at oblique incidence (in our case it is 55˚, 65˚and 75˚). Ellipsometry determines the polarization state from its light intensity. If the surface roughness is too large (i.e. larger than 30% of the wavelength) it becomes challenging to measure the polarization state because the roughness increases the scattering of the light beam resulting in significant depolarization and a reduction of the intensity of the specular reflected beam [73]. When the roughness increases, the measurement errors increase (depending on the instruments) so that the data achieved from the fitting becomes unreal.

3.2.2 Experimental Setup

A Woollam M-2000® rotating compensator Spectroscopic Ellipsometer was used to measure the thickness of the thin films (oxygen series) studied in this thesis. The M-2000 is available in a variety of spectral ranges with options from the UV to the NIR. The widest spectral range is 193nm to 1690nm with simultaneous data collection at more than 690 wavelengths. It can measure Ψ from 0°-90° and Δ from (0°-360°). A light beam with a diameter of 2mm-5mm is emitted from a Quartz Tungsten Halogen (QTH)/Deuterium(D_2) light source and linearly polarized by a fixed calcite Glan-Taylor

polarizer. The beam deviation of the polarizer is <1arcmin and the extinction ratio is $1x10^{-6}$. This linearly polarized light passes through a continuously rotating compensator (retarder, quarter wave plate). The rotating compensator has a rotational velocity of ~20Hz and causes a beam deviation that is <1arcmin. The beam is reflected of the sample which is placed on the sample stage. A vacuum pump helps to push the sample flat to the sample stage and to tightly hold the sample on the stage. An electro-optic alignment detector, which is divided into four quadrants, assists with the alignment process. The user adjusts the sample tilt so the intensity measured by each quadrant is equal, using the Cross-hair displayed on the computer console. The alignment resolution is better than 0.001˚. After the tilt is optimized by the user, the computer automatically measures the intensity as a function of the sample height and determines the maximum of that function. Two rotating knobs with the sample stage helps to adjust the samples vertically and horizontally. After reflection, the radiation passes a fixed second polarizer, which is called analyzer and is also made of calcite. Then the beam falls into the detector and is converted into an electric signal.

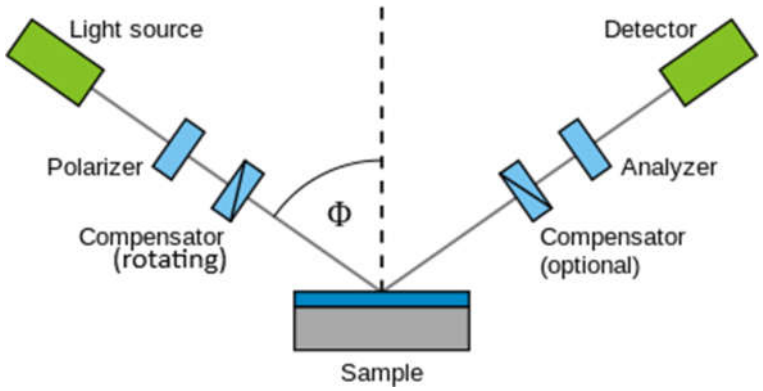

Fig. 3.2: Schematic diagram of the Ellipsometry set-up.

3.2.3 Experimental Results

Traditionally, “Wavelength-by-wavelength fits” (also referred to as “point-by-point fits”) are performed where the dielectric function values of interest are extracted from the experimental data for each wavelength, and independent of all other spectra data points. For this procedure, thickness of the particular layer as well as dielectric functions and thickness of all other sample constituents have to be known. The dielectric function obtained from the point-by-point fit needs then further comparison with model assumptions in order to obtain values of physically relevant parameters such as phonon mode frequencies and broadening parameters [75].
The wavelength by wavelength fit doesn’t use the neighboring wavelengths to help determine the optical constants. So, a small amount of noise can be seen in the optical constants, due to the observed noise in any data point in any specific wavelength. It is possible to improve a wavelength by wavelength fit by a second B-Spline fit; using the optical properties from the wavelength by wavelength fit as an initial guess for the B-Spline fit [76]. In this thesis this approach was followed. From table 3.1 below we see that the fit with wavelength by wavelength and the fit with B-Spline are close enough. Although a roughness fitting was also done but it seems that somewhere the roughness are unreal. To verify the accepted value of the ellipsometry data we further performed the XRR measurement on the same thin films samples (see 3.2.2).
Summary and comparison of Ellipsometry fitting with wavelength by wavelength and B-spline model:

Table 3.1: Comparison of the Ellipsometry data with WvlbyWvl and B-Spline fit.

		Bspline		Bspline			Wvlgth by Wvlgth		
Sample Properties		No Roughness		With roughness					
Oxygen flow	Ar flow	Thickness [nm]	MSE	Thickness	Roughness	MSE	Thickness	Roughness	MSE
10	40	15.33	1.312	9.83	8.32	1.242	12.68	6.65	1.301
10	40	11.24	1.342	7.35	6.84	1.292			
7	43	26.92	0.693	18.78	8.79	0.625	27.18	0	0.619
7	43	27.21	0.656	20	8.01	0.59			
5	45	64.39	0.814	64.87	1.33	0.683	65.39	0	0.629
5	45	63.79	0.771	64.18	1.24	0.653			
3.5	46.5	72.09	1.893	74.62	3.52	0.657	75.81	2	0.764
3.5	46.5	71.49	1.926	74.72	3.7	0.65			
2.5	47.5	62.42	1.449	64.89	4.33	0.795	64.89	4.33	0.71
2.5	47.5	62.42	1.485	64.74	4.2	0.835			
1.8	48.2	50.53	1.046	50.67	2.41	0.891	50.92	2.29	0.793
1.8	48.2	50.25	1.037	50.67	2.41	0.891			
1.25	48.75	52.35	1.695	58.67	4.49	0.618	58.36	4.49	0.453
1.25	48.75	52.31	1.617	58.71	4.38	0.582			
0.4	49.6	56.32	0.597	56.46	1.12	0.55	57.19	0.7	0.429
0.4	49.6	56.16	0.586	56.3	1.08	0.544			

Details on the measured data and fits are shown in Appendix B.

3.3 X-Ray Reflectometry

3.3.1 Basics of XRR

Beside ellipsometry another surface sensitive nondestructive technique widely used nowadays in materials science to quantitatively characterize the thin films is X-Ray Reflectivity. It is a powerful method to measure the thickness, roughness and the refractive index (density) of the thin films surfaces and multilayers [77]. The measured reflectivity curves can be analyzed by using the Fresnel formulas of reflection and transmission [78]. XRR can be used to analyze single crystalline, polycrystalline or amorphous thin films and multilayers. Although it is difficult to determine the thickness of metals with ellipsometry because of the high absorption, XRR can be used to measure the thickness of metallic thin films: XRR doesn't depend on the transparency of the thin films in the visible part of the spectrum as the absorption of EM-wave in the X-ray part of the spectrum are typically much lower; so opaque films under visible light can often be studied successfully by X-rays. The range

of the film thicknesses that can be measured by XRR is from several nanometers to ~500nm although some people mentioned ~1000 nm [79]. Thicker films require a more monochromatic more parallel incident beam.

When $n_1 > n_2$ total reflection can only occur when an x-ray beam impinges on a sample surface at a small glancing angle. Since this kind of reflection takes place outside of the materials it is called the total external reflection. Near the grazing incidence the reflected intensity becomes much more sensitive and is significantly influenced by a little change in refractive index. Due to this sensitivity and due to the comparatively strong variation of the optical constants δ and β at strong resonances it can become necessary to include dispersion and absorption corrections into the data analysis. In the range of X-Ray scattering, the refractive index is always less than one and is defined as:

$$n = 1 - \delta - i\beta \qquad [3.2]$$

Where,

$\delta = \frac{\rho_e r_e \lambda^2}{2\pi} \approx 10^{-6}$, wavelength dependent dispersion coefficient and,

$\beta = \frac{\mu\lambda}{4\pi} \approx 10^{-8}$ wavelength dependent absorption coefficient.

Here,

ρ_e = electron density (Z electrons/ atom)

λ = wavelength of X-ray

μ =linear absorption coefficient for energies far from X-ray threshold

r_e = classical electron radius $= e^2/mc^2$

For most materials, the real part of index of refraction of materials in the x-ray part of the spectrum is less than unity. So, most materials have a lower refraction index than vacuum for X-rays. According to Snell's law'

$$\frac{\cos\alpha_i}{\cos\alpha_t} = \frac{n}{n_0} \qquad [n_0=1 \text{ for air}] \qquad [3.3]$$

Where α_ι and α_τ are the complementary angles of the optical angle of incidence and angle of refraction normally referred to as the glancing angle of incidence and reflection. At the critical angle of incidence $\alpha_i = \alpha_c$ for which $\alpha_t = 0$ and x-rays are totally reflected from the interface. In this case we can neglect the absorption coefficient, β, hence we get from equation 3.2 and 3.3,

$$n \cong 1 - \delta = \cos \alpha_c \qquad [3.4]$$

Using the small angle approximation, we get,

$$\alpha_c \approx \sqrt{2\delta} \approx 1^\circ \qquad [3.5]$$

Beyond the critical angle the X-ray will penetrate into the thin film and thin film interference takes place. The reflectivity of a single layer deposited on a semi-infinite substrate can be expressed as,

$$R = \left| \frac{r_1 + r_2 e^{-2ik_{0z}t}}{1 + r_1 r_2 e^{-2ik_{0z}t}} \right|^2 \qquad [3.6]$$

Where, $r_{1,2}$ are the Fresnel reflectivity coefficients of the thin film surface and the substrate interface respectively, k_{0z}, is the component of the wave vector of the beam in the z-direction transmitted through the layer and t is the film thickness.

Intensity maxima can occur in two ways,

1) If $\exp(-2ik_{0z}t) = 1$ [3.7]
2) the path difference between the reflected waves should be an integral multiple of the incident wavelength for constructive interference i.e.

$$2t\sqrt{\sin^2\alpha_{im} - \sin^2\alpha_c} = m\lambda \qquad [3.8]$$

Here, 'm' is the Kiessig fringe order. The glancing angle of incidence is small in most

cases; hence we get from equation (3.8),

$$\alpha_{im}^2 - \alpha_c^2 = m^2 \left(\frac{\lambda}{2t}\right)^2 \qquad [3.9]$$

The basic idea behind this technique is to reflect a beam of x-rays from a flat surface and then measure the intensity of x-rays reflected in the specular direction (reflected angle equal to incident angle). If the incident light impinges on the sample beyond the critical angle for total external reflection, then the reflected light reflected from different layers interferes constructively or destructively resulting in Kiessig fringes in the reflectivity spectrum [80] (see Fig. 3.2). If the interface is not perfectly sharp and smooth then the reflected intensity will deviate from that predicted by the law of Fresnel's reflectivity. The deviations can then be analyzed to obtain the density profile of the interface normal to the surface [81]. The critical angle below which no interference fringes are observed provides information about the refractive index of the thin film, the width of the oscillation fringes gives information about the film thickness and the slope of the oscillation provides the information on the roughness of the film. Note that the amplitude of the thickness fringes increases with density contrast between film and substrate. Also, the higher the electron density the more intensity is scattered at higher angles.

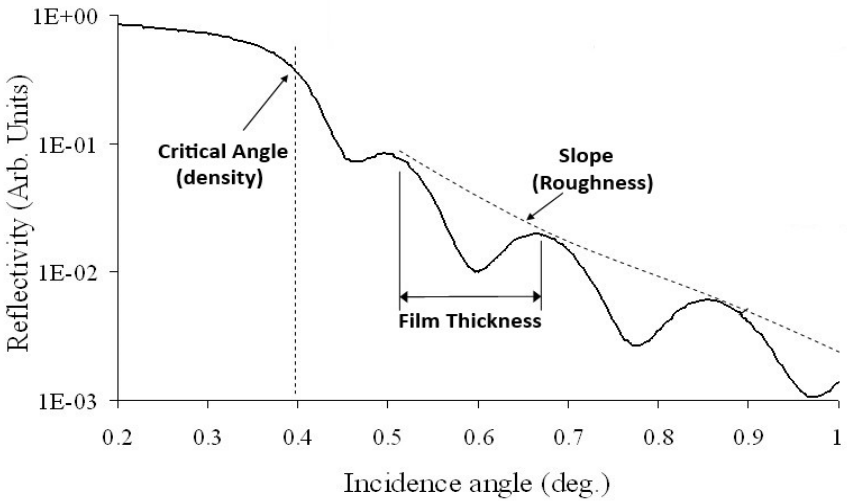

Fig. 3.3: Interpretation of the XRR data.

3.3.2 Experimental Setup

A Rigaku Smartlab high-resolution X-ray diffractometer was used to perform the X-ray Reflectivity measurement. A standard anode Cu Kα source (1.76kW) was used to generate the X-ray beam. The incident and reflected beams were collimated with a soller slit consisting of many parallel metal sheets of and a length limiting slit 5mm in height and the reflection intensity was measured by a scintillation counter. The specular reflectivity curves were recorded with a θ-2θ measurement geometry but the typical angles for an XRR measurement are much smaller than for a θ-2θ scan. To get highly accurate data to determine thickness and roughness, it is necessary to precisely align the sample with respect to the incident X-ray beam. The sample on the quartz substrate with thickness ~1mm and on Si/SiO_2 substrate with thickness ~0.5mm are mounted on a vertical flat sample stage, which is installed on a higher resolution goniometer. The 2θ angular resolution of the instrument is 0.0001°. The optical alignment process is carried out automatically by a software setup controlled

by the X-ray computer. After the setup is aligned the system continues by aligning the sample. By repeatedly adjusting the zero of the z and θ axis, an optimum position is obtained in which the sample is located at the center of the X-ray beam and only half of the intensity of the incident X-ray beam is detected by the detector. Then, by setting the detector (2θ) at an appropriate critical angle position, the total external reflection adjustment starts. By further optimizing the z, ω and χ positions, maximum reflection intensity which equals the intensity of the incident beam is achieved. The θ-2θ scan was done from 0˚- 8˚ with the incident beam at a grazing incidence.

3.3.3 Experimental Results

XRR was used to measure the thickness of the NiO samples made on the quartz substrate. The reflectivity fit shows the thickness, density and roughness of each layer. Quantitative experimental measurement data with fits are following:

Table 3.2: Thickness analysis of the thin NiO films through XRR.

Ar:O_2(in sccm**)**	Roughness(nm)	Density(g/cm^3)	Thickness(nm)
49.6:0.4	1.817	5.4761	57.487
48.75:1.25	2.628	6.946	50.10
48.2:1.8	2.9813	6.75767	52.3026
47.5:2.5	3.3363	6.41204	61.971
46.5:3.5	2.59	5.68	69.3881
45:5	2.62	5.47	61.5
43:7	1.5	4.6	22.7
40:10	2.1	6.9921	6.9921

More details on the measured data and the fits are presented in the Appendix C.

3.4 Summary of Thickness and Roughness Data

The thickness that was measured through the fitting of the experimental data with the models using ellipsometry correlates with the XRR fits. Although the roughness

of these two fittings are off from each other, the roughness estimated from XRR are most trustworthy since the models are used for the ellipsometry are nonphysical.

IV. MICROSTRUCTURE

4.1 Introduction

The crystallinity including crystal structure, crystal size, and texture, was studied by X-ray diffractometry. Two different diffractometers were used to study (1) the high pressure thick film oxygen series (NiO and $Fe_{0.2}Ni_{0.8}O_{(1-\delta)}$); (2) the high pressure thin film oxygen series (NiO only); the low pressure thin film oxygen series ($Fe_{0.1}Ni_{0.9}O_{(1-\delta)}$) and $Fe_{0.2}Ni_{0.8}O_{(1-\delta)}$).

4.2 Theory of XRD

In 1895, while Wilhelm Röntgen was investigating different types of cathode rays coming from different vacuum tubes, he noticed that the fluorescent barium platinocyanide screen was glowing when the rays fall on it. To his amazement, Röntgen found that the rays could pass straight through his hand and cast shadows of his bones on the fluorescent screen. He assumed it as an unknown ray and named as X-rays [82].

In the early 20th century Max Theodor Felix von Laue thought that X-ray has a wavelength similar to interatomic distances in crystals and the crystal should act like a 3D diffraction grating. William Henry Bragg, a pioneer in crystal structure determination using X-ray diffraction, with his son William Lawrence Bragg, derived Bragg's law, which relates the wavelength of X-rays to the glancing angle of reflection and determines when the diffraction should take place [83]. They used this law to

derive the crystal structure and the position of the atoms in the lattice. According to Bragg's law diffraction takes place at specific glancing angles of incidence when the incident electromagnetic wave length is of the same order of magnitude to the spacing between the crystal planes that have a normal vector parallel to the scattering vector. For such scattering direction, the beams reflected of consecutive crystal planes interfere constructively resulting in an interference pattern.

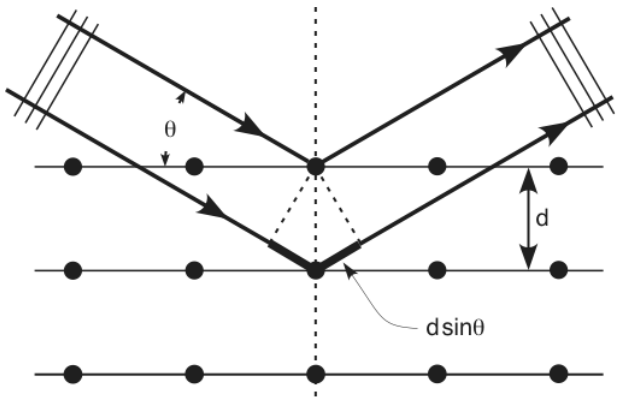

Fig. 4.1: Bragg Diffraction from two adjacent planes.

When X-rays pass through the crystal and scatter from parallel crystal planes, the conditions for constructive interference are:

1. The incident angle should be equal to the scattered angle.
2. The path difference between the two reflected rays should be equal to an integer multiple of their wavelength which is summarized by the following expression:

$$2d\sin\theta = n\lambda \qquad [4.1]$$

Where,

'n' is an integer determined by the order given,

'λ' is the wavelength of x-rays,

'd' is the spacing between the planes in the lattice, and

'θ' is the angle between the incident ray and the scattering planes.

For polycrystalline thin films or powder samples the grains or particles consists of single or multiple crystals oriented in a random manner. The primitive way to estimate the crystal size was first introduced by Scherrer in 1918 and is based on the fact that the peak width is inversely proportional to the crystallite size. This approximation, may be applied when the instrumental broadening is smaller than the line profile (2θ>0.5). The crystal size can be calculated from the following equation:

$$\beta(2\theta) = \frac{K\lambda}{D\ cos\theta} \qquad [4.2]$$

Where,

β = Peak width (FWHM)

λ = Radiation wavelength

D = Crystal size

K = Scherrer constant (dimensionless number)

θ = Incident angle

2θ = Diffracted angle

This equation works for the broad lines and the particle diameter <57nm [84]. Here, the crystal size is determined by using the Miller indices directed normal to the lattice plane. For larger particles, the line profile is less influenced by their size than the smaller particle size. The Scherrer constant, K, varies from 0.62 to 2.08 and depends on how the peak width is defined, the shape of the crystallites and the

crystallite-size distribution. From the SEM images it is obvious that the crystallite shape of NiO and $Ni_{(1-x)}Fe_xO$ are tetrahedral, depend on the oxygen flow during deposition, and decrease in size when increasing the oxygen flow respectively.

Peak broadening can also be caused by inhomogeneous lattice strain (micro-strain). Impurities, point defects, or vacancies can cause local deformation in the crystal lattice spacing and result in peak broadening. In case of homogeneous strain, the change in the d-spacing alters the 2θ position of the diffraction peaks. For example, if we consider an isotropic strain in the sample i.e. all the crystallites are equally compressed and reduce the d-spacing with an amount δd. To satisfy the Bragg condition 2θ needs to shift towards larger angles [85]:

$$2(d - \delta d)\sin(\theta + \delta\theta) = \lambda \qquad [4.3]$$

On the other hand, tensile stress causes a slight increase in d-spacing and shifts the Bragg angle to the lower values.

However, in case of polycrystalline thin films, there is an uneven distribution of the strain allowing some particles to experience compression and others tension. This nonuniform strain has an effect on the grains to be pulled in different directions causing a non-uniform change in the d-spacing. Thereby the ultimate effect of this non-uniform strain is to broaden the resulting diffraction peak. Peaks which are located at higher Bragg angles experience more broadening than those at lower angles.

To get an estimation of the crystallite strain, Stokes and Wilson (1944) developed an empirical relation useful to determine strain from peak broadening [86]:

$$\beta(strain) = 4\varepsilon \, tan\theta \qquad [4.4]$$

Where, ε is the micro-strain.

4.3 Experimental Setup

Two different diffractometers were used for the experiments. Early in the project a Bede D1 XRD system was used. The system had an aged X-ray source that had a rather low intensity. Theta-two theta scans were done from θ =35 to 45 degrees and took a lot of (8 hours scans). During the second part of the project a new Rigaku Smartlab system became available with much better signal to noise ration. Both systems are described below.

4.3.1 Bede D1 System Setup

Since films were deposited on substrates of different geometry we used different ways to mount the sample in the diffractormeter. The first type i.e. a glass sample was mounted at the center of the Goniometer (Aluminium plate) and stuck directly to the gripper on it. On the contrary the quartz sample was stuck on a glass slide (3inchX2.5inch) and then stuck on the Goniometer table. This procedure was followed to avoid peaks of the goniometer table to show up in the XRD scans. The length of the used slit was around 1 inch so some X-ray might miss the sample and we might get some unexpected peak of the goniometer table if we would not use the extra glass slide. For alignment, the sample was moved 5 mm back in the positive-Z direction so that the sample doesn't block the beam. Three slits, 1mm, 1mm, 2mm, were inserted into the optical housing exit, the entrance to the detector stage, and in the detector respectively. Copper was used as a target for the X-ray source and the

operating conditions of the source were -45kV and 35mA. The original intensity was found after a 2theta scan and after a Z scan. The Z position was set to half the original intensity before the Omega alignment scan. Since Brag diffraction peaks were expected around 37^{o}(small) and 43^{o}(large)), a full 2θ-ω scan was run within the range: 35^{o}- 45^{o} with step size 0.01^{o} and count time 100 s/step where the step motors were set on 'Fixed' mode to make it compatible with the count time and to make the noise level insignificant to get sharp and clear peaks.

4.3.2 Rigaku Smartlab System Setup

A standard copper anode tube with tungsten filament is used as an X-ray source with primary beam size of (vertical) x (horizontal): 0.4mm x 12mm. A maximum power of 3 kW can be applied but typically run at 1.76 kW (44 kV, 40 mA) to maximize the life of anode. The Cross-Beam-Optics (CBO) system of the Rigaku SmartLab allows two types of focusing: Brag-Brentano (BB) and Parallel Beam (PB). Since Brag-Brentano optics enables the beam divergence intentionally whereas the parallel beam uses the multilayer mirror to make collimated parallel beam with a beam divergence smaller than ~0.01˚ Different types of selection slits are chosen for the Brag-Brentano (BB) and Parallel beam focusing.

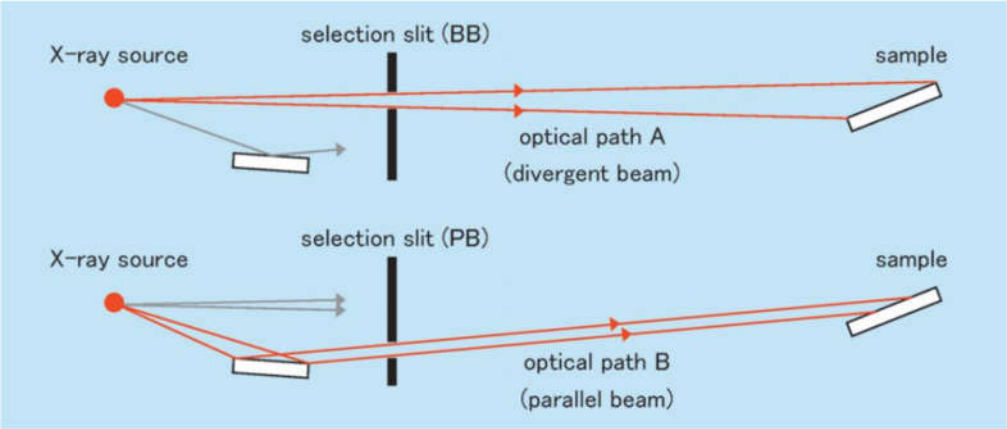

Fig. 4.2: Schematic diagram of CBO optics of Brag-Brentano (BB) and Parallel Beam (PB) focusing (copyright from Rigaku).

Soller slits are used to reduce the beam divergence. The soller slit unit contains many layers of sheet metal oriented parallel to each other in a box. The sheet metal plates are oriented parallel to the plane of diffraction. Soller slit determines the horizontal divergence limit of the beam (typically ~5°) and the resulting low-θ contribution to peaks.

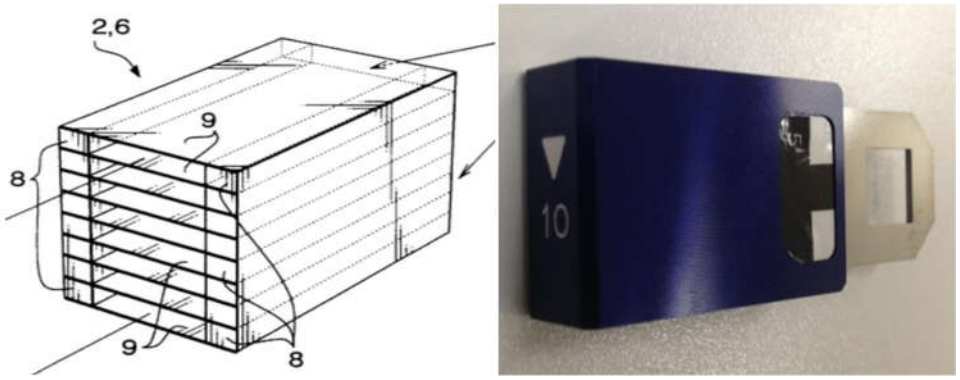

Fig. 4.3: Schematic diagram of Soller slit and image of length limiting slit (10mm).

A Ge monochromator (220 orientation, 2 bounce), typically used for single crystals/thin films, allows only the Kα1 radiation at the expense of intensity and is optional on the incident beam side. A length limiting slit, follows the soller slit, which

simply reduces the horizontal footprint of the beam on the sample. A flat sample stage, uses a special kind of center slit for the optics alignment. The sample stage stands in between of the source arm and detector arm and can be rotated in the azimuthal (φ) direction and be tilted in the χ direction. The χ angle rotates the sample normal out of the plane of incidence. An optional graphite monochromator which eliminates K_β radiation can be installed in the receiving side. Since nickel has a band edge between K_α and K_β energies a K_β filter consisting of a nickel plate is used at the receiving side following the sample stage. This nickel plate also reduces the intensity at ~30%. Next on the detector arm is the parallel Slit Analyzer (PSA) (0.5˚ and 0.114˚) with a similar kind of construction as the soller slit described above. The parallel plates of sheet metal of the PSA are oriented perpendicular to the plane of diffraction though. This component is added in the detector arm to determine (limit) the measurement resolution. A linear NaI scintillation point detector capable of 500,000 cps is attached at the end of the receiving arm.

A computer controlled software was used to perform the optics alignment in the beginning of the measurement. After that a follow-up sample alignment was done. When an optimum z position is achieved with half the intensity of the full incident beam and also the θ angle is positioned so the detector intensity is maximum, the alignment of the sample is complete and the desired measurement process starts. Since for NiO and $Ni_{(1-x)}Fe_xO$ no peaks are found for angles smaller than 30˚, all θ–2θ scans were done from 30˚- 90˚.

4.4 Instrumental Broadening

A high purity commercial standard XRD lanthanum hexaboride (LaB_6) was used to measure the instrumental broadening of the Rigaku Smartlab. A parallel beam $2\theta-\omega$ scan was performed from 0˚- 90˚. A Ge-(220) 2 bounce monochromator was used to remove the $K_{\alpha 2}$ from the incident beam. The FWHM of all the peaks was plotted against the 2θ angles and a polynomial trendline was also drawn which followed the course of the peak profiles.

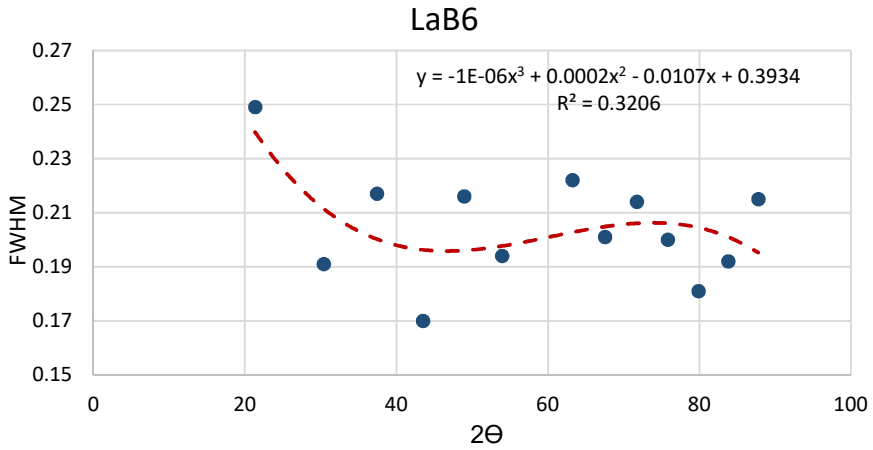

Fig. 4.4: Typical instrumental broadening trendline of Rigaku Smartlab.

From the above plot we can conclude that for the Rigaku Smartlab XRD system the typical instrumental broadening is around 0.21˚. For the peak profile fitting the pseudo-Voigt function was used. The formula for the residual peak broadening, β after subtracting the instrumental broadening that corresponds the pseudo-Voigt function is,

$$\boldsymbol{\beta^2 = (FWHM_{sample} - FWHM_{inst})\sqrt{FWHM_{sample}{}^2 - FWHM_{inst}{}^2}} \qquad [4.5]$$

4.5 Measured Results and Data Analysis

For our XRD peak analysis we performed two types of 2θ scans, i.e. a $\theta-2\theta$ scan and

a 2θ-ω scan. For the latter, the glancing angle of incidence was kept constant during the measurement while for the latter both θ and 2θ were scanned. The 2θ-ω scan of each type of sample are plotted- after removing the background counts per seconds. Results for the thick samples are shown in Fig. 4.4 for NiO and in Fig. 4.5 for NiFeO. Results on thin NiO films are shown in Fig. 4.10 and Fig. 4.11. The different lines show the data of samples sputtered at different oxygen gas flow. Al samples reported on in this section were sputtered at high pressure, i.e. around 8 mTorr.

4.5.1 High Pressure Thick Films (>250nm) of NiO and $Ni_{(1-x)}Fe_xO$ Sputtered at 7-8mTorr

The conventional $\theta-2\theta$ scan shows the peaks from the crystals plane which are parallel to the substrate. However conventional $\theta-2\theta$ scans of thin films have a poor signal to noise ratio and can show strong peaks of the substrate. To increase the sensitivity of the measurement method one often does a $2\theta-\omega$ scan instead. Another type of measurement, 2θ, which means by using a grazing incident beam at fixed angle, for example $\theta = 2$ and moving only 2θ one can enhance the signal of the thin film. At grazing incidence, the path length of the X-ray beam through the thin film is much larger than at large angles. Also, the penetration depth of the x-ray beam is less at grazing incidence. This will lower peaks and background of the substrate. Furthermore, diffraction peaks of the substrate are suppressed or are not observed as the scattering vector is no longer perpendicular to the substrate Sometimes, however, some unobservable substrate peaks are visible in the 2θ plots that are not present in the regular $\theta-2\theta$ scan. We did this kind of scan on the thick

samples we made and got some stronger peaks in the 2θ plots. The results of the 2θ scans are shown in Fig. 4.5 while Fig. 4.6 gives the $\theta-2\theta$ scans for the high pressure thick film oxygen series.

Analyzing all the graphs below we can conclude that almost all the films have a dominating (111) texture. In the 2θ scan of NiO deposited with 10% oxygen flow the peak at 43.2˚(200) and at 79.5˚(222) almost disappeared which is consistent with the $\theta-2\theta$ scan of the same sample. It seems that when the films get thicker only one i.e. {111} plane prevails and suppresses the others. To get a better idea of the texture of all of these films we did pole figure analysis which is explained below in sec 3.

Since these samples are polycrystalline we used the Scherrer equation on the $\theta-2\theta$ data to estimate the crystal size of the samples. The results are summarized in Table 4.2 below. For the result shown in Table 4.2 we assumed that all broadening results from the crystal size effect. In other words, effect of micro-strain on peak width was ignored.

Since 2θ scans are performed at grazing incidence angle they are very sensitive due to the limited penetration depth of the X-ray beam in the substrate. The diffracted beams come from the crystallites tilted with respect to the substrate plane and using the peak width of a 2θ plot to determine the crystal size provides information of the crystallites in a direction inclined to the substrate normal.

The crystal size determined from the Williamson Hall analysis resulted in negative crystal size values which is not physical. This could be due to strong texture in these films. Strictly speaking the Williamson Hall plot technique can only be applied to non-

textured isotropic samples. No further attempts were made to analyze both crystal size and micro-strain simultaneously.

Another analysis was performed on the $\theta-2\theta$ data. Neglecting the effect of crystal size on the peak broadening, we calculated the micro-strain from the peak width. Since the radius of the Fe^{2+} is smaller than the radius of the Ni^{2+} there should be more compressive strain in Fe doped NiO than only NiO. In table 4.3 the calculated micro-strain shows that for high oxygen flow NiFeO it is higher than others and it increases with 2θ as the FWHM increases. In addition, in terms of Oxygen vacancies, more oxygen vacancies increase the micro-strain for NiO whereas for NiFeO more oxygen vacancies decrease.

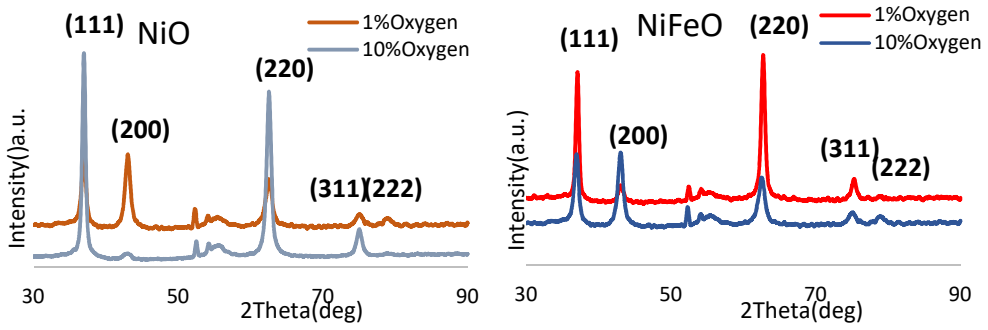

Fig. 4.5: 2Theta plot of NiO (left) and $Ni_{81}Fe_{19}O$ (right).

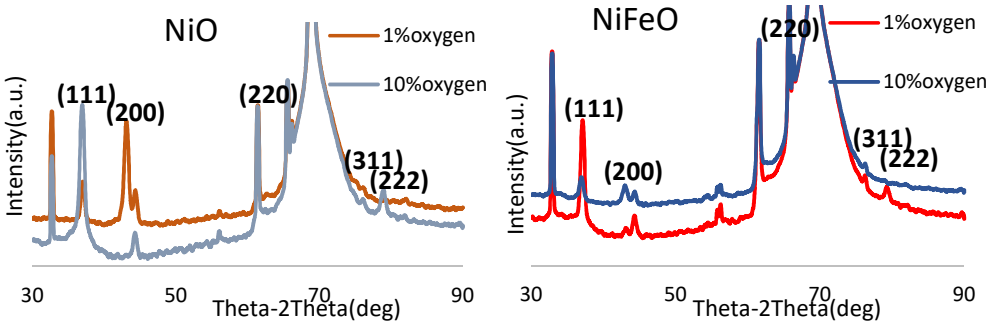

Fig. 4.6: Theta-2Theta plot of NiO (left) and $Ni_{81}Fe_{19}O$ (right).

Table 4.1: Crystal size calculated from $\theta-2\theta$ scan of different NiO and NiFeO thick films. The largest peak for each sample are underlined and the angles are shown in between the braces.

Crystal plane	$Ni_{81}Fe_{19}O$(0.5 sccm O_2)	$Ni_{81}Fe_{19}O$(5 sccm O_2)	NiO(0.5 sccm O_2)	NiO(5 sccm O_2)
(111)	<u>23.214(37.24˚)</u>	<u>15.947(37.08˚)</u>	21.397(37.16˚)	<u>21.187(37.1˚)</u>
(200)		9.217(43.1˚)	<u>20.61(43.22˚)</u>	
(220)	<u>9.747(62.9˚)</u>	6.502(63˚)	6.4915(62.7˚)	3.893(62.62˚)
(311)		3.5296(76.5˚)		
(222)	10.702(79.42˚)			10.472(79.12˚)

Table 4.2: Micro-strain calculated from $\theta-2\theta$ scan of different NiO and NiFeO thin films with the angles of the peaks in between the braces.

Crystal plane	$Ni_{81}Fe_{19}O$(0.5 sccm O_2)	$Ni_{81}Fe_{19}O$(5 sccm O_2)	NiO(0.5 sccm O_2)	NiO(5 sccm O_2)
(111)	0.28(37.24˚)	0.41(37.08˚)	0.31(37.16˚)	0.305(37.1˚)
(200)		0.614(43.1˚)	1.027(43.22˚)	
(220)	0.41(62.9˚)	0.612(63˚)	0.312(62.7˚)	0.274(62.62˚)
(311)		0.95(76.5˚)		
(222)	0.304(79.42˚)			0.615(79.12˚)

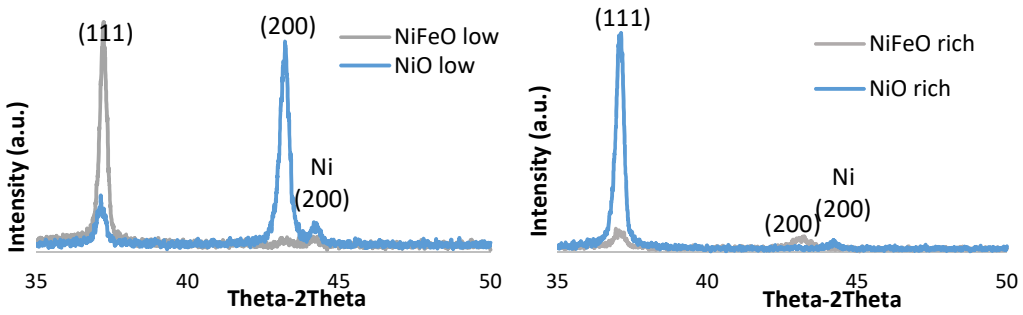

(a) (b)

Fig 4.7. Comparison of theta-2theta plot (with monochromator) of NiO and NiFeO at (a) low oxygen flow and (b) high oxygen flow.

Fig.4.7. shows the theta-2theta scan of the NiO and NiFeO samples with both the low oxygen flow and high oxygen flow deposition process. For the low oxygen flow

samples, either NiO or NiFeO, both of them show the metallic Ni peak at around 44.1˚. A little bit of peak shifting is noticed for the NiFeO sample at the low oxygen concentration towards the positive angle comparing with the NiO low oxygen flow samples. This peak shifting is attributed to the doping of Fe in the NiO. On the other hand, for the high oxygen flow samples both the NiO and NiFeO (111) peak shifted towards the negative angle and between them the NiFeO (111) peak shifted slightly more towards the negative angles compared to the NiO (111) peak. This peak shift towards the negative or low angles is attributed to the higher oxygen concentration in the NiO and NiFeO samples. It is also noticed that for the high oxygen flow NiFeO sample no metallic Ni peak was observed. We think when Fe is added in the NiO more than a certain amount it sits on the metallic Ni sites and reduces the metallic phase of Ni in NiO.

It is also observed from the above figure that more oxygen flow changes the crystal orientation. From the Fig. 4.6(a) it is seen that for low oxygen flow the prominent crystal orientation for NiO is the [100] plane whereas for the NiFeO it is the [111] plane. For high oxygen flow samples NiO has the opposite effect e.g. it has a very prominent [111] crystal plane orientation. In case of NiFeO there are two planes [111] and [100] have very weak orientation. This phenomenon is attributed to the formation of some oxides with Fe (maybe). To verify this a further XPS study of the high oxygen flow NiFeO is required.

4.5.1.1 Preferred orientation analysis

Pole figure analysis are an XRD measurement technique to determine the texture of the thin film samples. For the measurements the θ and 2θ are fixed at particular

angles corresponding to a specific d-spacing. In our case, we fixed the 2θ position at 37.2˚(111), 43.2˚(200), and 63.2˚(220). Then the diffracted intensity is measured as a function of α and β. α is the tilt angle, χ, from the surface normal direction to the plane of incidence. β is the azimuthal angle, φ angle, around the sample surface normal direction. α is scanned from 0-90 degrees and β is scanned from 0˚-360˚. To reduce the effect of sample size and geometry the background signal is measured at ±1.5˚ of the peak position. This background is subtracted from the measured intensity at the peak position.

For the preferred orientation analyses, we used the pole figure analysis method on the NiO and the Fe doped NiO samples. In the 3D-Explore software the file is loaded and analyzed by doing, the background correction, the smoothing of the data, and the background subtraction. In addition, the intensity scale of the pole figures was adapted to enhance its ring pattern. We found (111) texture in the $Ni_{81}Fe_{19}O$ with the low oxygen flow (0.5 sccm) means low oxygen partial pressure sample and (200) texture in the $Ni_{81}Fe_{19}O$ with the high oxygen flow (5 sccm) means high oxygen partial pressure sample. For the NiO with high oxygen flow (5sccm) the (111) texture at 37.2˚ is dominating.

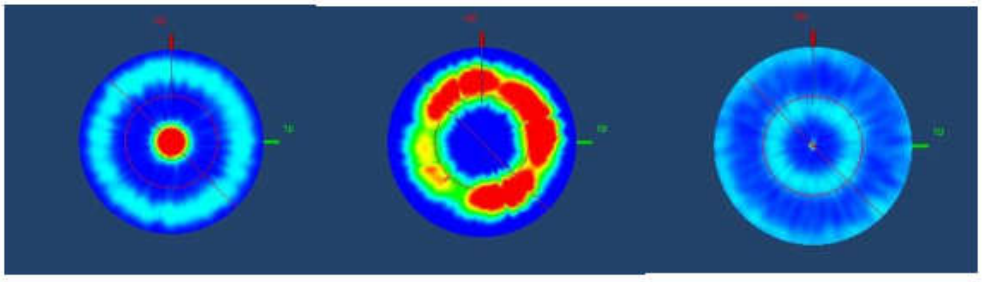

(111) (200) (220)

Fig. 4.8: Pole figure of $Ni_{81}Fe_{19}O$ with low oxygen flow.

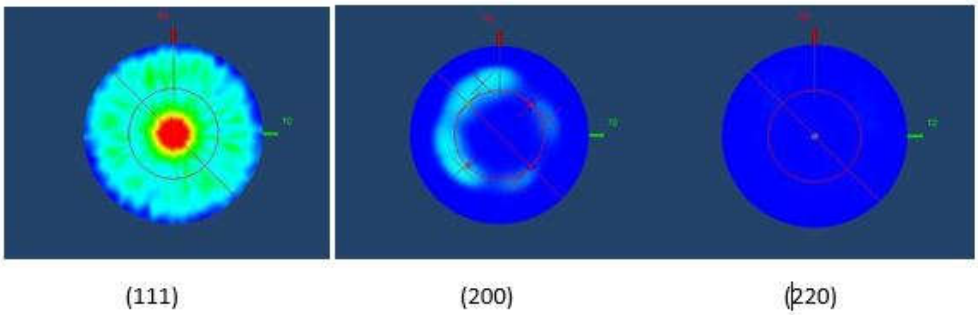

Fig. 4.9: Pole figure of $Ni_{81}Fe_{19}O$ with high oxygen flow.

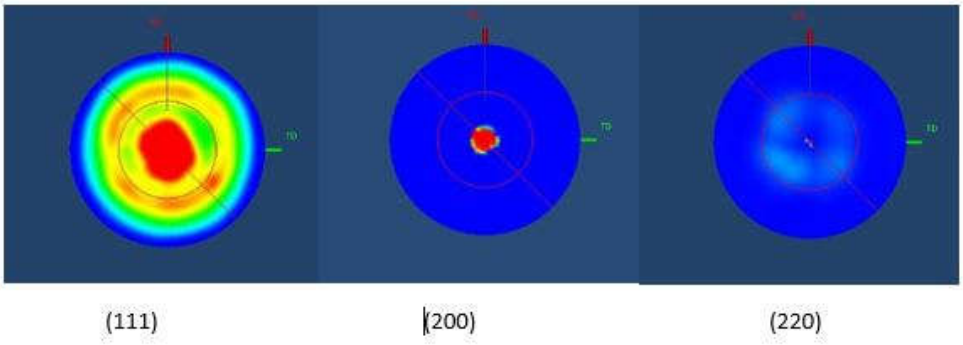

Fig. 4.10 : Pole figure of NiO with low oxygen flow.

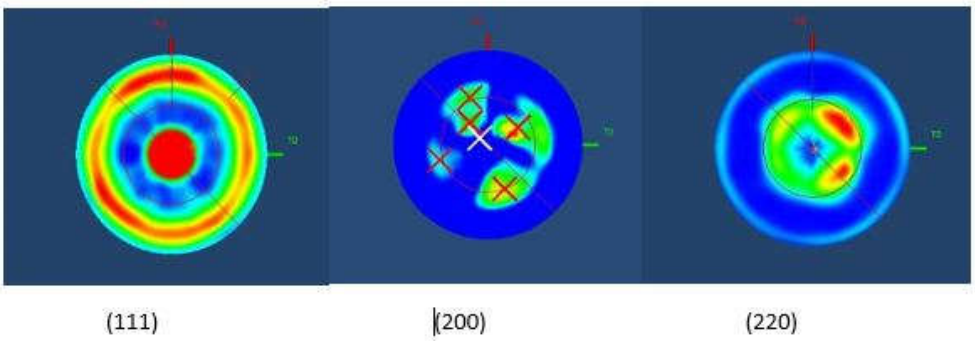

Fig. 4.11: Pole figure of NiO with high oxygen flow.

4.5.2 High Pressure Thin Films (<70nm) Sputtered at 7-8mTorr

For the thin films, it was very difficult to get all the peaks through the θ–2θ scans. To get an idea of the peak positions and their existence we first performed a 2θ scan on

samples sputtered on glass. The 2θ plot below (see fig. 4.12) shows that the peak heights are decreasing gradually with the increasing flow of oxygen in the deposition process. The observed peaks are consistent with a rocksalt crystal structure. Note that the film sputtered at 7 sccm oxygen flow is much thinner than the other samples, i.e. 20-22 nm compared to the 50-70 nm thickness of the other films. The θ–2θ plot is shown in Fig. 4.13. The low oxygen concentration samples have a (200) texture. For medium oxygen concentrations (1.25 to 3.5 sccm O_2) the films have a (111) texture while for high oxygen flow the samples again have a (200) texture.

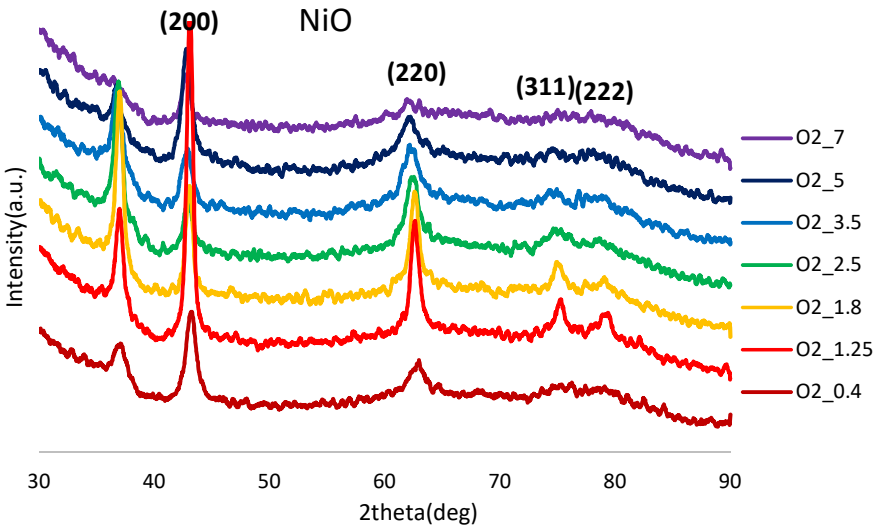

Fig. 4.12: 2Theta plot of NiO (thin films) with different Oxygen flow. (Value shown on the right in sccm)

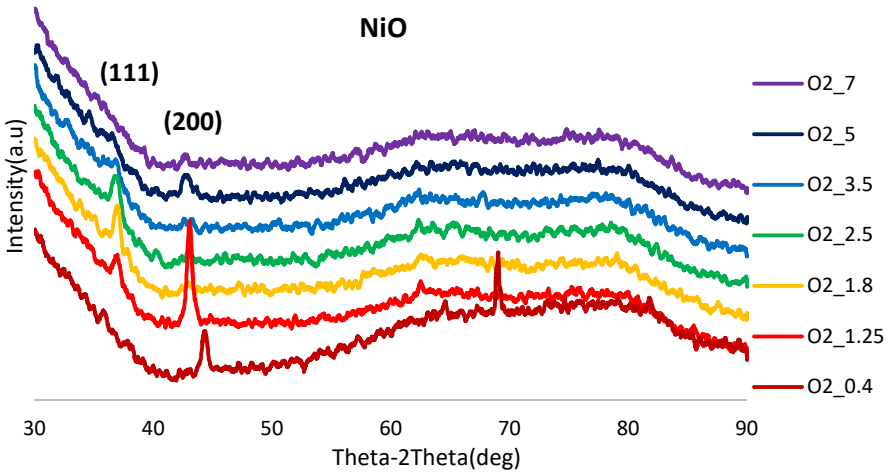

Fig 4.13: Theta-2Theta plot of NiO (thin films) with different Oxygen flow. (Value shown on the right in sccm.)

4.5.3 Low Pressure Thin Films Sputtered at 1mTorr

The XRD results for the low pressure thin film series are shown in Fig. 4.13 and 4.14 below. These were measured with the old XRD equipment. The measurement time was long (8 hours). The background was removed by drawing a trendline in MS Excel and subtracting that from the measurement data. Fig. 4.14 shows the data for $Ni_{90}Fe_1O_{(100-\delta)}$ and Fig. 4.15 shows the data for $Ni_{81}Fe_{19}O_{(100-\delta)}$. The spikes in the graph are believed to be caused by noise. The 10% Fe samples have always a (200) texture for all oxygen flows. For the 19% Fe samples the texture is (200) at medium oxygen flow and both (200) and (111) at high oxygen flow. The latter is consistent with the results on the high-pressure thick films.

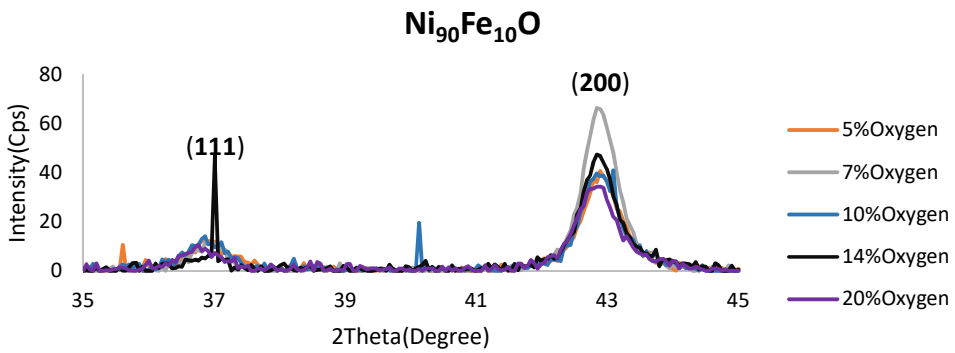

Fig. 4.14: A 2θ–ω scan of $Ni_{90}Fe_{10}O$.

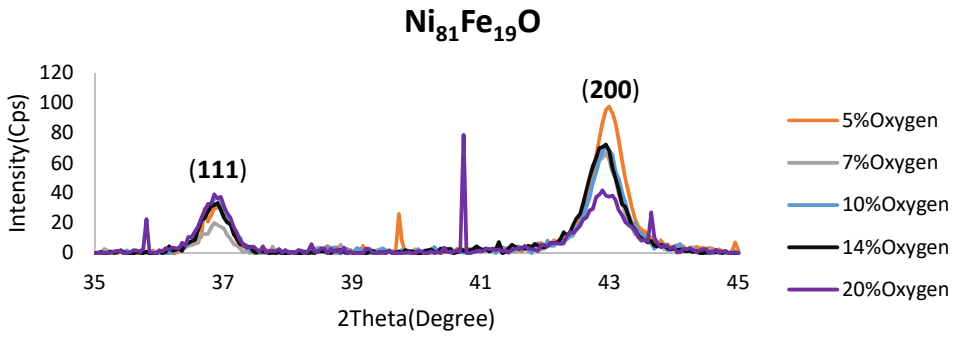

Fig. 4.15: A 2θ–ω scan of $Ni_{81}Fe_{19}O$

The crystal size was determined from the peak width for both samples and the results are summarized in the Table 4.4 given below.

Table 4.3: Crystal size calculated from 2θ–ω scan for (200) peaks of Fe-doped NiO:

Oxygen Flow	Crystal Size(nm)	
	$Ni_{81}Fe_{19}O$	$Ni_{90}Fe_{10}O$
5%	20.442	16.682
7%	19.734	18.264
10%	18.873	16.961
14%	18.668	17.916
20%	16.487	15.383

4.6 Conclusion

Since the low-pressure samples were not studied through the pole figure analysis but from the XRD data we can conclude that for the $Ni_{81}Fe_{19}O$ and for $Ni_{90}Fe_{10}O$ always the (200) texture wins, although it varies depending on the oxygen flow from low to

high. The lattice parameter of the conventional unit cell is calculated 4.219A (avg). For the high-pressure samples using the pole figure analysis it is obvious that {111} texture dominates the others.

V. ELECTRICAL PROPERTIES

5.1 Introduction

In this chapter the results of linear 4pp measurements are reported. The measured current and voltages are converted in a sheet resistance. This sheet resistance is used to calculate the resistivity of the TMO for currents parallel to the substrate. First the measurement technique is explained. This is followed by the measurement results on the high-pressure thin NiO series and the high-pressure thick oxygen flow series.

5.2 Basics of Four-Point Probe

Originally, Wenner first proposed the four-point probe method by in 1916 to measure the earth's resistivity. In Geophysics this measurement technique is referred as Wenner's method. In semiconductor metrology, Valdes adopted it for semiconductor wafer resistivity measurements in 1954. The probes are generally collinear, i.e., arranged in-line with equal probe spacing, but other probe configurations are possible. In a four-point probe four needle type probes are used to measure the resistivity of the p-n junctions, semiconductors, insulators etc. Four sharp probes are placed on a flat surface of the material to be measured so that all four probes can touch the surface. The inner two electrodes measure the floating potential and the outer electrodes measure the currents. If the flat surface is large enough then it is considered as semi-infinite volume. For a good contact with the probes and the surface and not allowing the minority carrier injection the surface of the material where the probes rest may be mechanically lapped.

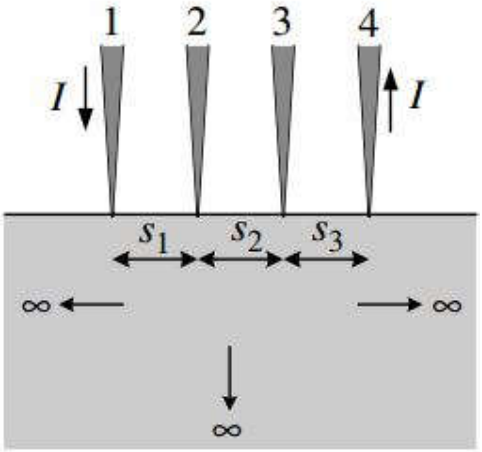

Fig. 5.1: Schematic diagram of Four-point probe.

The figure above shows a schematic view of four-point probe where four probes stands side by side maintaining a particular distance from each other. If the distances from each other are identical i.e. S_1=S_2=S_3 then the resistivity, ρ, is given by,

$$\rho = 2\pi SF\frac{V}{I} \qquad [5.1]$$

Where,

S = Space between two adjacent probes.

F = Correction Factor for the thickness of the thin films.

V = Voltage between the two inner probes.

I = Current flows through the outer probes.

For samples that are thinner than the probe spacing the correction factor, F, is defined by,

$$F = \frac{t/S}{2\ln 2} \qquad [5.2]$$

Combining equation (3.13) and (3.14) we get,

$$\rho = \frac{\pi}{\ln 2} t\frac{V}{I} = 4.532t\frac{V}{I} \qquad [5.3]$$

With the condition $t \leq S/2$.

The sheet resistance of the uniformity doped samples are given by,

$$R_{sh} = \frac{\rho}{t} \qquad [5.4]$$

In order to use this four-point probe method in thin films it is necessary to assume that:

1. The resistivity of the material is uniform close to the area that the probes cover.

2. If there is minority carrier injection into the semiconductor by the current-carrying electrodes most of the carriers recombine near the electrodes so that their effect on the conductivity is negligible. (This means that the measurements should be made on surfaces which have a high recombination rate, such as mechanically lapped surfaces.) [87]

3. The surface on which the probes rest is flat with no surface leakage.

4. The four probes used for resistivity measurements contact the surface at points that lie in a straight line.

5. The diameter of the contact between the metallic probes and the semiconductor should be small compared to the distance between the probes.

Contact and lead resistances are cancelled out by the four point method [88]-[90], however the contact resistance can still cause errors if these are producing enough heat. Inhomogeneous heat produced by the contacts can cause temperature gradients in the thin film sample. These temperature differences can cause thermal voltages resulting in systematic errors. Thus, it is imperative that the contacts should have low resistance. Swapping the position of the current and voltage electrodes and changing their polarity and averaging the results can correct for some of those thermos electric effects. Instrumental dc offsets in source, meters, and switching unit

also contribute to the error. This can also be easily corrected by measuring for two different current values and subtracting the results. This problem can be corrected by reversing the flow of current through the sample.

For the highly resistive films studied in this thesis, it is important that the input resistance of the voltmeter is large compared to the sample, otherwise most of the sourced current will flow through the voltmeter shunting the sample resulting in faulty measurement results. The use of electrometers or buffer amplifiers with a large input resistance (10^{14} Ohm) in between the sample and the voltmeter can reduce shunting but will increase time constant of the setup requiring longer waiting times after a current change before the system is stable. The noise level on the voltmeter signal is higher for the high resistive samples and mainly originates from Johnson noise. For our high resistance samples, the noise is on the order of hundreds of microvolts. For the very high resistance samples the low level of the voltage caused by the small current is comparable to the signal noise and also adds to the error. By using the proper shielded cables and low thermal contactors, as well as making single point grounding, the noise originating from other equipment can be reduced [91]. In that case Johnson noise is the limiting noise left. The electronic setup used for the electrical characterization is shown in the figure below. For the Keithley four-point probe setup, the main source of noise is the Johnson noise.

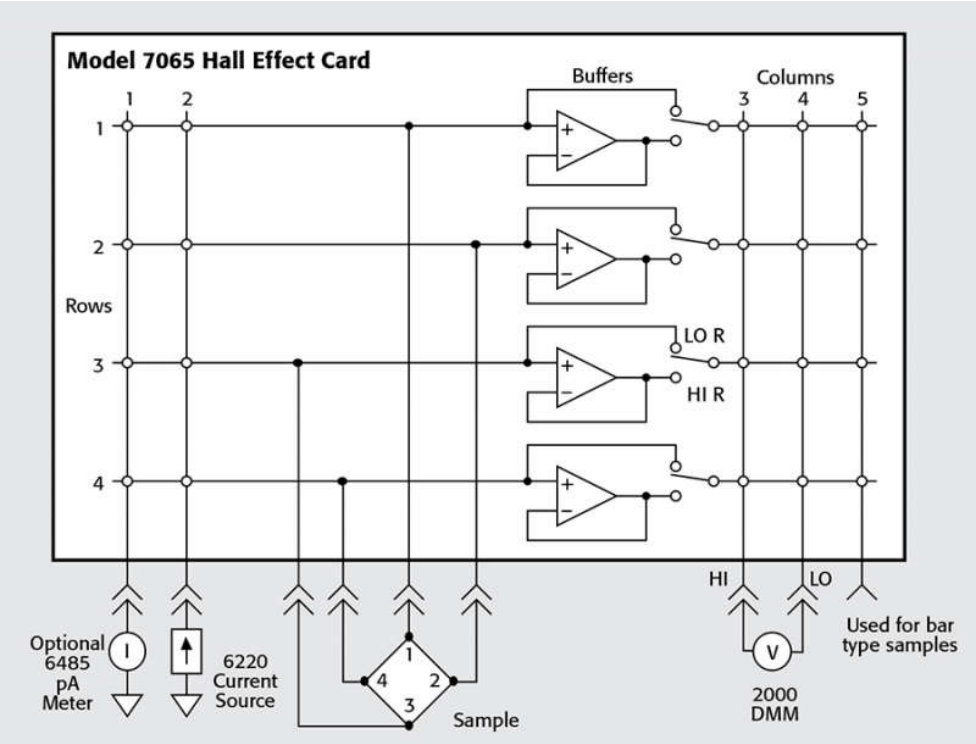

Fig. 5.2: Schematic of 7065 Hall effect Card.

5.2.1 Experimental Data

With the four-point probe we measured the resistivity of the NiO samples sputtered at high pressure. Sample deposited at different Oxygen flow were investigated. The resistivity is shown in Figure 5.3 below (Experimental data showed in Appendix E):

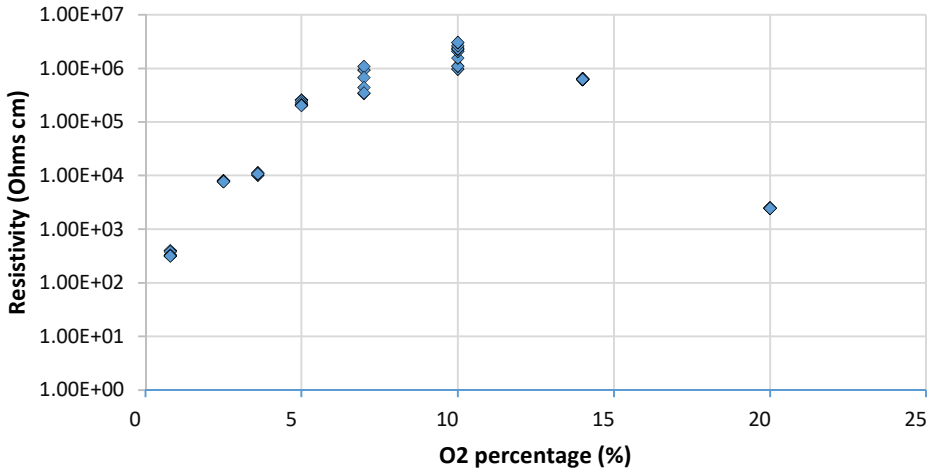

Fig. 5.3: Graphical representation of Resistivity of high pressure NiO thin film series.

Table 5.1: Calculated resistivity of NiO and $Ni_{81}Fe_{19}O$ thick films.

Sample Name	NiO(1%oxygen)	NiO(10%oxygen)	$Ni_{81}Fe_{19}O$(1% oxygen)	$Ni_{81}Fe_{19}O$(10% oxygen)
Resistivity (Ω cm)	0.30128	15922.5	5.3E-2	0.48875

5.3 Conclusion

The measurement result of the four-point probe shows that the resistivity of NiO increases with the increment of oxygen concentration. The resistivity gets saturated at 5sccm oxygen flow which we think is close to perfectly stoichiometric sample. For higher or lower oxygen flow samples the resistivity is lower; in our view this could be evidence of changing the type of carrier i.e. from p-type to n-type or it might be from metallic state to semiconductor state. To verify the latter the resistance of a sample made at low oxygen flow rate was measured by four-point probe at both room temperature and liquid nitrogen temperature. The resistance increases for lower temperature. So, the low oxygen flow samples are also semiconductor like for a current parallel to the substrate. For further verification a Hall measurement needs to be performed.

VI. MAGNETIC PROPERTIES

6.1 Introduction

Twagirayezu et al. found that the properties of reactive RF sputtered NiO and $Ni_xFe_{1-x}O$ sample depend on the oxygen flow during deposition. Samples sputtered at low oxygen flow have a magnetic moment at room temperature. This is an important result as it could mean that low oxygen NiO and $Ni_xFe_{1-x}O$ could be ferromagnetic possibly providing a means to detect the low resistive filaments in RRAM devices by magnetic force microscopy. Systematic switching studies of RRAM devices are currently challenging. To detect the position and size of the filaments, the top electrode is removed and the sample device is characterized by conductive atomic force microscopy. So, this is a destructive analysis method. In the case the filaments are magnetic, one might be able to detect them with magnetic force microscopy: so the top electrode no longer would have to be removed allowing for systematic studies of how filament position and size changes over the life time of the device. These types of studies are not possible by above described conductive-AFM approach as the device is destroyed upon removing the top-electrode. If the filaments carry a magnetic signature MFM can be applied to locate the position and possibly size of the filament through the metal top electrode.

To confirm the preliminary measurements of Twagirayezu, the magnetic properties of NiO and $Ni_{1-x}Fe_xO$ at room temperature were studied by Magneto-Optical Kerr magnetometry. The MO measurement method is approximately a factor 1000 more

sensitive than the Vibrating Sample Magnetometry used by Twagirayezu. The first part of the chapter contains an introduction to the MO Kerr effect. As small signals were expected, a thorough analysis of the MO Kerr measurement technique was conducted. Because a coherent laser is used as a light source, Fabry-Perot interference in the modulator causes large offsets in the 1ω and 2ω signal. It is shown that these offsets can impact the measurement accuracy of the MO-signals. In addition, the stability of the PEM was studied. In particularly the time dependence of the retardation was monitored after the retardation values were suddenly stepped up on the PEM controller. The step response indicates two different time responses: one is believed to be of electronic nature and the other is caused by the slight temperature increase caused by internal power dissipation in the PEM's transducer.

6.2 Theory of MO-Kerr Effect

Magneto-Optical (MO) effects arise from an optical anisotropy of the materials which can change the polarization state of incident linearly polarized light into rotated elliptically polarized light upon reflection from or transmission through a magnetic medium.

Light is a transverse electromagnetic wave which can be manipulated optically into plane, circularly or elliptically polarized light. For linearly polarized light the electric field only changes in magnitude is not in direction. The plane that contains the electric field E and the direction of propagation is called the plane of polarization. If the electric field is polarized in the plane of incidence, the light is referred to as p-polarized light. Conversely, if the electric field is polarized perpendicular to the plane

of incidence, it is referred to as s-polarized light. EM-waves for which the magnitude of the electric field is constant but for which the direction of the electric field changes as a function of time and space are referred to as circular polarized light. Depending on the rotation of the electric field vector E, rotating in either a clockwise or an anticlockwise direction one speaks of Right circular polarized or left circular polarized light. EM-waves for which both the magnitude and the direction change as a function of time and space are referred to as elliptically polarized light.

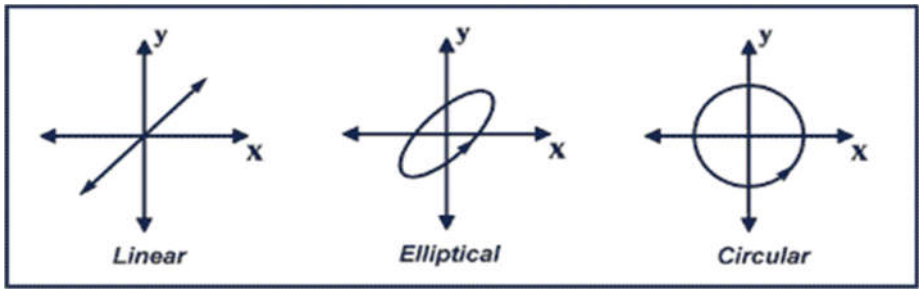

Fig. 6.1: linear, elliptically and circularly polarized light.

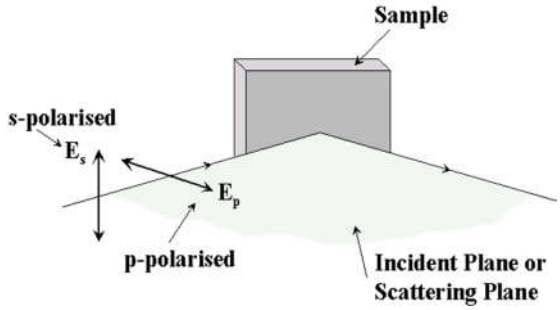

Fig. 6.2: p- and s-polarized light.

When the incident wave vector $\boldsymbol{k_i}$ has a resolved component along the direction of the magnetization $\boldsymbol{M}$ within the sample, inequivalent interactions occur for right and left circularly polarized light. This effect stems from the spin-orbit and exchange interactions within the medium. The presence of both type of interaction gives rise to off-diagonal terms in the dielectric tensor which governs the reflectivity. Thus, in

general, a plane-polarized beam reflected from or transmitted through a magnetic medium, becomes elliptically polarized with its principal axis of polarization rotated away from the plane of the incident polarization. Due to the high magnetic susceptibility in ferromagnetic materials the effect is particularly large. In the case of transmission, this is referred to as the Faraday effect and a field-dependent rotation of the polarization plane occurs. In the case of reflection this phenomenon is known as the magneto-optical Kerr effect, with both the refractive index and the reflectivity being dependent on the handedness of the polarization, and therefore the light is elliptically polarized in addition to being rotated.

Upon reflection one distinguishes between three Kerr effects depending on the relative orientation of the magnetization *M* with respect to the plane of incidence of the light: The longitudinal, transverse and polar Kerr effects.

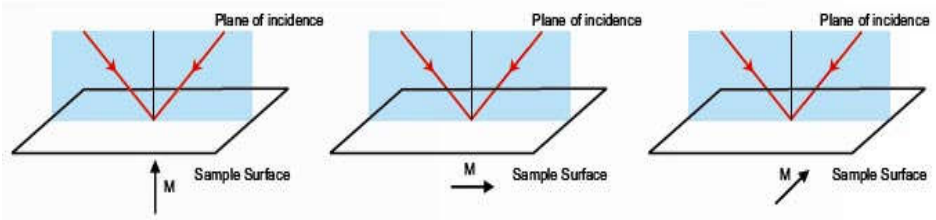

Fig. 6.3: Polar (left), longitudinal (middle) and transverse (right) kerr effect.

For all of these geometries, the magnetization in the sample is parallel to the applied magnetic field. In the longitudinal Kerr-effect there is no rotation at normal incidence and for smaller angles the magnitude of the rotation increases with the angle of incidence. By contrast, in the polar geometry a rotation can be obtained perpendicular incidence. This can be understood by noting that the magnitude of the Kerr rotation is determined by the projection of $\boldsymbol{k}$ along $\boldsymbol{M}$. In the longitudinal

geometry $\boldsymbol{k.M}$ vanishes at normal incidence, whereas in the polar geometry $\boldsymbol{k.M}$ is non-zero at perpendicular incidence.

As light only penetrates metals a distance of approximately equal to 10-20nm, the Magneto-Optical measurement technique is often used to measure the magnetic properties of the surface; in particularly for high conductive bulk samples, it is only the material within a few tens of nanometers of the surface that contributes to the observed rotation. In the case of ferromagnetic transition metals this rotation may be as large as 0.3 degrees. For films thin on the length scale of the skin depth, the total rotation is approximately proportional to the film thickness and it is therefore experimentally feasible to detect the rotation induced by a fraction of a single monolayer. An Fe layer down to 0.7 mono-layer is easily detectable by the MO Kerr measurement technique. Below this Fe is shown to no longer be ferromagnetic and the ferromagnetic signature is lost in the MO-Kerr signal.

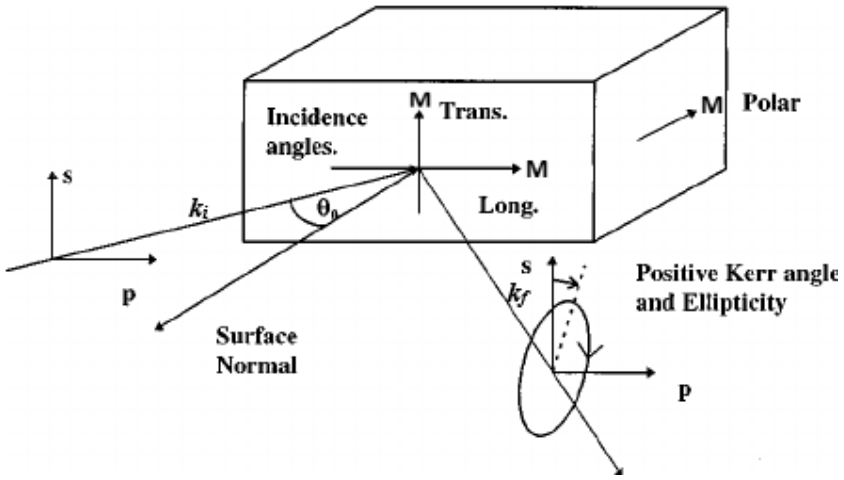

Fig. 6.4: Kerr rotation and ellipticity of reflected light.

The magnetic medium has different refractive indices for these two polarized modes. Therefore, the two circular modes travel with different velocities and attenuate

differently in the material. Upon reflection from the material, the two modes recombine to produce the Kerr rotation and ellipticity. The macroscopic description of Kerr effects relies on the two modes having different refractive indices within the material. The general form of the dielectric tensor which represents the effects of a magnetic medium is given by-

$$\boldsymbol{\varepsilon} = \boldsymbol{\varepsilon_0}\begin{pmatrix} \mathbf{1} & \mathbf{-iQ_z} & \mathbf{iQ_y} \\ \mathbf{-iQ_z} & \mathbf{1} & \mathbf{-iQ_x} \\ \mathbf{iQ_y} & \mathbf{-iQ_x} & \mathbf{1} \end{pmatrix} \qquad [6.1]$$

where $Q_{x,y,z}$ is the Voigt magneto optic constant which describes the magneto optical effect and ε_o is the permittivity constant in air. This Voigt term is to the first order proportional to the magnetization of the material. It is this complex Voigt term (the off-diagonal terms) which generally modifies the polarization. Basically, what MOKE measures directly, is the magneto optic response of the medium, which is a change in the incident polarization of the light. This magneto optic response consists of two parts: a change in the polarization of the in-phase component of the reflected light which gives rise to the rotation, and a change in the polarization of the out-of-phase component of the reflected light which gives rise to the ellipticity. The MO effect is caused by a combination of spin orbit interaction and exchange interaction. Spin orbit interaction is present in most materials and is larger for elements with a larger atomic mass. Although exchange interaction can be induced by a magnetic field, exchange interaction is large ferromagnetic materials.

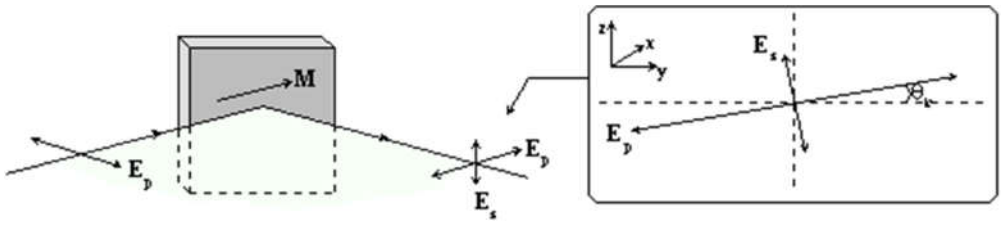

Fig. 6.5: Reflection of p-polarized light of a magnetic sample.

Although it is possible to measure magneto-optical effects by two polarizers and a wave-plate, the 1/f noise of detectors and amplifiers limits the signal to noise ratio with this approach. Better restuls are obtained by using a modulation technique such as a Photo-elastic modulators (PEM) [92]-[94]. They are often used to measure the magneto-optical Kerr or Faraday effects of thin ferromagnetic films and multilayers [93][94]. The state of polarization (SOP) of the light incident on the sample or transmitted or reflected by the sample is modulated by a standing sound wave in the PEM's optical head [95]-[97]. Subtle changes in the polarization induced by the sample such as Kerr rotation and ellipticity are converted to an intensity variation using polarizers [93][94]. This allows for a determination of the magneto-optical (MO) effects with a S/N ratio limited by the shot noise of the light source [98]-[101]. For single axis modulators the resonance condition is only fulfilled for one axis resulting in a uniaxial time dependent stress; the refraction index for light linearly polarized parallel or perpendicular to this modulation axis is modulated [102]. Because of Poisson's ratio, periodic strain variations are also expected perpendicular to this modulation direction resulting in a thickness modulation of the optical head's prism [103]-[105]. The latter causes a modulation of the optical path length of a ray passing through the modulator resulting in intensity variations of the transmitted

light when a coherent light source is used. This effect is similar to Fabry-Perot interference in a thin film; intensity variations several orders of magnitude larger than the intensity variations caused by the MO Kerr effect can be observed [103]-[105]. The large offsets of the AC detector signals originating from this interference effect poses problems on the MO measurement accuracy via several mechanisms including:

1. The large offsets in the 1ω and 2ω components of the detector signal will force one to use a higher range setting on the lock-in amplifier losing sensitivity and reducing S/N ratio.
2. Lab temperature, laser intensity, and laser beam direction fluctuate and can have a significant impact on the magnitude of the 1ω and 2ω detector signal offsets resulting in significant signal drifts. This effect is similar to signal offsets observed when incorporating a PEM in a longitudinal Kerr measurement setup [106]-[108].

Although the interference effect can be avoided by using an incoherent light source or other techniques [105], the use of lasers in MO-Kerr setups allows for faster measurements in particularly when scanning is involved and has advantages when one wants to focus the light beam to a diffraction limited spot for local measurements [99][109]-[112]. We therefore investigate the PEM interference effect in more detail in particularly the dependence on PEM tilt angle and polarizer angles are investigated and the consequences for the MO Kerr technique are discussed.

6.3 Experimental Setup

The Magneto-Optical Kerr setup used for the experiments is provided in Fig. 6.6 below.

A Melles Griot intensity stabilized He-Ne laser (05 STP901) without beam shaping optics is used for the light source (632.8 nm, 1-hour power stability: +/- 0.2% rms, linearly polarized). This laser includes controls needed for monitoring and controlling laser power. Its pointing stability has not been determined yet but similar intensity controlled lasers have a pointing stability of 0.2 milli-radians after significant warming up time [113]. The optical components are an aluminum mirror, a quarter wave-plate, a polarizer, a photo-elastic modulator, an analyzer, and a silicon photo-detector, all mounted on top of a vibration isolation table. Glan-Taylor prisms (MGTYS15, Karl Lambrecht) mounted in a Newport servo motor stage that can be controlled by a computer (step size 0.5 mdegr.) are used for the polarizer and analyzer. The orientation of the fast axis of the quarter wave plate is at 45 degrees with the horizontal so the horizontal linearly polarized laser light is converted into circularly polarized light just before the polarizer. Light reflected from the polarizer or PEM will one more time pass the quarter wave plate and be vertical linearly polarized when heading back to the laser preventing it from entering the laser cavity and destabilizing its intensity control. The PEM is a single axis Hinds PEM-90. It consists of a transparent prism mounted to a piezo-electric transducer. The transducer is used to generate a periodic time dependent physical strain in the prism, modulating its birefringence. The acoustic vibrations generate a standing longitudinal sound wave in the optical head [114]. The optical head of the PEM has such dimensions that a node occurs at the junction of prism and transducer and an anti-node near the center of the prism; so the strain amplitude is small at the junction between the transducer and the optical prism but

large in the center of the optical aperture [115]. As mentioned before the PEM is a single axis modulator where single axis refers to the wave resonance condition. The standing sound wave will cause modulations of light linearly polarized perpendicular to the modulator's optical axis. The PEM-90 is mounted horizontally on a non-magnetic optical post that can be rotated by a computer controllable Melles Griot micro-encoder rotation stage. This allows us to change the angle between the laser beam and the optical axis of the modulator with a resolution of 0.21 mdegr. A PDA50 Thorlabs photodetector that includes a pre-amplifier is used to convert the light into an electric signal which is monitored by a 5 GHz/s-50 MHz Tektronix scope (TBS 1052B EDU). The PDA50 was used at its lowest trans-impedance range which results in a bandwidth of 10 MHz. The DC and AC components of the detector signal are measured by an HP3457 multi-meter and two SR830 lock-in amplifiers. An electromagnet powered by a 100 watt Kepco power supply and furnished with a Hall probe is used to apply a magnetic field to the sample (+/-2000 Oersted). Measurements can be made in reflection or transmission mode. The sample-holder is made out of aluminum and brass and the sample is secured by copper-blade springs mounted with brass screws. An XY-Melles Griot Micro-encoder system is used to move the sample in between the pole pieces of the magnet when using the setup in scanning Kerr microscopy mode. By inserting a Mitutoyo long distance objective between the modulator and the sample, a resolution of less than 8 μm is easily obtained in scanning mode [110].

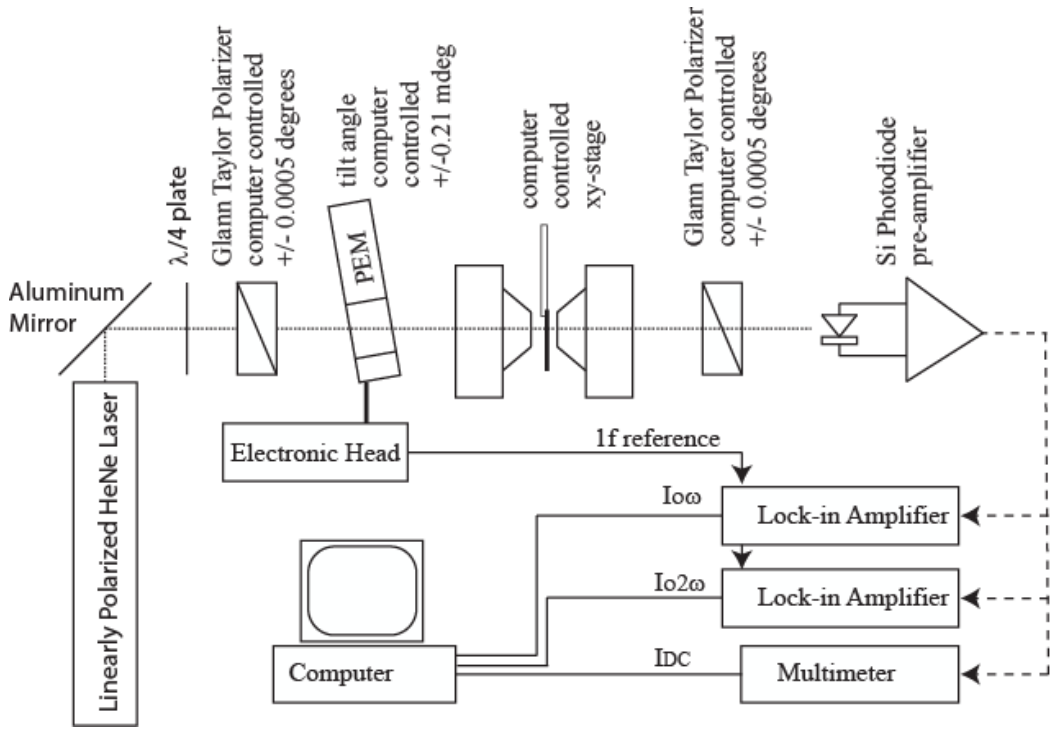

Fig. 6.6: Magneto-Optical Kerr setup.

6.3.1 Step Response of PEM

Similar to wave plates, PEMs are known to be very sensitive to temperature. A slight change in the lab temperature will result in small thickness change of its optical prism. The latter has an effect on its retardation but also on the Fabry-Perot interference effect described later in this chapter. Commercial PEMS are sometimes placed in a small furnace whose temperature is kept constant with a PID controller. For example, the PEM-ATC of Hinds Instruments. Temperature variations of the PEM can result from two sources: (1) change of the lab temperature; (2) change of the PEMs temperature by self-heating after a change of the retardation setting of the modulator. To study the latter effect the step response of the Hinds PEM-90 was measured. Fig 6.7, 6.8, and 6.9 shows the PEM's step response for sudden change of its retardation. Its frequency and the detector signal were monitored after changing the retardation setting with the

computer. Measurements were done for two different PEM tilt angles. The frequency of the modulator appears to increase/decrease while stepping up/down. According to Hirshy et al., the resonance frequency of the PEM increases with the temperature at a rate of 1.85 Hz per degrees. The observed step of 9 degrees indicates a temperature change of 4.9 degrees when changing the PEM's retardation with 4.6 radians. The increase of the resonance frequency with higher retardation settings is caused by a slight rise of the temperature of the optical head of the modulator caused by self-heating of the modulator. The step-up time constant was approximately 4 minutes while the step-down time constant was approximately 5 minutes. The dc and ac detector signals show each at least two time constants; one directly related to the sudden change of the modulation voltage and one related to the modulator's gradual temperature change. At 6 degrees PEM tilt angle (Fig. 6.7 and 6.8) Fabry-Perot interference of the coherent laser beam in the modulator is believed to be negligible. Note that the step-up graph for the 2ω signal shows an overshoot suggesting that the retardation step and temperature change have different sign influence on the 2ω signal. The 2ω step down response has an oscillating character, while the dc and 1ω step down graphs show no measurable overshoot. The step-up response at zero PEM tilt angle are shown in Fig. 6.9. The observed changes are much larger at perpendicular incidence. Differences are believed to originate from contributions caused by Fabry-Perot interference in the PEM's optical head.

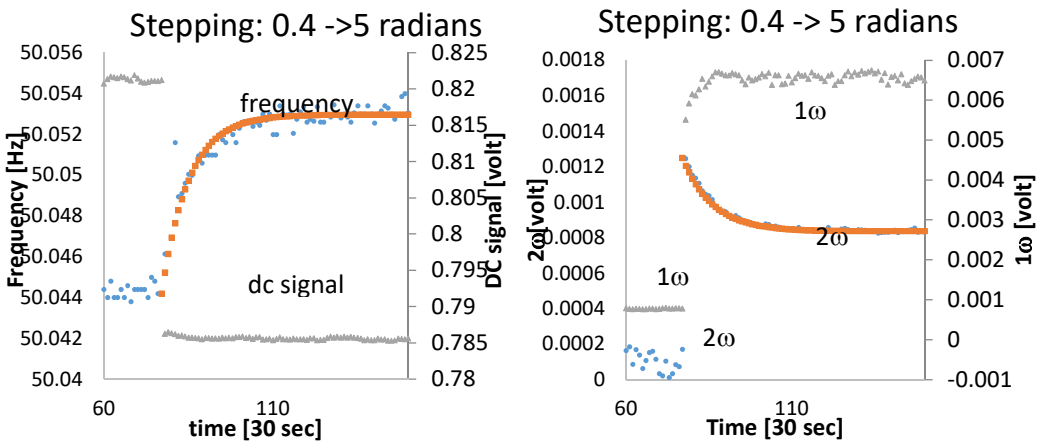

Fig. 6.7: Step-up response of PEM at 6˚ tilting angle.

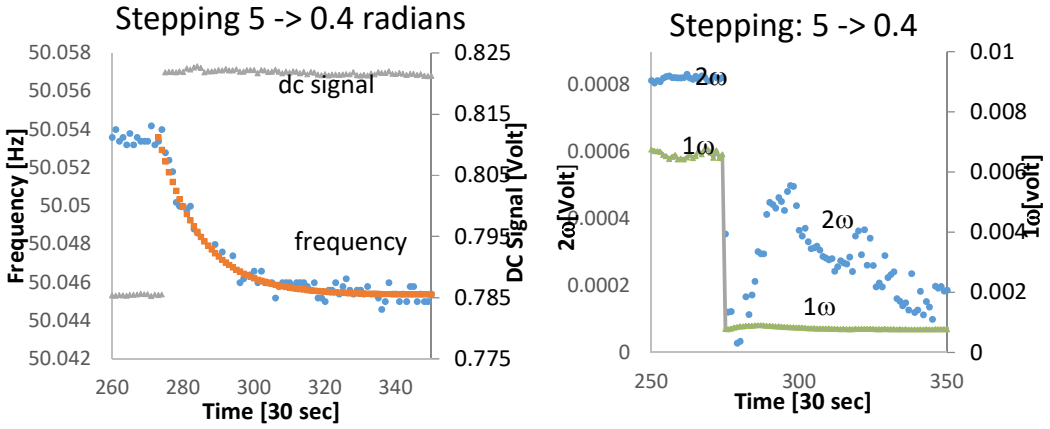

Fig. 6.8: Step-down response of PEM at 6˚tilting angle.

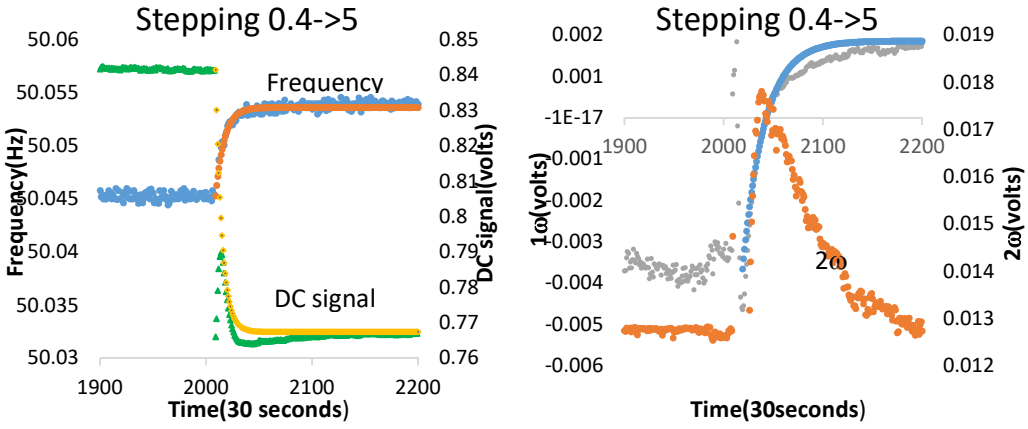

Fig. 6.9: Step-up response of PEM at perpendicular incidence.

6.4 Model

6.4.1 Without Analyzer

When using a PEM with highly coherent laser light, the electric field of light multiple times reflected in the modulator will also contribute to the transmitted light (see Fig. 2a). Assuming that all beams keep their phase relation the following expression for the electric field transmission coefficient of the PEM can be found [116]:

$$T = \frac{E_t}{E_i} = \frac{1}{E_i}\sum_{k=0}^{\infty} E_i t_{ag} t_{ga} r_{ga}^{2k} e^{i(2k+1)\frac{2\pi nd(t)}{\lambda}}$$
$$= t_{ga} t_{ag} \frac{e^{i\frac{2\pi nd(t)}{\lambda}}}{1 - r_{ga}^2 e^{2i\frac{2\pi nd(t)}{\lambda}}} \qquad [6.2]$$

Where t_{ag} (t_{ga}) is the amplitude transmission coefficient for the air-glass (glass-air) interface, r_{ga} is the amplitude reflection coefficients for the glass-air interface, λ is the laser wavelength in vacuum, t is the time, and $nd(t)$ the optical path length upon one pass of the laser beam through the PEM's optical head. Note that the numerator of equation [6.2] gives the pure phase shift while the denominator describes the PEM's intensity modulation. Since both the refraction index and the thickness of the optical head are modulated, $nd(t)$, the optical path length in meters for one pass of the laser beam through the optical head, is described by the product of two periodic functions:

$$nd(t) = (n_o + \Delta n \sin(\omega t))(d_o + \Delta d \sin(\omega t))$$
$$= n_o d_o + \frac{1}{2}\Delta n \Delta d + (n_o \Delta d + d_o \Delta n)\sin(\omega t) - \frac{1}{2}\Delta n \Delta d \cos(2\omega t) \qquad [6.3]$$
$$\approx n_o d_o + (n_o \Delta d + d_o \Delta n)\sin(\omega t) = \frac{\lambda}{4\pi}(a + b\sin(\omega t))$$

Where 'a' is twice the PEM's unstrained optical path length in radians, i.e. $a = \frac{4\pi}{\lambda} n_o d_o$, 'b' is twice the modulation of the PEM's optical path length in radians, i.e. $b = \frac{4\pi}{\lambda}\left(n_o \Delta d + d_o \Delta n\right)$, n_o is the refractive index (without strain) of the fused silica optical head (1.4569 at 632.8 nm), $\omega = 2\pi f$ is the modulation frequency of the PEM (f=50 kHz), d_o is the thickness of the optical head (6.35 +/-0.1 mm), Δn the amplitude of the refraction index variations induced by the periodic strain in the optical aperture, and Δd the modulation of the thickness of the optical head. For the single axis modulator used in this study, i.e. the PEM90, at normal retardation values we can ignore the 2nd DC term and the 2ω term in equation [6.3]. Note that Δd is the same for light linearly polarized along (p) or perpendicular (s) to the modulation axis. For a single axis modulator, Δn is different for the s-direction and p-directions. From crystal optics we know:

$$\begin{aligned} \Delta n_p &= -\frac{n_0^3}{2}\left[p_{11} - 2\nu p_{12}\right]\varepsilon_p \\ \Delta n_s &= -\frac{n_0^3}{2}\left[p_{12} - \nu\left(p_{11} + p_{12}\right)\right]\varepsilon_p \end{aligned} \qquad [6.4]$$

Where ν is Poisson's ratio, ε_p is the strain parallel to the modulation direction and p_{11} and p_{12} are Pockel's constants. For fused silica p_{11}=0.126 and p_{12}=0.26 at 632.8 nm [112][117] and the $\Delta n_s >> \Delta n_p$.

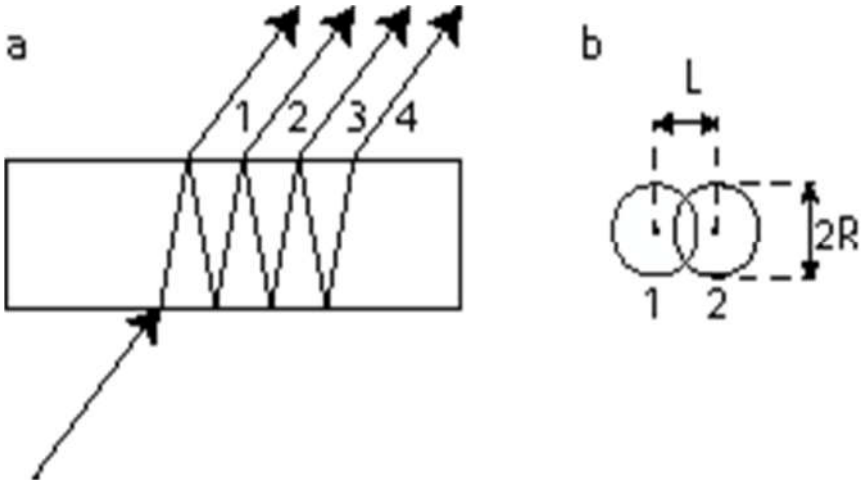

Fig. 6.10: (a) multiple interference in PEM optical head; (b) overlap of beam 1 and 2.

The birefringence can be calculated from [6.4] and is given by:

$$\Delta n = \frac{n_o^3}{2}\left[p_{12} - p_{11}\right]\left[1+\nu\right]\varepsilon_p \qquad [6.5]$$

For linearly polarized light polarized at an angle of Φ_p degrees with respect to the *p*-direction, the electric field at the detector can be described by Jones matrices, i.e.

$$\begin{pmatrix} E_p \\ E_s \end{pmatrix} = \begin{pmatrix} T_p & 0 \\ 0 & T_s \end{pmatrix}\begin{pmatrix} \cos(\Phi_p)E_o \\ \sin(\Phi_p)E_o \end{pmatrix} = E_o\begin{pmatrix} \cos(\Phi_p)T_p \\ \sin(\Phi_p)T_s \end{pmatrix} \qquad [6.6]$$

The intensity without analyzer is proportional to the square of the electric field, i.e.

$$I \propto \left|E_{\text{det}}\right|^2 = E_o^2 T_p T_p^* \cos^2(\Phi_p) + E_o^2 T_s T_s^* \sin^2(\Phi_p) \qquad [6.7]$$

Where the star indicates the complex conjugated. Using equation [6.2] we find the following expression for *TT**:

$$TT^* = t_{ga}t_{ag}t_{ga}^*t_{ag}^* \frac{1}{\left(1-r^2e^{i\frac{4\pi}{\lambda}nd(t)}\right)\left(1-r^2e^{-i\frac{4\pi}{\lambda}nd(t)}\right)}$$
$$= \frac{t_{ga}t_{ag}t_{ga}^*t_{ag}^*}{1+r^4} \frac{1}{\left(1-\frac{2r^2}{1+r^4}\cos\left(\frac{4\pi}{\lambda}nd(t)\right)\right)} \quad [6.8]$$

Notice that, $\frac{2r^2}{1+r^4} << 1$ so this can be approximated by:

$$TT^* \approx \frac{t_{ga}t_{ag}t_{ga}^*t_{ag}^*}{1+r^4}\left(1+\frac{2r^2}{1+r^4}\cos\left(\frac{4\pi}{\lambda}nd(t)\right)\right) = e\left(c+\cos\left(\frac{4\pi}{\lambda}nd(t)\right)\right) \quad [6.9]$$

Where '*e*', and '*c*' are defined as:

$$e = \frac{2t_{ga}t_{ag}t_{ga}^*t_{ag}^*r^2}{\left(1+r^4\right)^2}$$
$$c = \frac{1+r^4}{2r^2} \quad [6.10]$$

Substituting nd(t) from equation [3] in equation [9] gives:

$$TT^* \approx e\left(c+\cos\left(a+b\sin(\omega t)\right)\right)$$
$$= e\left(c+\cos(a)\cos\left(b\sin(\omega t)\right)-\sin(a)\sin\left(b\sin(\omega t)\right)\right) \quad [6.11]$$

Which can be simplified by expanding the cos(sin) and sin(sin) terms into Bessel Fourier series:

$$TT^* = e\left[c+\cos(a)\left[J_o(b)+2\sum_{k=1}^{\infty}J_{2k}(b)\cos(2k\omega t)\right]+ 2\sin(a)\sum_{k=1}^{\infty}J_{2k+1}\sin\{(2k+1)\omega t\}\right] \quad [6.12]$$

Strictly speaking equation [6.12] is only valid for perpendicular incidence as equation [6.3] only provides the optical path length at perpendicular incidence. For non-zero PEM tilt angle (ϕ) the path length of the laser beam through the optical head increases and becomes inversely proportional to the cosine of the angle of refraction

of the laser beam in the PEM's optical head. Correcting for the additional optical path length outside the modulator for a tilted PEM, and using Snell's law and a small angle approximation we find for the effective 'a' value:

$$\begin{aligned} a_{eff} &= \frac{4\pi}{\lambda} n_o d_o \cos(\phi_r) = a\cos(\phi_r) \\ &\approx a\cos\left(\frac{\phi}{n_o}\right) \approx a - \frac{1}{2}\frac{\phi^2}{n_o^2} a \end{aligned} \qquad [6.13]$$

A similar correction can be made for 'b', i.e.

$$\begin{aligned} b_{eff} &= \frac{4\pi}{\lambda} (n_o \Delta d + d_o \Delta n)\cos(\phi_r) \\ &= b\cos(\phi_r) \approx b\cos\left(\frac{\phi}{n_o}\right) \approx b - \frac{1}{2}\frac{\phi^2}{n_o^2} b \end{aligned} \qquad [6.14]$$

This approximation ignores the effect of the tilt angle on the birefringence [118]. For PEM tilt angles smaller than 2.5 degrees, (b_{eff}-b)<0.001, and the PEM tilt angle dependence of b_{eff} can be ignored. Substituting [6.13] into [6.12] gives:

$$\begin{aligned} TT^* \approx e\Bigg\{ & c + \cos\left(a - \frac{1}{2}\frac{\phi^2}{n_o^2} a\right)\left[J_o(b) + 2\sum_{k=1}^{\infty} J_{2k}(b)\cos(2k\omega t)\right] \\ & + 2\sin\left(a - \frac{1}{2}\frac{\phi^2}{n_o^2} a\right)\sum_{k=1}^{\infty} J_{2k+1}(b)\sin((2k+1)\omega t)\Bigg\} \end{aligned} \qquad [6.15]$$

Using equation [6.15] we find for the tilt angle dependence of the intensity (up to the 2nd harmonic):

$$\begin{aligned} I_\phi = E_o^2 e\Bigg[& c + \cos\left(a - a\frac{\phi^2}{2n_o^2}\right)\left(J_o(b_p)\cos^2(\Phi_p) + J_o(b_s)\sin^2(\Phi_p)\right) + \\ & + 2\cos\left(a - a\frac{\phi^2}{2n_o^2}\right)\left(J_2(b_p)\cos^2(\Phi_p) + J_2(b_s)\sin^2(\Phi_p)\right)\cos(2\omega t) + \\ & 2\sin\left(a - a\frac{\phi^2}{2n_o^2}\right)\left(J_1(b_p)\cos^2(\Phi_p) + J_1(b_s)\sin^2(\Phi_p)\right)\sin(\omega t)\Bigg] \\ = I_{DC} + I_{o2\omega}\cos(2\omega t) + I_{o\omega}\sin(\omega t) \end{aligned} \qquad [6.16]$$

Where, $I_{DC} = E_o^2 e\left[c + \cos\left(a - a\frac{\phi^2}{2n_o^2} \right)\left(J_o(b_p)\cos^2(\Phi_p) + J_o(b_s)\sin^2(\Phi_p)\right)\right]$

$$I_{o\omega} = E_o^2 e\left[2\sin\left(a - a\frac{\phi^2}{2n_o^2} \right)\left(J_1(b_p)\cos^2(\Phi_p) + J_1(b_s)\sin^2(\Phi_p)\right)\right]$$

$$I_{2\omega} = E_o^2 e\left[2\cos\left(a - a\frac{\phi^2}{2n_o^2} \right)\left(J_2(b_p)\cos^2(\phi_p) + J_2(b_s)\sin^2(\phi_p)\right)\right]$$

This equation shows that the DC and 2ω term will have the same PEM tilt angle dependence and have extremes for the same PEM tilt angles. The 1ω term will be maximum for PEM tilt angles for which the 2ω component is zero and vice versa. This is in agreement with our observations reported previously [118].

6.4.2 With Analyzer

The effect of the analyzer can be determined by inserting its Jones matrix in equation [6.6]. Assuming the orientation of the analyzer with respect to the p-direction we find:

$$\begin{pmatrix} E_p \\ E_s \end{pmatrix} = \begin{pmatrix} \cos^2(\Phi_A) & \cos(\Phi_A)\sin(\Phi_A) \\ \cos(\Phi_A)\sin(\Phi_A) & \sin^2(\Phi_A) \end{pmatrix}\begin{pmatrix} T_p & 0 \\ 0 & T_s \end{pmatrix}\begin{pmatrix} \cos(\Phi_p)E_o \\ \sin(\Phi_p)E_o \end{pmatrix}$$
$$= E_o\begin{pmatrix} \cos^2(\Phi_A)\cos(\Phi_p)T_p + \cos(\Phi_A)\sin(\Phi_A)\sin(\Phi_p)T_s \\ \cos(\Phi_A)\sin(\Phi_A)\cos(\Phi_p)T_p + \sin^2(\Phi_A)\sin(\Phi_p)T_s \end{pmatrix} \quad [6.17]$$

Similar to [6.7] we find the intensity by multiplying the components with their complex conjugated and adding both terms:

$$I \propto \left|E_{\text{det}}\right|^2 = E_o^2 T_p T_p^* \cos^2(\Phi_p)\cos^2(\Phi_A) + E_o^2 T_s T_s^* \sin^2(\Phi_p)\sin^2(\Phi_A) + \left(T_p T_s^* + T_s T_p^*\right)\sin(\Phi_A)\cos(\Phi_A)\sin(\Phi_p)\cos(\Phi_p) \quad [6.18]$$

For MO Kerr measurements the analyzer is normally set to 0 degrees which simplifies the intensity to (up to the 2nd harmonic):

$$\begin{aligned} I_\phi &= E_o^2 e\left[c + \cos\left(a - a\frac{\phi^2}{2n_o^2}\right) J_o(b_p)\cos^2(\Phi_p) + \right. \\ &+ 2\cos\left(a - a\frac{\phi^2}{2n_o^2}\right) J_2(b_p)\cos^2(\Phi_p)\cos(2\omega t) + \\ &\left. 2\sin\left(a - a\frac{\phi^2}{2n_o^2}\right) J_1(b_p)\cos^2(\Phi_p)\sin(\omega t)\right] \\ &= I'_{DC} + I'_{o2\omega}\cos(2\omega t) + I'_{o\omega}\sin(\omega t) \end{aligned} \quad [6.19]$$

Where, $I'_{DC} = E_o^2 e\left[c + \cos\left(a - a\frac{\phi^2}{2n_o^2}\right) J_o(b_p)\cos^2(\Phi_p)\right]$

$$I'_{o\omega} = E_o^2 e\left[2\sin\left(a - a\frac{\phi^2}{2n_o^2}\right) J_1(b_p)\cos^2(\Phi_p)\right]$$

$$I'_{o2\omega} = E_o^2 e\left[2\cos\left(a - a\frac{\phi^2}{2n_o^2}\right) J_2(b_p)\cos^2(\phi_p)\right]$$

This expression has a similar angle dependence as in the case of without analyzer. Note that a small misalignment of the analyzer or polarizer will result in additional terms similar to equation [6.16].

Note that I_{DC}, $I_{o\omega}$, $I_{o2\omega}$ and I'_{DC}, $I'_{o\omega}$ and $I'_{o2\omega}$ vary periodically with the PEM tilt angle ϕ although their amplitudes are independent of ϕ. Previous measurement results

however show a decrease of the interference effect with PEM tilt angle [118]. This happens due to less overlap of the primary beam with the beams that pass multiple times through the modulator (see Fig. 6.10). Only at perpendicular incidence when all beams completely overlap is the value calculated from expressions [6.16] and [6.19] correct. For non-zero angles of incidence the various beams are shifted with respect to the primary beam. We can estimate the effect on the intensity amplitudes from the fraction of the area of the primary beam that overlaps with the secondary beam (See Fig. 6.10b). For a beam radius *R* and a beam shift *L* this fraction is:

$$\frac{A_{seg}}{\pi R^2} = \frac{2}{\pi}\cos^{-1}\left(\frac{L}{2R}\right) - \frac{L}{2\pi R^2}\sqrt{4R^2 - L^2} \qquad [6.20]$$

Where, A_{seg} is the surface of the overlap of two consecutive beams, *R* is the laser beam radius and *L* is the separation (center to center) between the primary beam 1 and the beam 2 that passes two more times through the modulator head (walk-off). The latter can be calculated from Snell's law of refraction. Taking the small angle approximation we find, $L = \frac{2\phi_i d}{n_o}$. $\mathrm{L} = \frac{2\phi_{\mathrm{i}}\mathrm{d}}{\mathrm{n_0}}$ So the PEM tilt angle dependence of the I_{DC}, $I_{o\omega}$, and $I_{o2\omega}$ signals are described by:

$$\frac{I(\phi)}{I(0)} = \frac{2}{\pi}\left[\cos^{-1}\left(\frac{\phi d_o}{n_o R}\right) - \frac{\phi d_o}{n_o R^2}\sqrt{R^2 - \frac{\phi^2 d_0^2}{n_o^2}}\right] \qquad [6.21]$$

This equation is only valid for $\phi < Rn_o/d_o$ as there is no overlap beyond this angle. Note that we assumed that the electric field amplitude E_o is constant across the beam and that only the interference between the primary and secondary beam are

relevant. Equation [6.21] can be well approximated by a straight line for angles below 2.5 degrees. For larger angles a small 2nd order correction is required. This effect can be modelled by replacing the parameter 'e' in equations [6.16] and [6.19] by 'hϕ+j' or for better fits by 'gϕ^2+hϕ+j', where g, h, and j are fit parameters.

The model described in the previous section in particularly equation [6.16], is compared with previous experimental results [6.27] in Fig.6.11. For the setup without analyzer and sample the $I_{o\omega}$ and $I_{o2\omega}$ were measured with the lock-in amplifiers. The I_{DC} was measured with the HP digital voltmeter. See Fig.6.6 for more details on the measurement setup. Measurement points are indicated by markers. The 1ω signal is shifted in the y-direction with 0.05 volt for clarity. All three signals have an extreme at perpendicular incidence and are periodic with the PEM tilt angle. The 1ω, and 2ω signals appear to be shifted with respect to each other at larger PEM tilt angles: when the 1ω signal is maximum the 2ω component is zero and vice versa. An exception is perpendicular incidence where the 2ω signal has a minimum but does not become zero. The DC and 2ω signal have extremes at the same PEM tilt angles. Although an intensity stabilized laser was used, small drifts were still observed in the DC signal. Observed DC drifts are consistent with the specifications of the laser. The lines in Fig. 6.11. are the result of a model fit using equation [6.16] assuming the parameter '*e*' is a linear function of ϕ. The least square fit was done using the solver add-in of Microsoft Excel.

Note that the periodicity of the PEM tilt angle dependence of the 1ω, 2ω and DC

components are all the same (see phase of cosine and sine functions in equation [6.16]), but the period decreases with angle ϕ because of the ϕ^2 term.

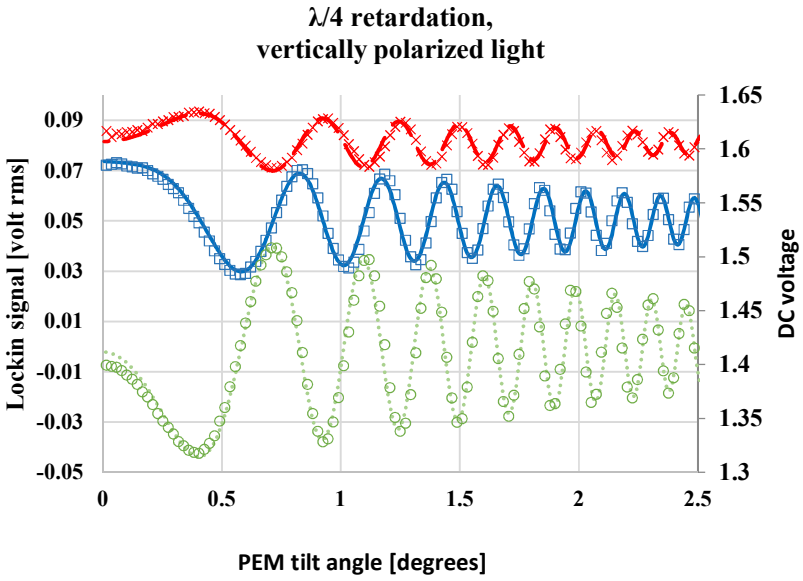

Fig. 6.11: I_{DC} (top red), $I_{o\omega}$ (middle blue) and $I_{o2\omega}$ (bottom green) as a function of PEM tilt angle for vertically polarized light: Measurement data (markers) and model fit (line). The $I_{o\omega}$ curve is shifted 0.05 volts up for clarification.

For two consecutive zeros on the PEM tilt angle curve the optical path length difference for the beam passing through the modulator two more times increases with 2π or in other words:

$$a - \frac{a\phi_1^2}{2n_o^2} = 2m\pi \quad \text{and} \quad a - \frac{a\phi_1^2}{2n_o^2} = 2(m-1)\pi \qquad a\text{-}\frac{a\phi^2}{2n_0^2} = 2(m\text{-}1)\pi \quad [6.22]$$

Subtracting one from another we get: $\phi_2^2 - \phi_1^2 = \frac{4\pi n_o^2}{a}$ $\phi_2^2 - \phi_1^2 = \frac{4\pi n_0^2}{a}$

Replacing, $\phi_2 = \phi_1 + \Delta\phi$ and ignoring $(\Delta\phi)^2$ we find:

$$\Delta\phi = \frac{2\pi n_o^2}{a\phi_1} \quad \Delta\phi = \frac{2\pi n_0^2}{a\phi_1} \qquad [6.23]$$

Or in other words the PEM tilt angle period, $\Delta\phi$, is inversely proportional to the PEM tilt angle and thus decreases for larger angles. Fig. 6.12. below shows the period

determined from the measurement data (blue markers) presented in Fig. 6.11. and a model fit performed in Microsoft Excel using equation [6.23]. Best fit is obtained for $\frac{2\pi m_o^2}{a} = 6.5E-5$ which is close to what we expect using the specs provided by Hinds Instruments (7.3E-5) and suggests that our modulator is slightly thicker than ¼". The calculated modulator thickness using the results of the fit is d_o=0.0712 m. Note that at perpendicular incidence the magnitude of the 1ω and 2ω components depend on the parameter '*a*' and thus on 'd_o', a parameter that likely varies among PEMs with different thicknesses.

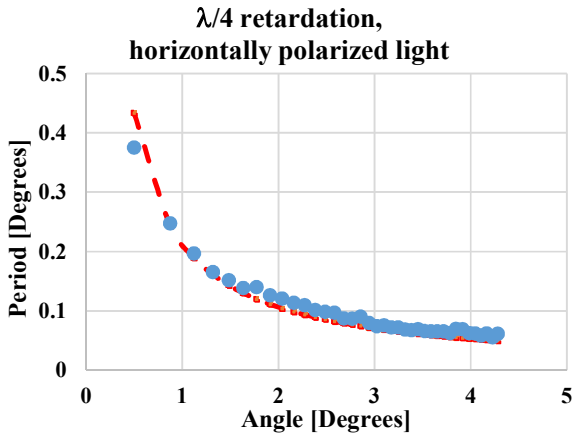

Fig. 6.12: Period of 2ω signal as a function of the PEM tilt angle determined from the data of Fig. 3 and best fit using equation [6.23].

Fig. 13. shows the time dependence of the intensity at perpendicular incidence with the analyzer and sample removed (retardation is set to 0.25λ). The colored markers are the measurement data and the solid lines are model fits of equation [16] done in Microsoft Excel. With no polarizing optics between the PEM and the detector the observed intensity variations are solely due to the interference of the coherent laser light in the PEM caused by the modulation of the optical path length of the laser beam in the optical head. Note that the modulation depth for vertical linearly polarized light

is larger than for horizontal linearly polarized light. This is in agreement with literature and equations [6.4] and [6.6] shown above.

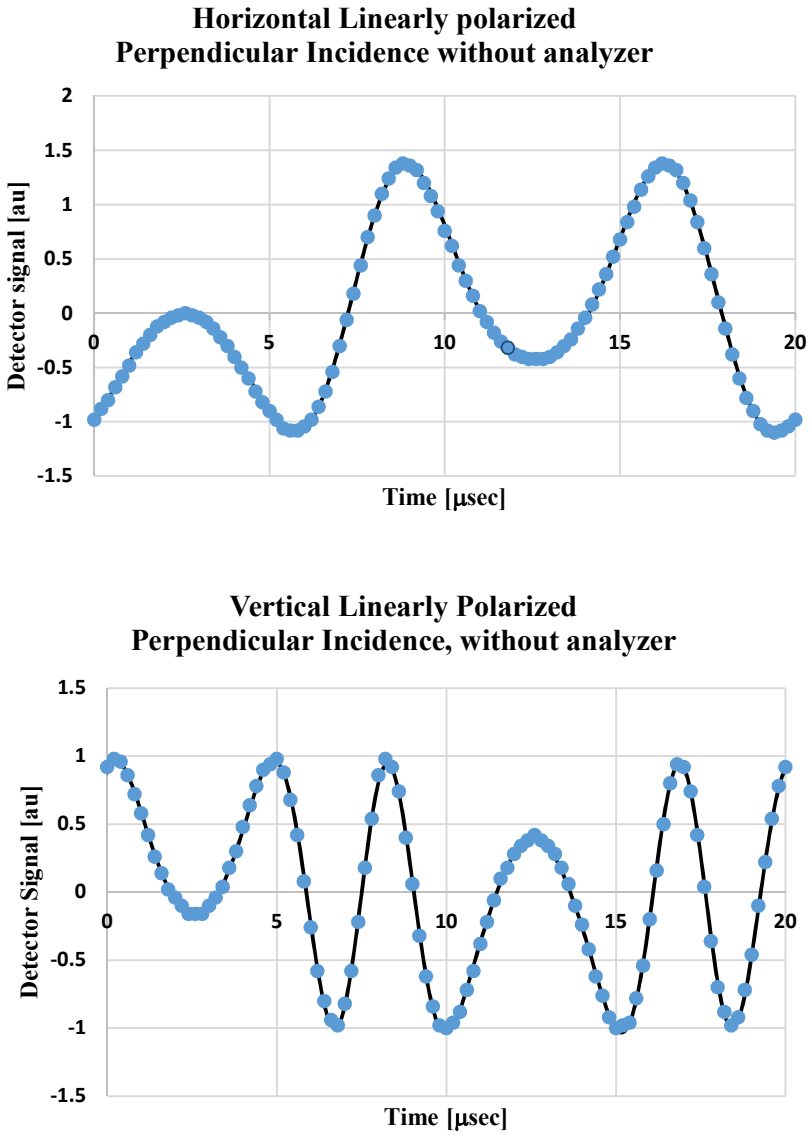

Fig. 6.13: Intensity as a function of time at 0.25λ retardation depth for vertical linearly and horizontal linearly polarized light on PEM: measured values (blue circles) and model fit (solid line).

The fit parameters are summarized in Table 1. The relative values of the higher harmonics determined from the measurement data of p-polarized light (i.e. $I_{o\omega}/I_{o3\omega}$, $I_{o\omega}/I_{o5\omega}$, and $I_{o2\omega}/I_{o4\omega}$) were used to estimate b_p=3.28. The b_s was estimated from the

$I_{o\omega}/I_{o3\omega}$, $I_{o\omega}/I_{o5\omega}$, and $I_{o2\omega}/I_{o7\omega}$ ratios for s-polarized light (b_s=6.56). As expected the difference of b_p and b_s (3.22) is approximately twice the retardation in radians (2*π/2), i.e.

$$b_p - b_s = \frac{4\pi}{\lambda}\left(d_o\Delta n_p + \Delta d n_o\right) - \frac{4\pi}{\lambda}\left(d_o\Delta n_s + \Delta d n_o\right) = \frac{4\pi}{\lambda}\left(d_o\Delta n\right) \qquad [24]$$

Table 6.1: Result of Intensity vs Time fit

SOP	Phase [μsec]	Error [/datapnt]	Freq [Hz]	$I_{o\omega}$	$I_{o2\omega}$	$I_{o3\omega}$	$I_{o4\omega}$	$I_{o5\omega}$	$I_{o6\omega}$	$I_{o7\omega}$	$I_{o8\omega}$
S	-12.4	4.0E-4	50062	-0.27	-0.09	-0.11	0.09	0.72	0.11	0.36	0.04
P	-12.4	3.3E-4	50063	0.5	0.32	0.86	0.1	0.17			

Fig. 6.14. shows the $I_{o\omega}/I_{DC}$ and $I_{o2\omega}/I_{DC}$ detector signals as a function of the polarizer angle for perpendicular incidence with both the sample and the analyzer removed. Both signals are periodic as a function of the polarizer angle. Note that the 1ω and 2ω signals are zero at around 50 and 51 degrees respectively. This is off from the 45 degrees observed by Polnau et al. for a double axis PEM [104]. Further investigations revealed that not for all retardation setting the 1ω and 2ω signals have a zero for a specific polarizer angle. No zeros were found for a retardation of 0.5λ while for 0.79λ only the 2ω component has a zero. The ability to zero both the 1ω and the 2ω signal for certain values of the retardation (read b) can be understood from equation [6.16]. If $J_1(b_p)$ and $J_1(b_s)$ have opposite sign the $I_{o\omega}$ component can be zeroed with the polarizer. If $J_2(b_p)$ and $J_2(b_s)$ have opposite sign the $I_{o2\omega}$ component can be zeroed with the polarizer. It is clear from Fig. 6 that the graph is not symmetric around zero

degrees. This is due to a slight misalignment of the polarizer in the rotation stage (normal of the polarizer prism and rotation axis are not parallel). Also the light incident on the polarizer was slightly elliptically polarized (I_v/I_h=0.8). So, in case one wants to determine the effect of Φ_p on the intensity with more accuracy, it is better to use a fixed polarizer and to rotate the PEM around the optical axis of the setup as done by Polnau et al. [104].

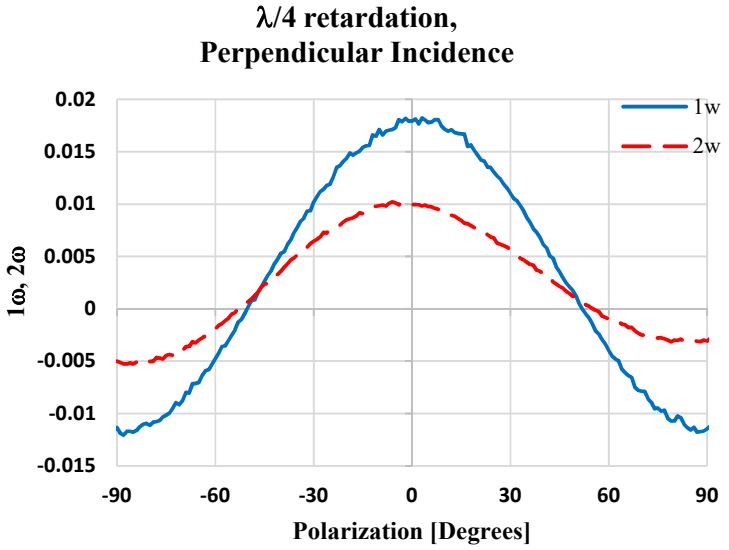

Fig. 6.14 : Normalized 1ω and 2ω components of the detector signal as a function of the polarizer angle.

The consequences for the MO Kerr measurement technique becomes clear from a typical Kerr setup. For MO Kerr measurements one uses a polarizer set at 45 degrees. No analyzer is required to measure the Kerr ellipticity and the detector intensity contains a 1ω signal that is proportional to the Kerr ellipticity [89]

$$I \propto 1 + 4\varepsilon_k J_1(\delta_o)\sin(2\Phi_p)\sin(\omega t) \qquad [6.25]$$

Where ε_k is the Kerr ellipticity, δ_o is the total retardation depth equal to $\delta_o = \frac{2\pi}{\lambda}\left(d_o \Delta n_p + d_o \Delta n_s\right)$, and J_1 is the first order Bessel function. The proportionality constants for the Kerr ellipticity is maximum at a δ_o of 1.84 radians.

For setups that are used to measure the Kerr rotation and Kerr ellipticity simultaneously, one inserts an analyzer in between the sample and the detector. With the analyzer set to 0 degrees, the 1ω component will become linearly proportional to the Kerr ellipticity and the 2ω component linearly proportional to the Kerr rotation, i.e.

$$\begin{aligned} I \propto\ & 1 + J_0\left(\delta_0\right)\sin(2\Phi_p)\sin\left(2\Phi_A + 2\theta_k\right) \\ & + \cos(2\Phi_p)\cos\left(2\Phi_A + 2\theta_k\right) \\ & + 4\varepsilon_k J_1\left(\delta_0\right)\sin(2\Phi_p)\sin\left(\omega t\right) \\ & + 2J_2\left(\delta_0\right)\sin(2\Phi_p)\sin\left(2\Phi_A + 2\theta_k\right)\cos\left(2\omega t\right) \end{aligned} \qquad [6.26]$$

Where J_o, J_1, and J_2 are the zero, 1st and 2nd order Bessel functions and the other parameters are as defined above. Note that the proportionality constants for the Kerr ellipticity and Kerr rotation are maximum at a δ_o of 1.84 and 3.05 radians respectively and that the DC component is also proportional to the Kerr rotation unless δ_o is equal to 2.4. Note that the AC-signals carrying the MO information have the same frequency and phase as the AC-signals due to the PEM interference effect, compare equations [6.25] and [6.26] with equations [6.16] and [6.18]. As the signals originating from the PEM interference effect are constant, one can simply subtract them out. The problem is that the signals of the PEM interference effect are typically several orders of magnitude larger than the MO-signals, meaning that drift of the setup which includes

drift of the laser intensity, drift of the laser beam direction, and drift of retardation, all induced by temperature fluctuations in the lab can result in drifts of the AC-offsets. To avoid these issues, it is best to null the AC-offsets. It is clear from equations [6.16] and [6.19] that one can always find an angle for which the $I_{o\omega}$ $(I'_{o\omega})$ or $I_{o2\omega}$ $(I'_{o2\omega})$ component is zero by adjusting the PEM tilt angle. For the setup without analyzer the retardation values for which $J_2(b_s)$ has an opposite sign from $J_2(b_p)$ or $J_1(b_s)$ has opposite sign of $J_1(b_p)$, one can zero both the $I_{o\omega}$ and $I_{o2\omega}$ components by adjusting first the PEM tilt angle and then the polarizer angle. Note that since $J_2(x)$ is an even function, for a single axis PEM the 2ω signal is in general unequal to zero at a polarizer angle of 45 degrees. This approach to null the offsets will no longer work well if $J_n(b_p)/J_n(b_s)$ is larger than 10 or smaller than 0.1 as then the polarizer angle will be too close to zero or 90 degrees making the setup insensitive to the MO effects. For the measurement setup that includes an analyzer at zero degrees (regular MO Kerr setup) one can no longer use the polarizer angle to zero $I'_{o\omega}$ or $I'_{o2\omega}$ as can be concluded from equation [6.19]. It is still possible to zero both AC-signals but one should use the PEM tilt angle and the retardation depth. The measured zeros for $I'_{o\omega}$ and $I'_{o2\omega}$ are summarized in table 6.2 for both *p* and *s*-polarized light. The results are compared with the values calculated from the b_p and b_s determined above. Although the general tendency of equation [6.19] is reproduced, we noticed larger discrepancies between calculated and measured zeros for *s*-polarized light suggesting that the b_s determined from the higher harmonics of the intensity-time plots is not that accurate. Another reason for the observed differences could be the ignored angle dependence of the birefringence or the PEM tilt

angle dependence of '*b*'. As δ_o is the difference from b_p to b_s, the zeros listed in table 6.2 do not coincide with zeros for the MO-signal's sensitivity.

Table 6.2: Measured and Calculated Retardation values that shows zeros for the AC-offsets originating from the PEM interference effect. The calculated values are the zero determined from the b_p and b_s values estimated from the intensity-time graphs.

p-polarized				**s-**polarized			
($I'_{o\omega}$)		($I'_{o2\omega}$)		($I'_{o\omega}$)		($I'_{o2\omega}$)	
Meas.	Calc.	Meas.	Calc.	Meas.	Calc.	Meas.	Calc.
1.8	1.8	2.7	2.4	1.69	1.1	1.22	1.4
3.4	3.2	3.8	3.9	2.47	2	2.05	2.3
4.9	4.7			3.24	2.9	2.78	3.3
				4.06	3.7	3.64	4.1
				4.78	4.7	4.31	5

6.5 Experimental Data of $Ni_{81}Fe_{19}O$ Samples with Different Oxygen Flow

The optimized setup was used to determine the MO Faraday rotation of FeNiO samples sputtered on fused quartz and microscope slides substrates. The samples were sputtered at room temperature with different oxygen flow rate. The oxygen percentage in the sputter gas was calculated from the gas flow rates ϕ_{Ar} and ϕ_{O2} using:

$$O_2\text{-percentage}=(100\ \phi_{O2})/(\ \phi_{Ar}+\ \phi_{O2})$$

The total flow rate, i.e. $\phi_{Ar} + \phi_{O2}$ was kept at 50 sccm for all samples. Here the slope of the $I_{2\omega}/I_{dc}$ versus H graph was determined from the measurement data for the low pressure $Ni_{0.81}Fe_{0.19}O_{(1-\delta)}$ oxygen flow series. The results are summarized in Fig. 6.15 below. Included is data of the fused quartz substrate and also the data measured on a 10% Fe sample, i.e $Ni_{0.9}Fe_{0.1}O_{(1-\delta)}$. The Faraday rotation thin film appears to have a non-zero Faraday effect that is significantly different from that of the substrate. The data was used to calculate the Verdet constant by subtracting the signal of the

substrate and dividing by the film thickness. The calculated Verdet constant for $Ni_{0.81}Fe_{0.19}O_{(1-\delta)}$ is shown in Fig. 6.14. Errors in the data of Fig. 6.14 are mainly originating from the estimation of substrate and film thickness. The same substrate signal was subtracted from all data.

To reduce the error measurements were also performed on the high-pressure thick film series. For these measurements for each sample and the substrate and the film+substrate were measured. So, the real substrate signal was subtracted. The results are summarized in Table 6.3 below. The Verdet constant increases with the inclusion of Fe and the inclusion of oxygen vacancies. Increase for samples sputtered at lower oxygen flow rate confirm the VSM results of Twagirayezu [119].

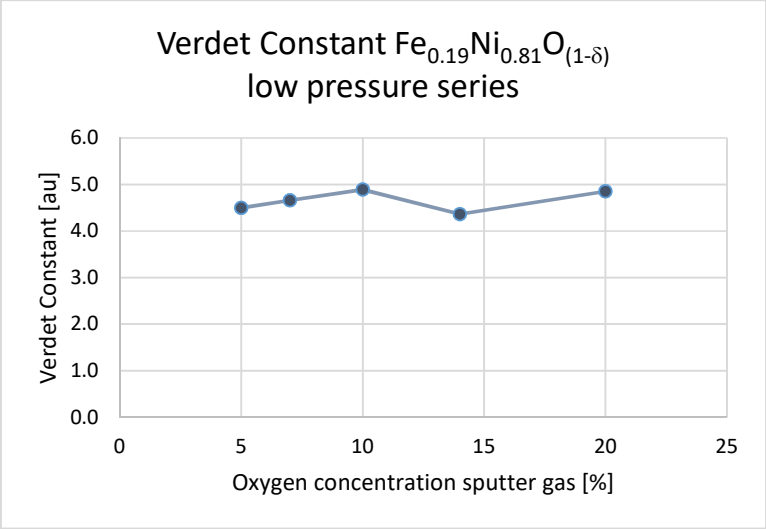

Fig. 6.15: Influence of Oxygen flow on the Verdet Constant of the $Ni_{81}Fe_{19}O$ thin films.

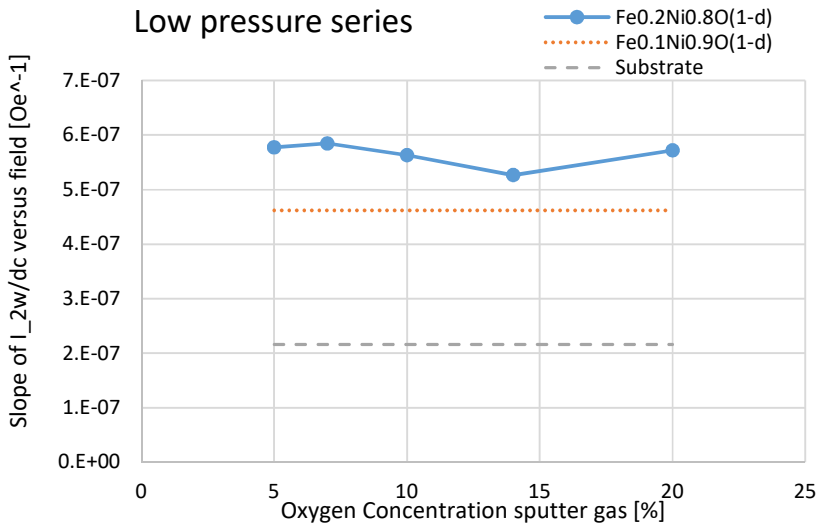

Fig. 6.16: Slope of $I_{2\omega}/I_{dc}$ vs H curve as a function of Oxygen flow during deposition of low pressure $Ni_{(1-x)}Fe_xO$.

Table 6.3: Verdet constant of thick films of NiO and $Ni_{81}Fe_{19}O$ with high and low oxygen flow:

Sample Name (O_2 flow %)	Verdet Constant [Degrees/(Oe m)]		average Verdet constant [degrees/(Oe m)]
	QCM Thickness	Ellipsometry Thickness	
NiO(1%)	9.20	65.1	37
NiO(10%)	3.52	2.49	3
$Ni_{81}Fe_{19}O$(1%)	123	87.5	105
$Ni_{81}Fe_{19}O$(10%)	70.9	1.30	36

6.6 Conclusion

The PEM's frequency and detector signals were monitored as a function of the time after step change of the PEM's retardation setting. The step response graphs show two time constants: one short time constant originating from the electronic head, and one longer time constant of 4 to 5 minutes originating from effects of self-heating of the modulator. The temperature change of the modulator caused by self-heating after a retardation step of 4.5 radians was estimated to be approximately 5 degrees.

The Jones matrix for coherent light was derived for a single axis PEM. Although

others have used Jones Matrices to describe the Fabri-Perot interference in static wave plates [120][121], this is the first Jones matrix description of the effect in a PEM. The matrix describes both the intensity modulation caused by the PEM interference effect and the phase modulation at perpendicular incidence. The Jones matrix was used to determine the detector signal for a setup involving a polarizer and shows that the detector signal has large 1ω and 2ω offset signals caused by Fabry-Perot interference in the PEM's optical head. The derived model shows how the offset signals depend on PEM tilt angle, polarizer angle and retardation depth. The offsets can be minimized at small PEM tilt angles by adjusting the PEM tilt angle although not simultaneously for the 1ω and 2ω components. For some retardation depths, it is possible to zero both the offset in the 1ω and 2ω detector signal for the analyzer-less setup, but not for all retardation depths. For the setup that includes an analyzer set at 0 degrees, it is no longer possible to use the polarizer angle to zero one of the components. For such setup, one can still zero both offsets by adjusting first the retardation nulling the $J_1(b_p)$ or $J_2(b_p)$ term and then adjusting the PEM tilt angle to zero the other term. Zeroing the offset originating from the PEM interference will allow one to avoid the large offsets in the 1ω and 2ω signals and use a much lower lock-in amplifier range that is more sensitive and has less noise. A low offset in ac-signals is also desirable to reduce signal drifts originating from temperature fluctuations of modulator, laser, or lab. A zero offset will further allow one to improve the S/N ratio of the MOKE setup by dividing the AC-signals by the DC-signal and making the setup insensitive to laser intensity variations. This correction is

not meaningful when large AC-offsets are present.

The optimized setup was used to determine the Verdet constant of NiO and FeNiO thin films. The Verdet constant appears to increase with iron doping and with oxygen concentration. The results are in agreement with the results of Twagirayezu [109].

VII. COMPOSITION ANALYSIS

7.1 Rutherford Backscattering Spectroscopy (RBS)

As a method for materials analysis Rutherford Backscattering Spectroscopy (RBS) was first introduced by Rubin et. al. in 1957 [122]. In general, RBS measures the elastic scattering of an incident beam of high energy particles with a stationary solid sample. The scattering nucleus can be identified by the fractional momentum loss of the incident particle.

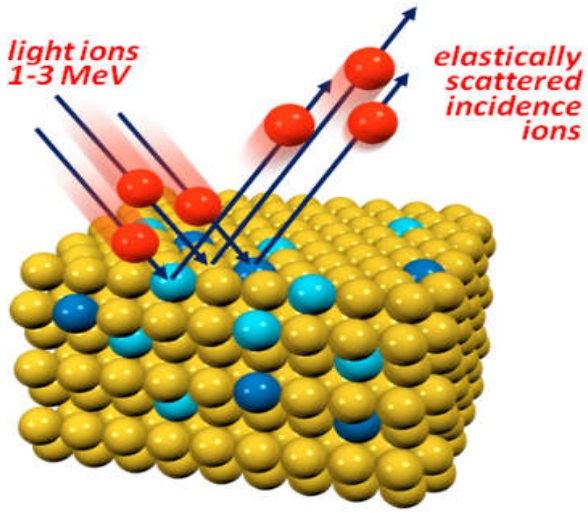

Fig. 7.1: Incident ions collides with the particles in the materials and backscattered (elastic collision).

A target is bombarded with ions at an energy in the MeV-range (typically 0.5–4 MeV), and the energy of the backscattered projectiles is recorded with an energy sensitive detector. From RBS, one can get the quantitative determination of the composition

of a material without reference sample. It is also possible to determine depth information from the measurement data and do depth profiling of individual elements through the thickness of the sample. Although RBS gives low sensitivity for light elements, for heavy elements a very good sensitivity of the order of parts-per-million (ppm) can be found. The analyzed depth is typically about 2 µm for incident He-ions and about 20 µm for incident protons. Usually protons, ^{4}He, and sometimes lithium ions are used as projectiles at backscattering angles of typically 150-170°. Different angles or different projectiles are used in special cases [123].

Two types of scattering geometries (see figure 7.2) are often used: 1) IBM geometry and 2) Cornell geometry. IBM geometry is the simpler one of those two aforementioned scattering geometries. For this measurement geometry incident beam, exit beam and surface normal of the sample lie in the same plane, with

$$\alpha + \beta + \theta = 180° \qquad [7.1]$$

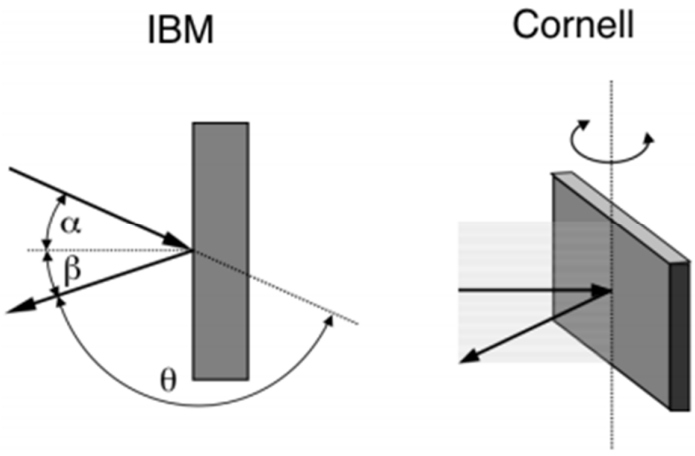

Fig. 7.2: Left: IBM geometry; Right: Cornell geometry. (Incident angle α, exit angle β and scattering angle θ.)

For Cornell geometry, incident beam, exit beam and the rotation axis of the sample are also in the same plane, but are related by

$$\cos(\beta) = -\cos(\alpha)\cos(\theta) \qquad [7.2]$$

Cornell geometry has the advantage of combining a large scattering angle, which is desirable for optimized mass resolution, and grazing incident and exit angles, which optimizes depth resolution.

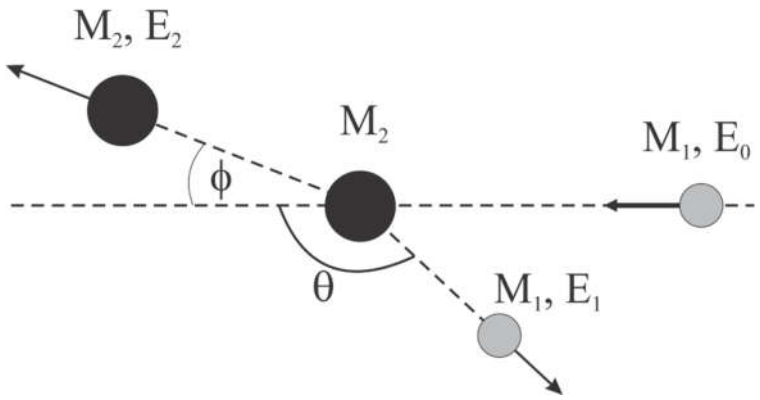

Fig. 7.3: Schematic representation of the collision process that takes place in the sample.

Fig. 7.3 shows a schematic representation of the elastic collision between the incident projectile of mass M_1 and energy E_0 and a target mass of mass M_2, which is initially at rest. After the collision, the projectile and target mass have energies of E_1 and E_2 and have been scattered to the laboratory angles θ and φ, respectively.

In a laboratory system, if the incident ion has incident energy, E_0 and mass, M_1 then after scattering the energy of the backscattered ion is given by,

$$E_1 = K\,E_0 \qquad [7.3]$$

Where the kinematic factor, K is given by the following equation,

$$K = \frac{{M_1}^2}{(M_1+M_2)^2}\left[\cos\theta \pm \left\{\left(\frac{M_2}{M_1}\right)^2 - \sin^2\theta\right\}^{1/2}\right]^2 \qquad [7.4]$$

Here, θ is the scattering angle and M_2, the mass of the target nucleus initially at rest. For $M_1 < M_2$ only the plus sign in eq. [7.4] applies. If $M_1 > M_2$ then eq. [7.4] has two

solutions, and the maximum possible scattering angle θ_{max} is given by,

$$\theta_{max} = \sin^{-1}\left(\frac{M_2}{M_1}\right) \quad [7.5]$$

With the scattering cross section,

$$\frac{d\sigma}{d\Omega} = \sigma(\theta) = \left(\frac{Z_1 Z_2 e^2}{4E \sin^2\left(\frac{\theta}{2}\right)}\right)^2 \quad [7.6]$$

Where, Ω is the solid angle of the detector (see figure 7.4). Z_1 and Z_2 are the atomic numbers of the incident and the target particles and e is the charge of the electron. If two different target elements with mass difference ΔM_2 are present, then the energy separation ΔE_1 of particles backscattered from the two masses is given by,

$$\Delta E_1 = E_0 \frac{dK}{dM_2} \Delta M_2 \quad [7.7]$$

Best energy separation and mass resolution are obtained for light target elements where the derivative dK/dM_2 is steep, while for heavy elements the mass resolution gets small. The mass resolution for heavier elements can be improved by using higher incident energies or heavier incident projectiles [124].

The determination of layer thickness from RBS data requires making assumptions about the film densities. The assumed densities used to calculate film thicknesses are included in the data tables. In general, the physical thickness of films should be checked with a direct measurement technique (SEM, TEM, AFM, profilometry). If the thickness of the films is known, the real density can be calculated. Conversely, if the density is known, RBS can provide accurate thicknesses. The equation governing the conversion from the RBS densities and thicknesses and real thicknesses to the real densities is:

$$D_{real} = (D_{RBS} \times T_{RBS})/T_{real} \quad [7.8]$$

7.1.1 Experimental Setup

The experimental setup for the backscattering experiment is shown in Figure 7.4. The measurements were done by Evans Analytical Group, a company specialized in materials characterization. A collimated beam of monoenergetic ions is incident on a planar sample. Particles backscattered to an angle θ are detected by a detector.

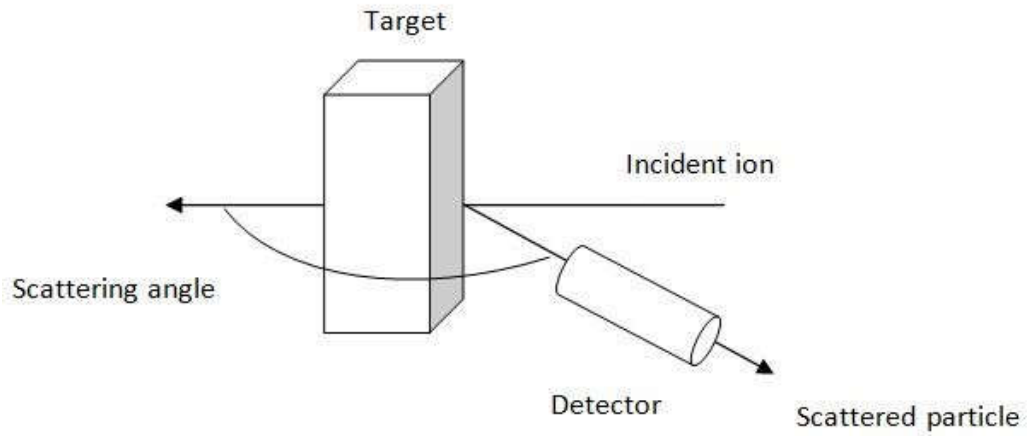

Fig. 7.4: Schematic view of RBS system.

RBS spectra are acquired at a backscattering angle of 160° and an appropriate grazing angle (with the sample oriented perpendicular to the incident ion beam). The sample is rotated or tilted with a small angle to present a random geometry to the incident beam. This avoids channeling in both the film and the substrate. The use of two detector angles can significantly improve the measurement accuracy for composition when thin surface layers need to be analyzed. The schematic diagram below shows the scattering geometry in a typical RBS experiment with two detectors.

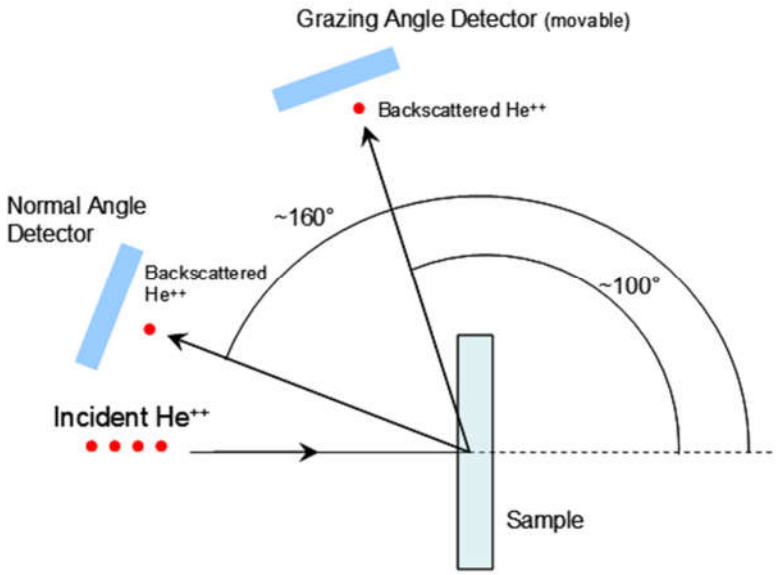

Fig. 7.5: Scattering geometry of the RBS system with two detectors.

When a thin (<100nm) amorphous or polycrystalline film resides on a single crystal substrate "ion channeling" may be utilized to reduce the backscattering signal from the substrate. This results in improved accuracy in the composition of layers containing elements that overlay with the substrate signal, typically light elements such as oxygen, nitrogen and carbon.

Analytical Parameters: RBS	
He^{++} Ion Beam Energy	2.275MeV
Normal Detector Angle	160°
Grazing Detector Angle	~100°
Analysis Mode	*CC RR*

7.1.2 Experimental Results

Two NiO thin films that were sputtered with low (1%) and high (10%) oxygen flow were analyzed by the RBS system to get a clear idea of the metal to oxygen ratio. Both samples were capped with a 10nm aluminum layer. Estimated thicknesses of the layers

were found by the QCM. To verify the layer thicknesses further measurements and fitting were done by the XRR.

Table 7.1: Atomic concentration in different layers of the low oxygen sample (NiO sputtered with 1% O_2 flow):

Layers	"RBS" Thickness [Å]	Atomic Concentrations [at%]				Assumed Density [at/cc]
		Si	Ni	O	Al	
Layer 1	110	-	-	30	70	6.35E22
Layer 2	760	-	53	47	-	8.19E22
Layer 3	60	33.3	-	66.7	-	6.41E22
BULK	-	100	-	-	-	5.00E22

Table 7.2: Atomic concentration in different layers of the high oxygen sample (NiO sputtered with 10% O_2 flow):

Layers	"RBS" Thickness [Å]	Atomic Concentrations [at%]				Assumed Density [at/cc]
		Si	Ni	O	Al	
Layer 1	115	-	-	30	70	6.35E22
Layer 2	750	-	43.3	56.7	-	7.99E22
Layer 3	50	33.3	-	66.7	-	6.41E22
BULK	-	100	-	-	-	5.00E22

Table 7.3: Estimated uncertainties and detection limits [in at%]

Element	Uncertainty (at%)
Ni	±1
O	±3

1) Uncertainties are expressed as expanded uncertainties U = kuc, where k is the coverage factor of 2 giving an approximate level of confidence of 95%, and uc is the combined standard uncertainty calculated in accordance with the ISO “Guide to the Expression of Uncertainty in Measurement”.

VIII. SUMMARY

In this research, the deposition process and properties of NiO and Fe-doped NiO thin films that can be used for RRAM application were studied. In the deposition process the system pressure, temperature, bias voltage, power etc. all play a very important role on the deposition rate. It was found that for low oxygen flow both NiO and Fe-doped NiO have a good deposition rate, but with increasing oxygen flow the deposition rate drops and at 10sccm the deposition rate was less than 0.1 A/sec. The MKS mass flow controller had an error of 2% and can only be used to control the oxygen gas flow above 0.4 sccm. So below the 0.4sccm it was not possible to perform reactive ion sputtering. To get an idea about the deposition with the presence of oxygen at low gas flow < 0.4sccm a new mass flow controller is being installed. So, in the future films can be deposited at lower oxygen flow for further investigation.

A substrate shutter was installed in the system to allow the plasma to become stable before the substrate is exposed to the deposition beam.

To verify the thickness obtained from ellipsometry measurement data, the thickness of the high pressure NiO oxygen flow series was also determined from XRR measurement data. The XRR fits gave similar thickness results. The roughness of the measured samples from ellipsometry and the XRR are far off from each other though; a future AFM study might give the solution of this problem.

All the samples show the rocksalt crystal structure. In case of thin films, although, the peaks are getting weaker for the higher oxygen flow samples, however, NiO and NiFeO sustain the rocksalt crystal structure.

The oxygen vacancies influence the crystallite size; with the decreasing oxygen vacancies the crystallite size decreases for both NiO and NiFeO. The micro-strain increases with adding Fe in NiO. The pole figure data shows the dominant {111} texture for high-pressure thick NiFeO films made with high or low oxygen flow. For NiO only the samples made at high oxygen flow show {111} texture. The low oxygen flow samples show {200} texture.

Oxygen vacancies plays a very important role on the electrical properties. For the high pressure thin films the resistivity increases with the oxygen flow and gets saturated at a certain point and then starts to drop. For the thick films it increases with the oxygen flow.

To get a better/ accurate idea about the crystal/particle size an SEM study needs to be planned, in addition, a Raman studies should be performed to confirm the crystal structure and provide additional information on micro-strain in the crystal.

The oxygen vacancy and Fe concentrations influence the magnetic properties of the NiO and NiFeO. As the oxygen flow increases the Verdet constant decreases. The Verdet constant is higher when iron is incorporated in the NiO crystal structure.

For further analysis we want to deposit the thin films on NaCl substrates and dissolve the NaCl to get free standing films. This could give additional informationon the MO effect and how it relates to oxygen vacancies and Fe concentrations. Furthermore, it could provide more information on how optical properties change through the film thickness.

APPENDIX

Appendix A

Standard Operating Procedure for Sputtering:

Load The Sample:

1. Check if the spindle is in the load-lock system. If not transfer the spindle from the chamber to the load-lock system following the procedure outlined below.

2. Make sure the high vacuum valve is closed. Screw is not visible (turn clockwise to close). Switch off the ion gauge (high vacuum gauge).

3. Switch off the power to the pumps of the load-lock system. On main rack at the top right.

4. Watch the pressure in the load-lock system. Double check that the pressure in the chamber does not rise. If it rises, make sure to stop the venting process.

5. One the load-lock system is at atmospheric pressure, lift the lit and place it on the three bumps under the load-lock system.

6. Remove the spindle and place it on a tissue on the instrument. Mount your sample. Only use the provided screws. Do not use standard stainless steel screws since that will damage the Mo spindle.

7. Place the spindle with the samples upside down on the fork. Make sure that two of the screws are lined up between the teeth of the fork.

8. Clean the gasket and the lit with a wipe with IPA. Make sure no particles are on

the lit and the vacuum ring.

9. Close and center the lit.

10. Switch on the pump of the load-lock at the right top of the rack. Monitor the pressure of the load-lock. It should go down to the 10^-5 torr range within a couple of minutes. If not, readjust the lit.

11. Once the load-lock is back in the 10^-6 torr range switch on the ion gauge in the main chamber.

12. Once the load-lock pressure is within a factor 10 of the vacuum chamber pressure you can open the high vacuum valve and load the sample. Before you do so make sure that the claw is raised, i.e. the mechanical translator on top of the vacuum system is below position 25 (sputter and transfer position). Slide the rod/fork carefully into the vacuum chamber. Move it all the way to the stop (black ring).

13. Lower the claw by moving the mechanical translation stage to position 40. Make sure that the fork/rod does not move away from the stop. The claw needs to get into the hole in the middle of the spindle. Look through the window as the claw approaches the spindle. Once in place, lock the claw in place by rotating the sample-rotator at the top of the vacuum system clockwise.

14. If locked move the mechanical translator back to a position below 25. Now remove the fork/rod carefully, and close the high vacuum valve.

15. Pump down the chamber until the pressure in the chamber is back to the 3*10^-7 torr range before starting the sputtering process.

DC deposition:

1. Switch off the ion gauge. Set the substrate temperature following the direction provided below if you decide to sputter above room temperature. Set the rotation of the spindle to 60 rotation per minute (at least one rotation per monolayer). Switch on the throttle. Set the Ar flow to 10-80 sccm, and turn the gas on. Check the capacitance gauge until chamber pressure is constant. You should be able to start a dc-gun with 4-5 mTorr.

2. Set time to 0 and power to 10%, but don't turn the gun on.

3. Turn the gun on in the software. Once the plasma is started, a purple indicator will light up on the program.

4. Check through the vacuum window if the gun is indeed on. Now set the power to what you need for deposition, make sure to set the time first and not more than 1 watt per second.

5. When the set-point power is reached, pre-sputter for 30 seconds.

6. Open the shutter to start the deposition process by clicking the big button in the program. Time your deposition. Do not deposit for more than 600 seconds.

7. Click the big button again to stop the sputtering.

8. Reduce the power of the gun by setting first the time interval to the used power and then setting the power to 0%.

9. Turn off the gas after this step.

10. If you want to make a thicker film, cool the gun for 5 minutes and restart the deposition process.

11. Once you are done, stop the sample rotation, and switch off the substrate heater.

12. If the sample temperature is back to room temperature remove the sample for the sputter chamber following the opposite of the loading process.

RF deposition:

1. Switch off the ion gauge. Set the substrate temperature following the direction provided below if you decide to sputter above room temperature. Set the rotation of the spindle to 60 rotation per minute (at least one rotation per monolayer).

2. Set Ar flow to 5 sccm, and turn gas on. Set time to 0 and power to 10%, but don't switch the gun on.

3. Close the high vacuum valve to the turbo pump, and check the gauge. Wait until the chamber pressure reaches up to 2.5*10^-2 Torr. Turn the gun on. Check if the purple light is on. If not repeat step 2 at a little higher pressure.

4. When the purple light turns on, throttle the high vacuum valve to the turbo pump. The plasma is on now. Check through the vacuum window that the gun is on.

5. Now set the power to what you need for deposition, make sure to set the time first and not more than 1 watt per second.

6. When the set-point power is reached, pre-sputter for 30 seconds.

7. Open the shutter to start the deposition process by clicking the big button in the program. Time your deposition. Do not deposit for more than 600 seconds.

8. Click the big button again to stop the sputtering.

9. Reduce the power of the gun by setting first the time interval to the used power

and then setting the power to 0%.

10. Turn off the gas after this step.

11. If you want to make a thicker film, cool the gun for 5 minutes and restart the deposition process.

12. Once you are done, stop the sample rotation, and switch off the substrate heater.

13. If the sample temperature is back to room temperature remove the sample for the sputter chamber following the opposite of the loading process.

Bias Cleaning:

1. First keep the main chamber valve wide open and adjust the Ar gas flow to make the chamber pressure 1mT (in my case it was 38 sccm).

2. Turn on RF#1 power supply and raise the power 40% i.e. 20W (max power is 50W).

3. Switch on the plasma switch and the FWD power will raise to 20W.

4. Close the main chamber valve to ramp up the pressure, as soon as the pressure goes to ~30mT immediately throttle the main chamber valve and you will see the plasma glow.

5. Adjust the gas flow to keep the pressure 3~5mT (in my case the gas flow was 30 sccm to get the pressure at 5mT).

6. Clean the substrate maximum 5 minutes or 300s.

7. Ramp down the power to 0W by 1W/s.

8. Turn off the gas flow.

9. Open the main Chamber valve.

Copra Cleaning:

1. Power on the COPRA PS (RF#3 in the middle rack).

2. Push the PGM button and push the ‘UP’ & ‘DOWN’ button to change to ‘PANEL’ mode.

3. Manually set the plasma power to 150W (using the ↑ ↓ on the right side).

4. Turn on the DELTA ES 030 power supply and increase the current to 1.9A which will give you the voltage ≈3.0V.

5. With the VAT open set the Ar GAS FLOW to GN 4 (Copra gas) to ~9 sccm.

6. ‘CLOSE’ the VAT to allow the chamber pressure to climb up. At the chamber pressure ≈ 20 to 25 mT, turn the RF POWER on at RF #3.

7. Check the reflected power. If the reflected power is larger than 10 Watt immediately shut of the plasma (Can you check manual) and throttle the chamber.

8. If the reflected power is less than XX watt, throttle the chamber and adjust the knobs at the bottom of the Copra gun to adjust the reflected power to zero if necessary.

9. Look for the plasma inside the chamber. If plasma is not on in the chamber switch off the PS. (If you cannot see the plasma do the process numbers 6, 7, and 8 again).

[Caution: Don’t let the chamber pressure climb up more than 60mTorr]

10. To keep the REF PWR ≈ 0 you might need to vary the LOAD & TUNE at the bottom of the chamber.

11. Once the Plasma is tuned and operating, switch to the power of the RF# 3 power supply to 250W in two steps, i.e. 200 Watt (adjust pressure to 4 sccm, and adjust the reflected power to zero) and 250 (adjust pressure slowly to 2.6 sccm, and adjust the

reflected power) The latter should give you a chamber pressure of approximately ≈ 1mT.

12. Clean your sample for max ≈300s.

13. When you are done with the COPRA cleaning power off the COPRA gun (RF Power supply 3). First lower the power to 150 adjust the reflected power. Then lower the power to zero. As there is no target and no lining in our Copra you can lower the power rather quickly.

14. Make the GAS FLOW ≈0.

15. Open the VAT.

<u>Unload The Sample:</u>

1. Turn the ion gauge on to check chamber pressure. If it in the same range (within a factor 10) as load-lock, open the high vacuum valve between chamber and sample load-lock holder.

2. Make sure that the claw and spindle are up, i.e. below position 25. Slide the rod/fork carefully into the vacuum chamber. Move the rod/fork all the way to the stop, i.e. black ring on the rod.

3. Once the fork is at the position of the sample-holder lower the spindle onto the fork (position 40). Turn it counter-clockwise to unlock the spindle from the claw.

4. Once in place lift the claw up by moving the mechanical translator to a position below 25. Carefully remove the fork, and close the high vacuum valve.

5. Switch off the power to the pumps of the load-lock system.

6. Watch the pressure in the load-lock system go up.

7. When the load-lock system is at atmospheric pressure, lift the lit and place it on the three bumps under the load-lock system.

8. Take the sample out and lid the load lock.

Appendix B

Thickness was measured with the ellipsometer and then the spectroscopic data were fit with the model.

Fitting with Wavelength by Wavelength:

a. NiO with $Ar:O_2$=40:10(in sccm)

Include Surface Roughness = OFF
Layer # 1 = WvlByWvl Thickness # 1 = **20.75 nm** (fit)
Substrate = BSplineFitQuartzsubstrate
Angle Offset = 0.00

MSE = 1.405
Thickness # 1 = 20.75±0.497 nm

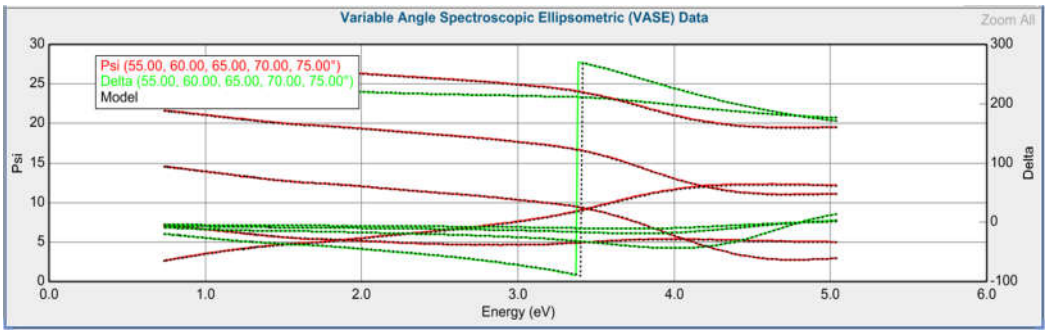

b. NiO with $Ar:O_2$=43:7(in sccm)

Include Surface Roughness = OFF
Layer # 1 = WvlByWvl Thickness # 1 = **27.18 nm** (fit)
Substrate = BSplineFitQuartzsubstrate
Angle Offset = 0.00

MSE = 0.619
Thickness # 1 = 27.18±0.161 nm

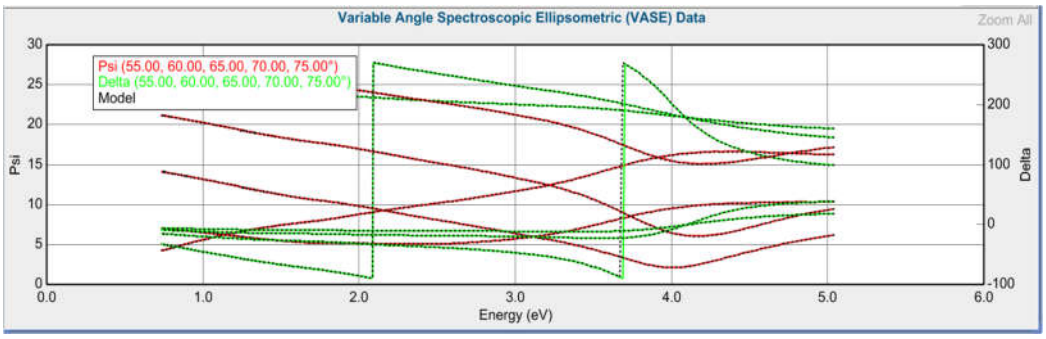

c. NiO with Ar:O_2=45:5(in sccm)

Include Surface Roughness = OFF
Layer # 1 = WvlByWvl Thickness # 1 = 65.39 nm
Substrate = BSplineFitQuartzsubstrate
Angle Offset = 0.00 MSE = 0.629

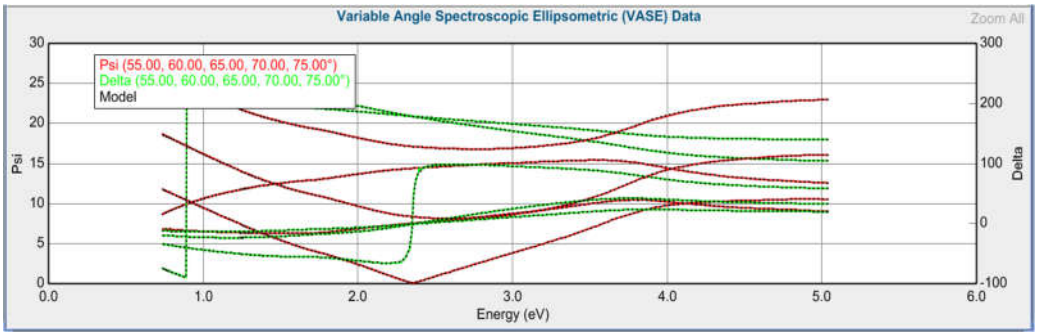

d. NiO with Ar:O_2=46.5:3.5(in sccm)

Include Surface Roughness = ON Roughness = 2.00 nm
Layer # 1 = WvlByWvl Thickness # 1 = **75.81 nm** (fit)
Substrate = BSplineFitQuartzsubstrate
Angle Offset = **0.0240** (fit)

MSE = 0.764
Thickness # 1 = 75.17±0.055 nm
Angle Offset = 0.0601±0.003611

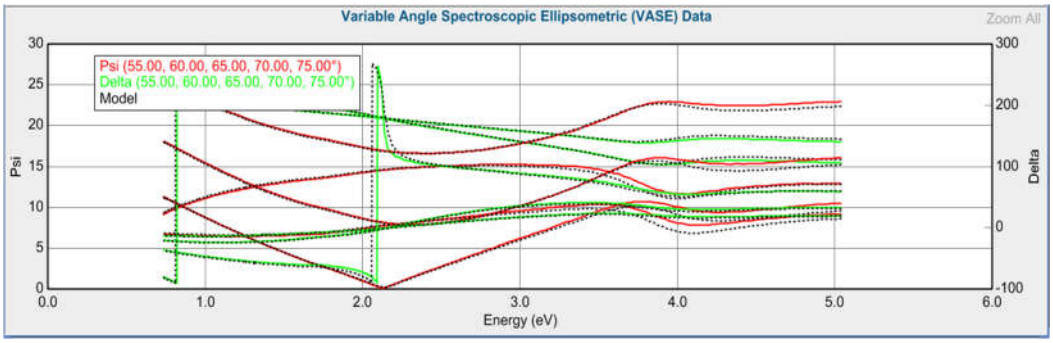

e. NiO with Ar:O_2=47.5:2.5(in sccm)

Include Surface Roughness = ON Roughness = 4.33 nm
Layer # 1 = WvlByWvl Thickness # 1 = 64.89 nm
Substrate = BSplineFitQuartzsubstrate
Angle Offset = 0.00 MSE = 0.710

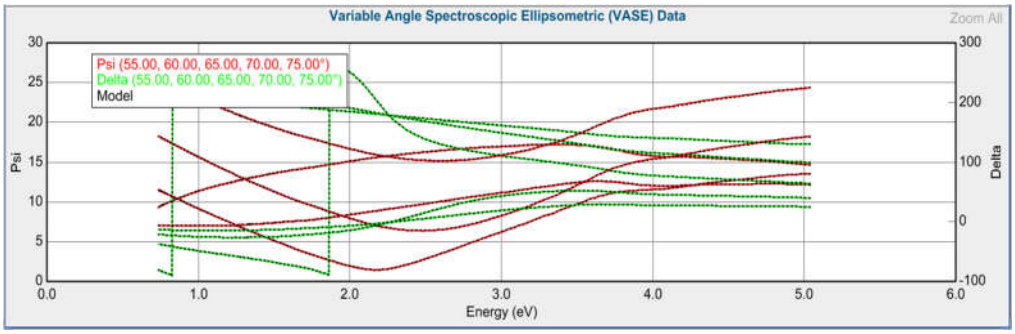

f. NiO with $Ar:O_2$=48.2:1.8(in sccm)

Include Surface Roughness = ON Roughness = 2.29 nm
Layer # 1 = WvlByWvl Thickness # 1 = 50.92 nm
Substrate = BSplineFitQuartzsubstrate
Angle Offset = 0.00 MSE = 0.793

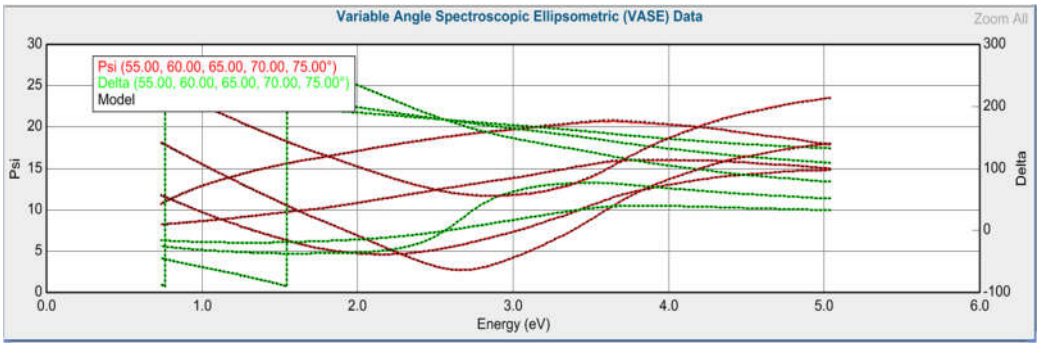

g. NiO with $Ar:O_2$=48.75:1.25(in sccm)

Include Surface Roughness = ON Roughness = **4.49 nm** (fit)
Layer # 1 = WvlByWvl Thickness # 1 = **58.36 nm** (fit)
Substrate = BSplineFitQuartzsubstrate
Angle Offset = **0.00152** (fit)

MSE = 0.453
Roughness = 4.87±0.037 nm
Thickness # 1 = 59.00±0.036 nm
Angle Offset = 0.00497±0.002041

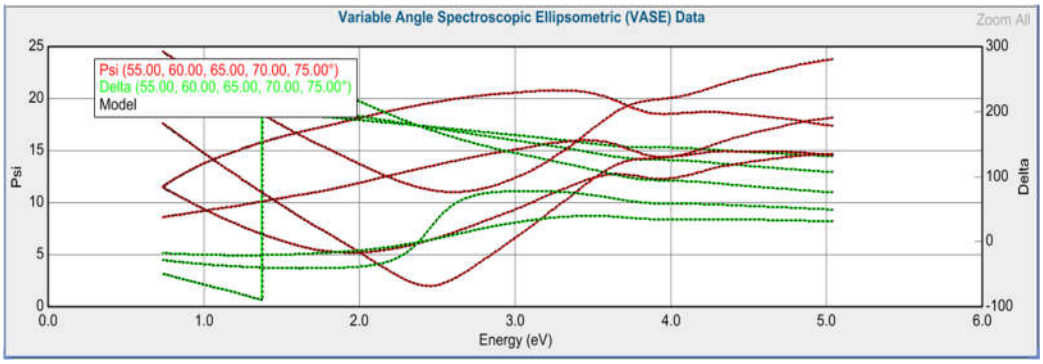

h. NiO with Ar:O_2=49.6:0.4(in sccm)

Layer # 1 = WvlByWvl Thickness # 1 = **57.19 nm** (fit)
Substrate = BSplineFitQuartzsubstrate

MSE = 0.429
Roughness = 0.70±0.057 nm
Thickness # 1 = 57.19±0.046 nm

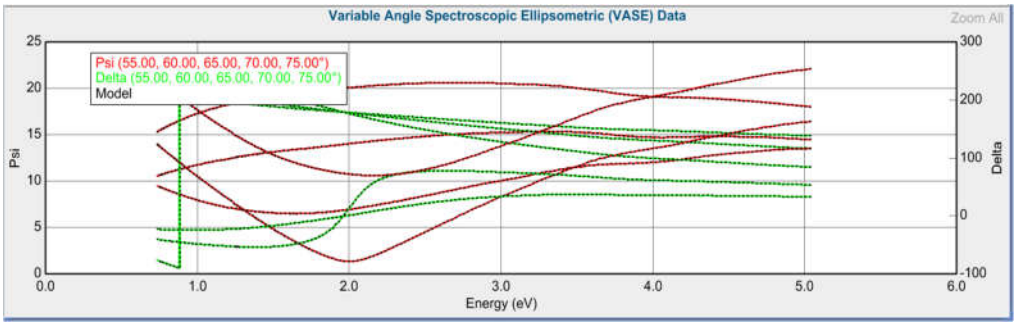

Fitting eith B-Spline model:

i. NiO with Ar:O_2=40:10(in sccm)

Layer # 1 = B-Spline Thickness # 1 = **11.24 nm** (fit)
Substrate = BSplineFitQuartzsubstrate

MSE = 1.342
Thickness # 1 = 11.24±0.465 nm

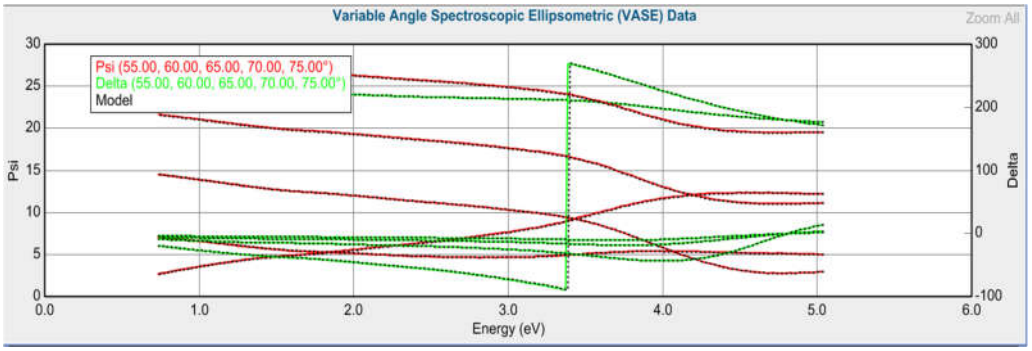

j. NiO with Ar:O_2=43:7(in sccm)

Layer # 1 = B-Spline Thickness # 1 = **26.92 nm** (fit)
Substrate = BSplineFitQuartzsubstrate

MSE = 0.693
Thickness # 1 = 26.92±0.180 nm

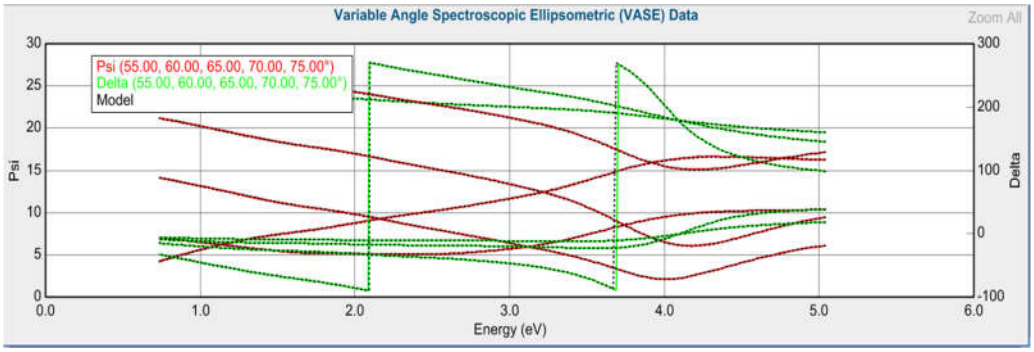

k. NiO with Ar:O_2=45:5(in sccm)

Layer # 1 = B-Spline Thickness # 1 = **64.39 nm** (fit)
Substrate = BSplineFitQuartzsubstrate

MSE = 0.814
Thickness # 1 = 64.39±0.047 nm

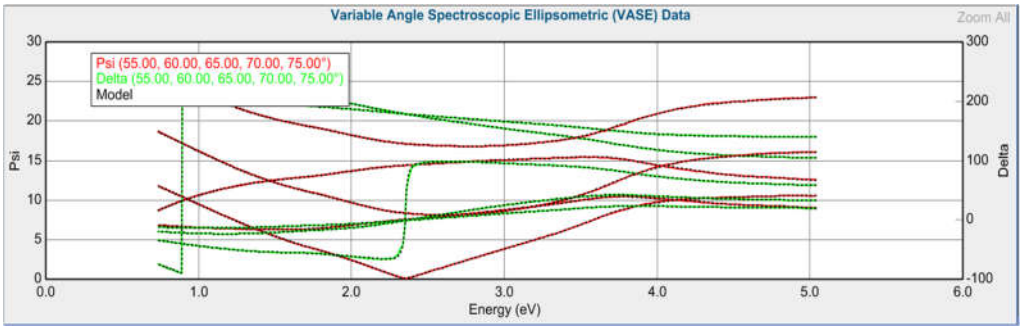

l. NiO with Ar:O_2=46.5:3.5(in sccm)

Layer # 1 = B-Spline Thickness # 1 = **72.09 nm** (fit)
Substrate = BSplineFitQuartzsubstrate

MSE = 1.893
Thickness # 1 = 72.09±0.085 nm

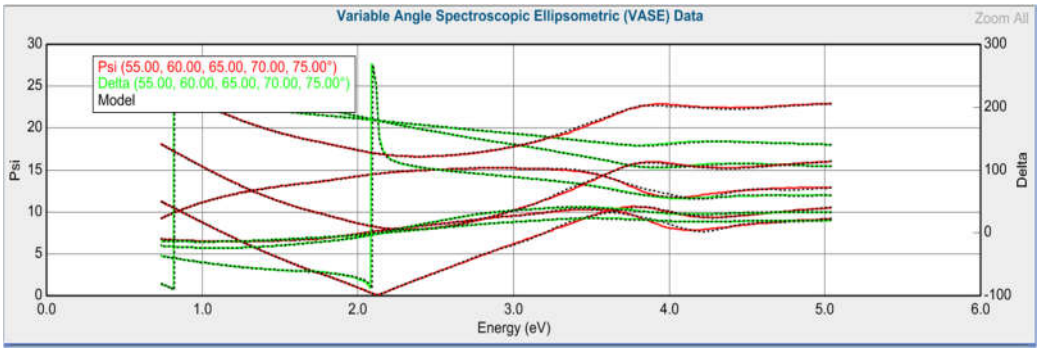

m. NiO with Ar:O_2=47.5:2.5(in sccm)

Layer # 1 = B-Spline Thickness # 1 = **62.42 nm** (fit)
Substrate = BSplineFitQuartzsubstrate

MSE = 1.449
Thickness # 1 = 62.42±0.136 nm

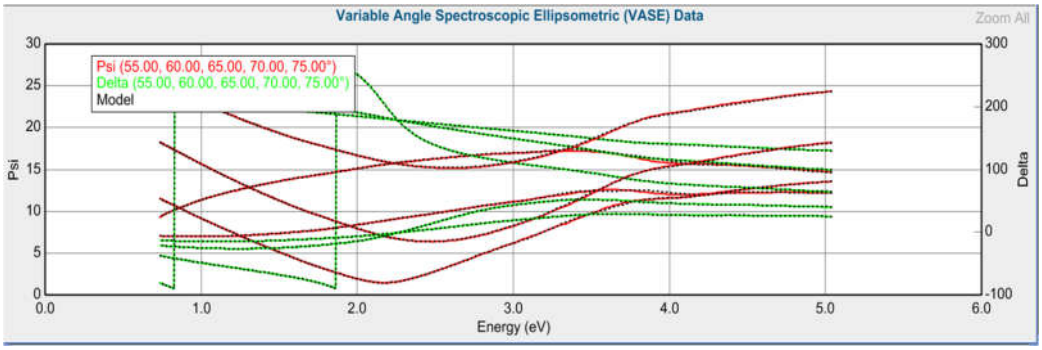

n. NiO with Ar:O_2=48.2:1.8(in sccm)

Layer # 1 = B-Spline Thickness # 1 = **50.53 nm** (fit)
Substrate = BSplineFitQuartzsubstrate

MSE = 1.046
Thickness # 1 = 50.53±0.069 nm

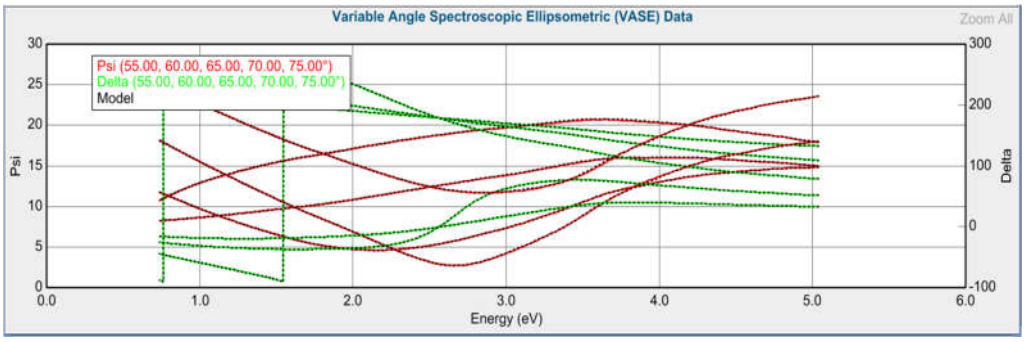

o. NiO with $Ar:O_2$=48.75:1.25(in sccm)

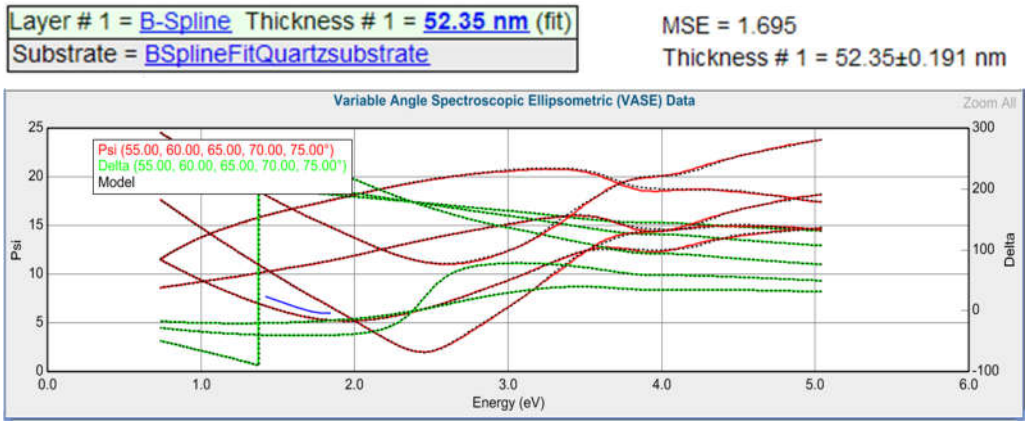

p. NiO with $Ar:O_2$=49.6:0.4(in sccm)

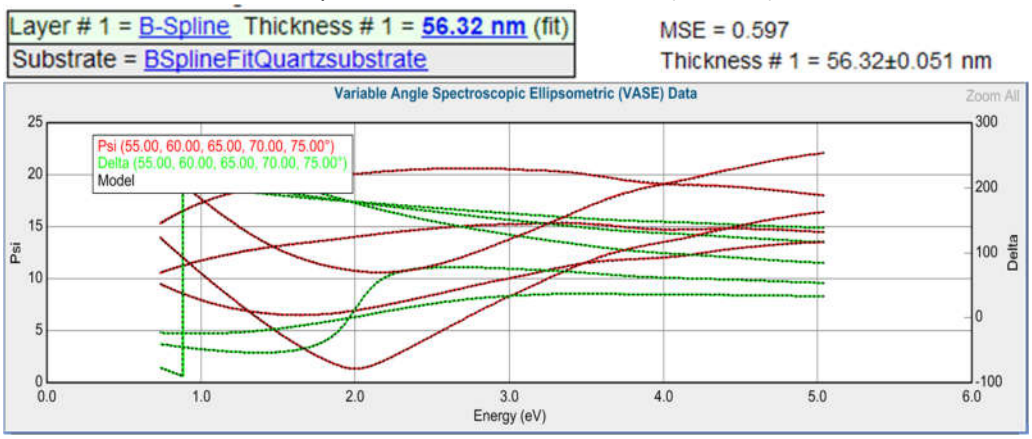

Appendix C

Density, thickness and roughness were measured by X-Ray Reflictivity.

a. NiO with Ar:O_2=49.6:0.4(in sccm)

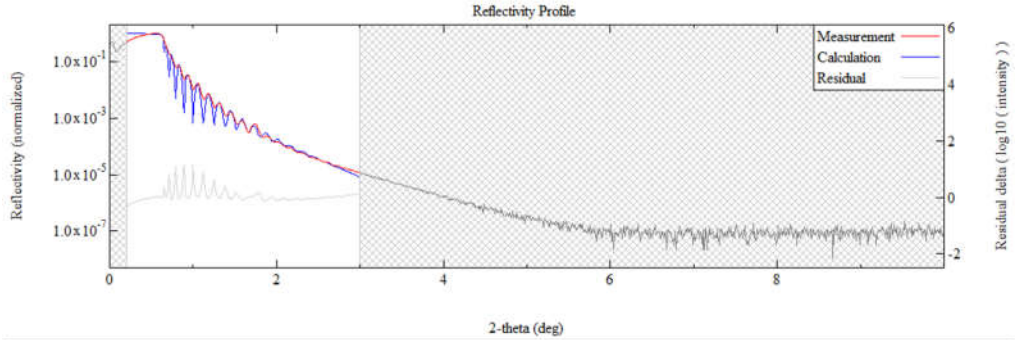

Layer Parameter List | Layer Structure Model

No.	Layer name	Thickness...	Density(g...	Roughne...	Depth dis...	Bottom d...	# of perio...	Surface r...	Delta	Beta
1	NiO	57.487[-]	5.4761[-]	1.81693[-]	No distrib...				1.5540e-0...	2.5525e-0...
0	SiO2	0.0[-]	0.82[-]	0.71994	No distrib...				2.6580e-0...	3.4640e-0...

b. NiO with Ar:O_2=48.75:1.25(in sccm)

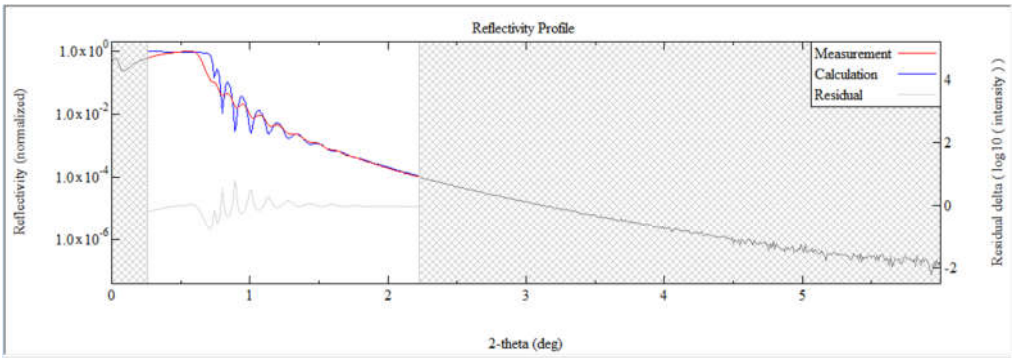

Layer Parameter List | Layer Structure Model

No.	Layer name	Thickness...	Density(g...	Roughne...	Depth dis...	Bottom d...	# of perio...	Surface r...	Delta	Beta
1	NiO	50.10[-]	6.946[-]	2.6295[-]	No distrib...				1.9711e-0...	3.2376e-0...
0	SiO2	0.0[-]	2.07[-]	0.659[-]	No distrib...				6.7100e-0...	8.7444e-0...

c. NiO with Ar:O_2=48.2:1.8(in sccm)

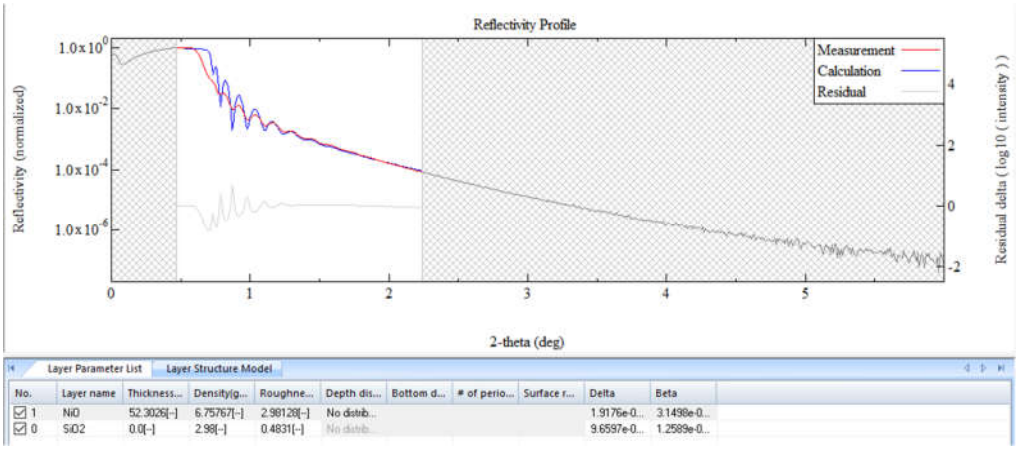

d. NiO with Ar:O_2=47.5:2.5(in sccm)

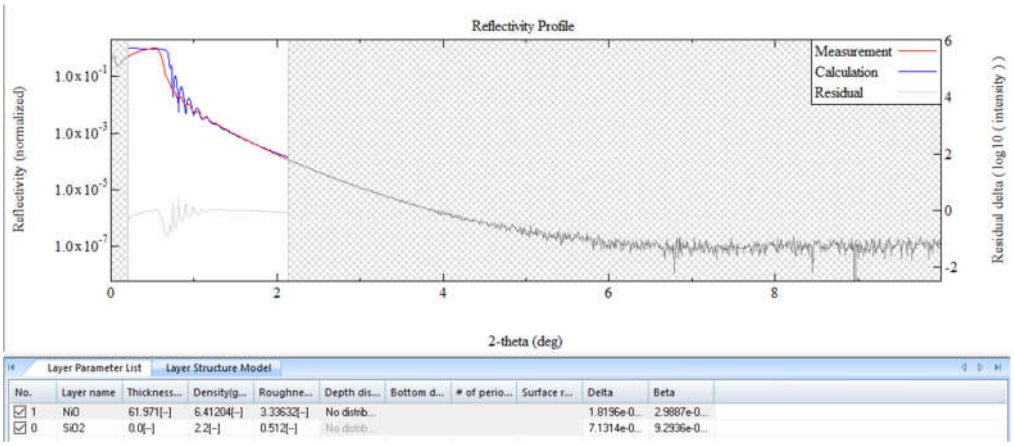

e. NiO with Ar:O_2=46.5:3.5(in sccm)

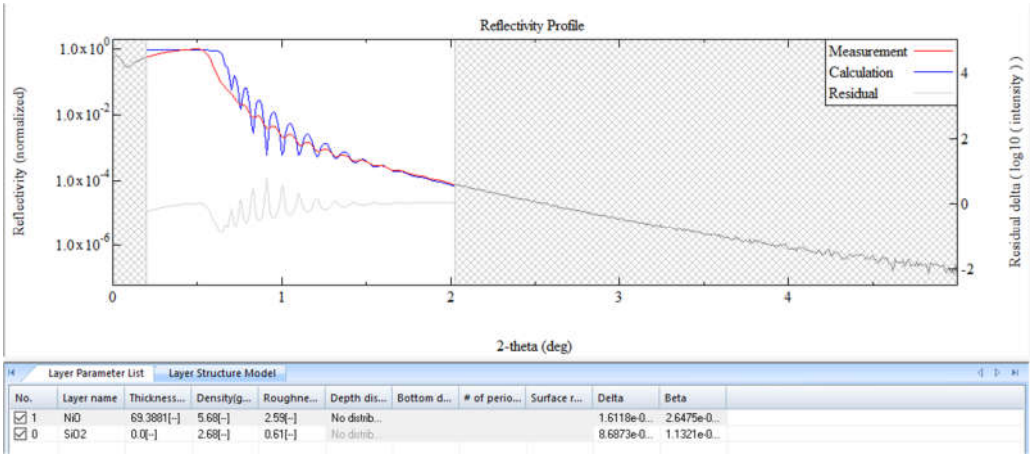

f. NiO with Ar:O_2=45:5(in sccm)

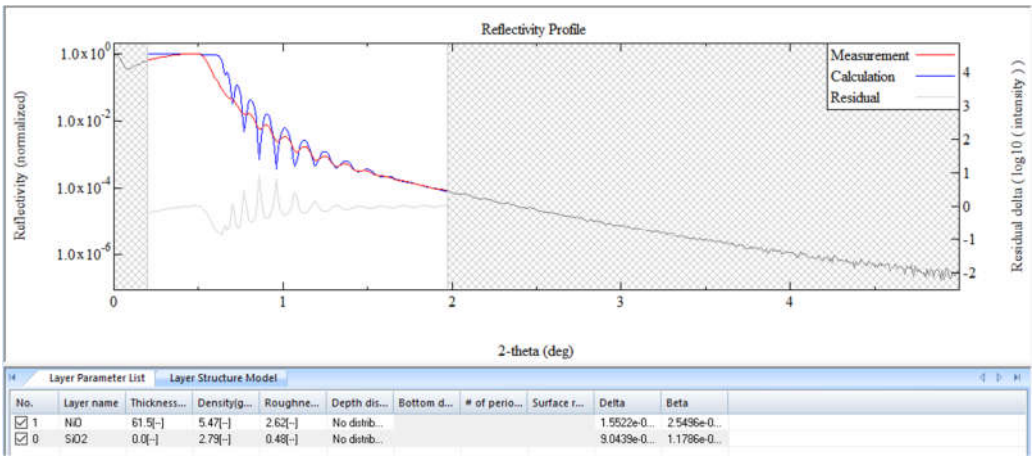

g. NiO with Ar:O_2=43:7(in sccm)

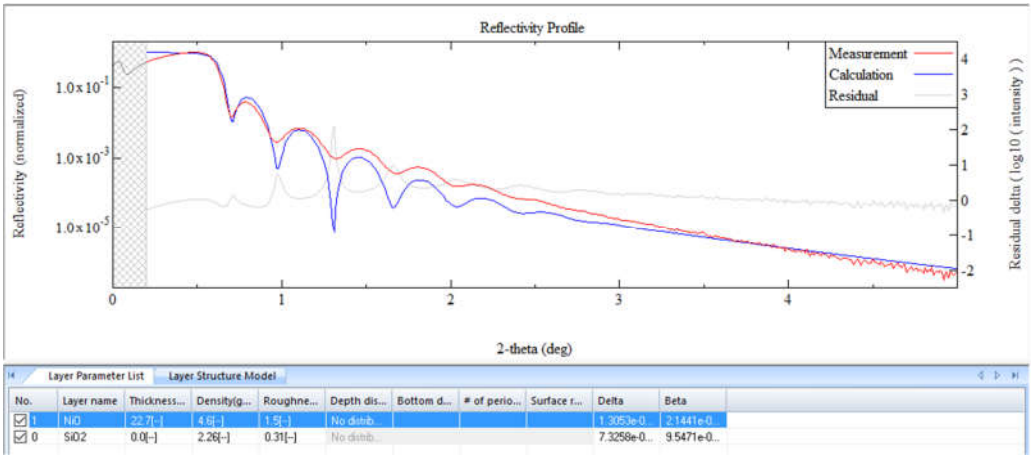

h. NiO with Ar:O_2=40:10(in sccm)

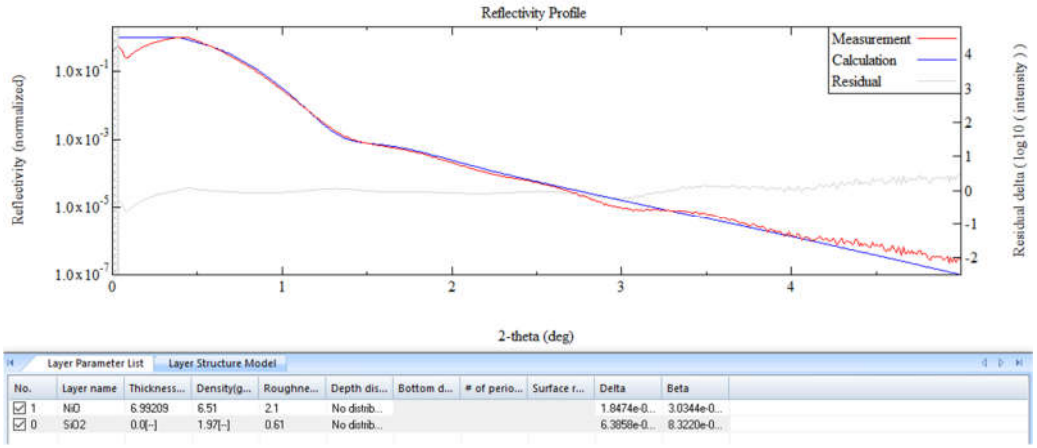

Appendix D

Faraday rotation measurements of the samples with 19%(atomic) of Fe doped NiO with different oxygen flow (5%, 7%, 10%, 14%, 20%).

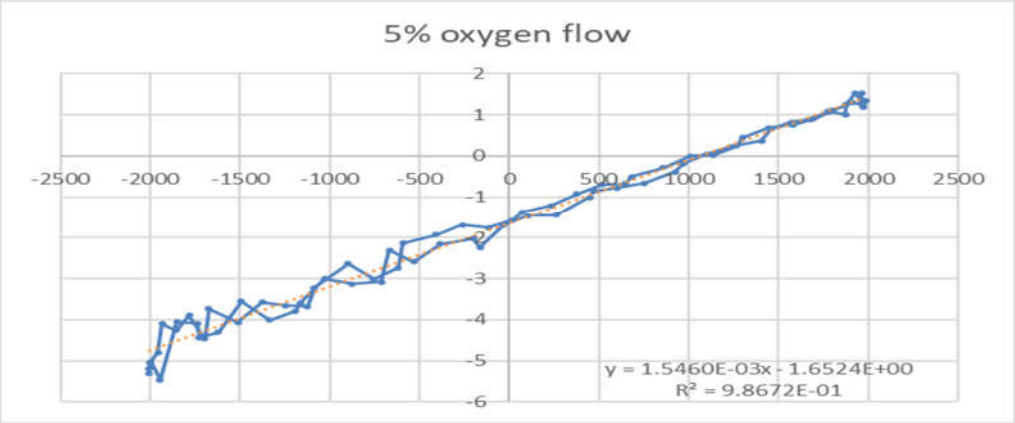

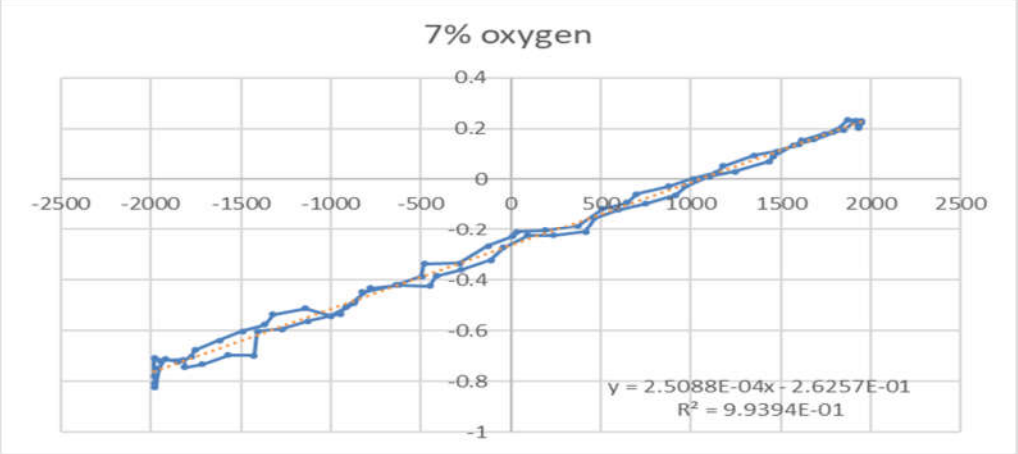

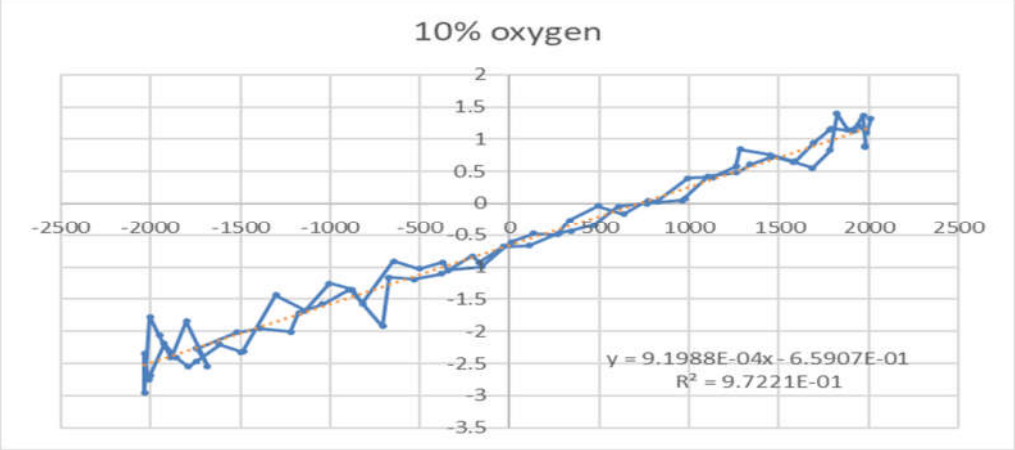

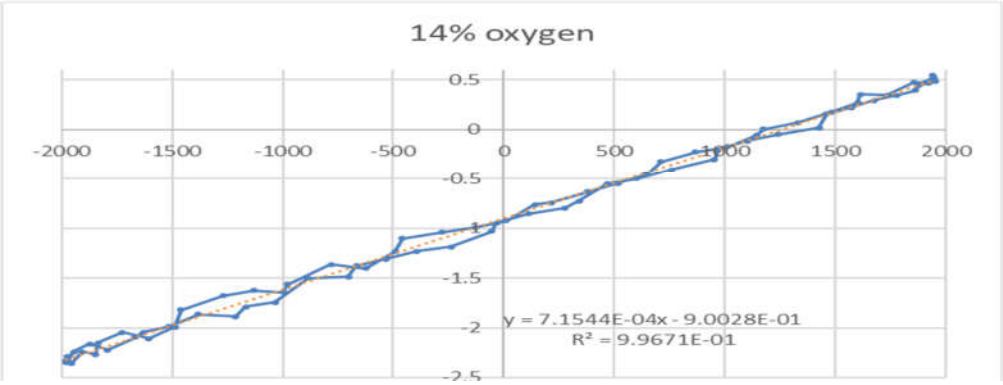

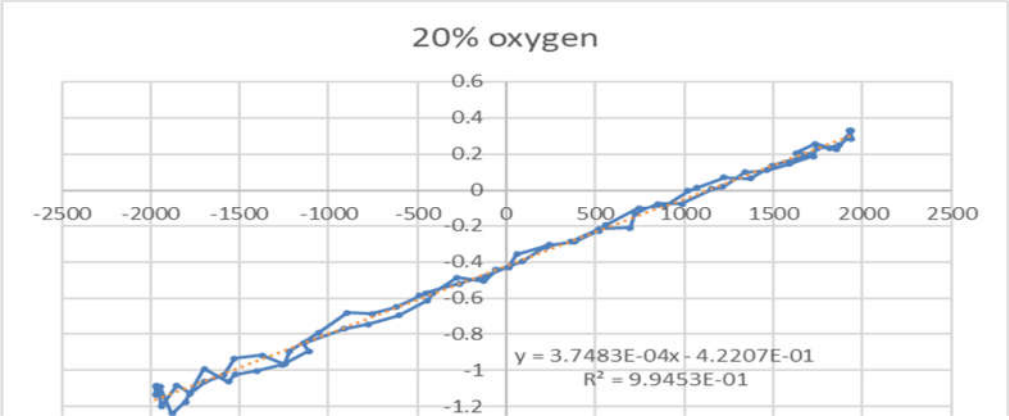

Table D-1: Variation of slope of Kerr rotation with respect to oxygen concentration.

O_2 percentage in sputter gas	**Slope of Kerr Rotation**
5%	1.55×10^{-3}
7%	2.51×10^{-4}
10%	9.20×10^{-4}
14%	7.15×10^{-4}
20%	3.75×10^{-4}

Appendix E

Table E-1: Variation of resistivity with the partial pressure of Ar and O2 gas flow.

Ar:O_2(in sccm**)**	**Resistivity(Ω cm)**
49.6:0.4	314.2078746
48.75:1.25	7618.839826
48.2:1.8	10721.39968
47.5:2.5	199989.6851
46.5:3.5	342721.009
45:5	3030336.066
43:7	620351.1814
40:10	2422.191611

REFERENCES

1. J. Thornton, Influence of apparatus geometry and deposition conditions on the structure and topography of thick sputtered coating, J. Vac. Sci. Technol., Vol. 11, (1974) 666-670.
2. Y.M. Lu, W.S. Hwang, J.S. Yang, H.C. Chuang, Properties of nickel oxide thin films deposited by RF reactive magnetron sputtering, Thin Solid Films 420–421 (2002) 54–61.
3. James Landon, et al., spectroscopic characterization of mixed iron nickel oxide electro catalyst for the oxygen evolution reaction in alkaline electrolytes, ACS Catal. (2012) 2, 1793-1801.
4. Yuan- Hua Lin, et al., Ferromagnetism and electrical transport in iron doped nickel oxide, Phys. Rev. B 73(2006) 193308.
5. Magneto-Optics and Spectroscopy of Antiferromagnets, V.V. Eremenko, N.F. Kharchenko, Yu G. Litvinenko, V.M. Naumenko, springer verlag, 1992, ISBN -13: 978-1-4612-7694-4.
6. H. Bi, S. Li, Y. Zhang, Y. Du, Ferromagnetic-like behavior of ultrafine NiO nanocrystallites, J. Magn. Magn. Mater. 277, 363-367 (2004).
7. Issei Sugiyama, Naoya Shibata, Zhongchang Wang, Shunsuke Kobayashi, Takahisa Yamamoto, Yichi Ikuhara, Ferromagnetic dislocations in antiferromagnetic NiO: Natur Nanotechnology 8, 266-270 (2103).
8. Kwanruthai Wongsaprom, Santi Maensiri, Sythesis and Room Temperature Magnetic Behavior of Nickel Oxide Nanocrystallites, Chiang Mai J. Sci. (2013) 40(1), pp. 99-108.
9. Kazuro Kuroda, Takuya Satoh, Sung-Jin Cho, Ryugo Iida, Tsutomu Shimura, “Measurement of inverse Faraday effect in NiO using ultrashort laser pulses, Proc. of SPIE vol. 7728, 77281Z (2010).
10. Ashcroft and Mermin. Solid State Physics. ISBN 0030839939.
11. Chiang, Yet-Ming; Birnie III, Dunbar; Kingery, W. David. Physical Ceramics: Principles for Ceramic Science and Engineering. John Wiley & Sons. ISBN 0-471-59873-9.
12. Mattila, T.; Nieminen, R.M. (1995). "Direct Antisite Formation in Electron Irradiation of GaAs". Physical Review Letters. 74 (14): 2721–2724.
13. J. A. Thornton, ‘The influence of apparatus geometry and deposition conditions on the structure and topography of thick sputtered coatings’, J. Vac. Sci. Technol. Vol. 11 p-666 (1974).
14. https://en.wikipedia.org/wiki/Crystallographic_defect.
15. Per Kofsad and Truls Norby. ‘Defects Chemistry and Reactions in Solid’ (KJM 4120). University of Oslo.

16. Timothy M. Wilson (1970). 'A Study of the electronic structure of the first-row Transitional-Metal Compounds'. International Journal of Quantum Chemistry. Vol IIIS, p757-774.
17. B. H. Brandow (1977). 'Electronic structure of Mott insulators'. Advances in Physics. Sep77, Vol. 26, Issue 5, p651.
18. A. Barry Kunz (1981). 'Electronic Structure of NiO'. J. Phys. C: Solid State Phys. 14 L455.
19. J. G. Aiken and A. G. Jordan (1968). 'ELECTRICAL TRANSPORT PROPERTIES OF SINGLE CRYSTAL NICKEL OXIDE' J. Phys. Chem. Solids, Vol. 29, p2153-2167.
20. G.T. Surrat, and A.B. Kunz (1977), 'Unrestricted Hartree-Fock calculations for a cluster model of NiO', Sol.St.Com. 23, p555.
21. G. Madhy, V. Biju (2014). 'Effect of Ni2+ and O2- vacancies on the electrical and optical properties of nanostructured nickel oxide synthesized through a facile chemical route', Physics E60, p200-205.
22. J. B. Goodenough, 'Progress in Solid State Chemistry', Vol. 5, edited by H. Reiss (Pergamon Press, New York, 1971) p. 271.
23. J. H. DeBoer and E. J. W. Verwey (1937), Proc. Phys. Soc. (London) 49, (extra part).
24. E. J. W. Verwey (1948), Chem. Weekblad 44, 705—708.
25. W. L. Jang, Y. M. Lu, W. S. Hwang, C. L. Dong, P. H. Hsieh, C. L. Chen, T. S. Chan, and J. F. Lee (2011), 'A study of thermal decomposition of sputtered NiO films', EPL 96, 37009.
26. Jae Wan Park, Jong-Wan Park, Dal-Young Kim, and Jeon-Kook Lee (2005), 'Reproducible resistive switching in nonstoichiometric nickel oxide films grown by rf reactive sputtering for resistive random access memory applications', Journal of vacuum science and technology, A 23, 1309.
27. W. Bruckner R Kaltofen, J. Thomas, M. Hecker, M. Whlemann, A. Oswald, D. Elefant, and C. M. Schneider (2003), 'Stress development in sputtered NiO thin films during heat treatment', J. of App. Phy. Vol. 94, Number 8.
28. Marek Guzeiwicz, Jakub Grochowski, Michal Borysiewicz, Eliana Kaminska, Jaroslaw Z. Domagala, Witold Rzodkiewicz, Bartlomiej S. Witkowski, Krystyna Golaszewska, Renata Kruszka, Marek Ekielski, anna Piotrowska (2011), 'Electrical and optical properties of NiO films deposited by magnetron sputtering', Optica Applicata. Vol. XLI, No. 2.
29. S. C. Chen et. al., 'Characterization and properties of NiO films produced by rf magnetron sputtering with oxygen ion source assistance', Thin Solid Films (2014).
30. Dong-Jin Yun, and Shi-Woo Rhee (2008), 'Deposition of NiOx thin films with radio frequency magnetron sputtering and their characteristics as a source/drain electrode for the pentacene thin film transistor', J. Vac. Sci. Technol. B 26(5).
31. A. Karpinski, A. Ferrec, M. Richard-Plouet, L. Cattin, M. A. Djouadi, L. Drohan, P.-Y. Jouan (2012), 'Deposition of nickel oxide by direct current reactive sputtering effect of oxygen partial pressure', Thin Solid Films 520, 3609-3613.

32. Y. M. Lu, W. S. Hwang, J. S. Yang, H. C. Chuang (2002), 'Properties of NiO thin films deposited by RF reactive magnetron sputtering', Thin solid films 420-421, 54-61.
33. T. C. Peng, X. H. Xiao, X. Y. Han, X. D. Zhou, W. Wu, F. Ren, C. Z. Jiang (2011), 'Characterization of DC reactive magnetron sputtered NiO films using spectroscopic ellipsometry', Applied Surface Science 257, 5908-5912.
34. A. Karpinski, N. Ouldhamadouche, A. Ferrec, L. Cattin, M. Richard-Ploued, L. Brohan, M. A. Djouadi, P-Y Jouan (2011), 'Optical characterization of transparent nickel oxide films deposited by DC current reactive sputtering', Thin Solid Films 519, 5167-5770.
35. I. Fasaki, A. Koutoulaki, M. Kompitsas, C. Charitidis (2010), 'Structural, electrical, and mechanical properties of NiO thin films grown by pulsed laser deposition', App. Surface Sci. 257, 429-433.
36. F. Saadati, A. -R. Grayeli, H. Savaloni (2010), 'Dependence of the optical properties of NiO thin films on film thickness and nano-structure', Journal of Theoretical and Applied Physics, 4-1, 22-26.
37. K. Ashok (2011), 'Characterization of nickel oxide thin film- DC reactive magnetron sputtering', Surface Review and Letters, Vol 18, Nos. 1 & 2, 11-15.
38. Andre Venter, Johannes R. Botha (2011), 'Optical and electrical properties of NiO for possible dielectric applications', S. Afr. J. Sci 107(1/2).
39. Ming Yang, Haifeng Pu, Qianfei Zhou, Qun Zhang (2012). 'Transparent p-type conducting K-doped NiO films deposited by pulsed plasma deposition', Thin Solid Films 520, 5884-5888.
40. S. C. Chen, T. Y. Kuo, Y. C. Lin, H. C. Lin (2011). 'Preperation and properties of p-type transparent conductive Cu-doped NiO films', Thin Solid Films 519, 4944-4947.
41. Yarraguntla Ashok Kumar Reddy, Akepati Sivasankar Reddy, Pamanji Sreedhara Reddy (2013), 'Substrate temperature dependent properties of Cu doped NiO films deposited by DC reactive magnetron sputtering', J. Mater. Sci. Technol. 29(7), 647-651.
42. https://www.webelements.com/iron/atoms.html.
43. https://www.webelements.com/nickel/atoms.html.
44. Mohammad A. Ati, Hayder Khudhair, Shadab Dabagh, R. M. Rosnan, Ali A. Ati (2014), 'Synthesis and Characterization of Cobalt doped Nickel-Ferrites Nanocrystalline by Co-precipitation Method', International Journal of Scientific & Engineering Research, Vol. 9, Issue 9. 927-930.
45. C. L. Chang, G. Chern, C. L. Chen, H. H. Hsieh, C. L. Dong, W. F. Pong, C. H. Chao, H. C. Chien, S. L. Chang (1999), 'Electronic States and structural characterization in single-crystal Fe-Ni-O alloy thin films grown by molecular beam epitaxy', Solid State Communications 109, 599-604.
46. James Landon, Ethan Demeter, Nilay Inoglu, Chris Keturakis, Israel E. Wachs, Relja Vasic, Anatoly I. Frenkel, and John R. Kitchin (2012), 'Spectroscopic Characterization of Mixed Fe-Ni Oxide Electrocatalysts for the Oxygen Evolution Reaction in Alkaline Electrolytes', ACS Catal. 2, 1793-1801.

47. Anup K. bandypadhyay, Steven E. Rios, Albert Tijerina, Carlos J. Gutierrez (2004), 'The influence of ion beam sputtering geometry on metastable ($Ni_{81}Fe_{19}$)O/$Ni_{81}Fe_{19}$ exchange biased blayers', Journals of Alloys and Compounds 369, 217-221.
48. Shaohui Liu, Jianfeng Jia, Jiao Wang, Shijiang Liu, Xinchang Wang, Hongzhang Song, Xing Hu (2012), 'Synthesis of Fe-doped NiO nanofibers using electrospinning method and their ferromagnetic properties', Journal of Magnetism and Magnetic Materials 324, 2070-2074.
49. Gagan Dixit, J. P. Singh, R. C. Srivastava, H. M. Agrawal, R. J. Chaudhary (2012), 'Structural, Magnetic and optical studies of nickel ferrite thin films', Adv. Mat. Lett. 3(1), 21-28.
50. Ulrike Luders, Manuel Bibes, Jean-Francois Bobo, Matteo Cantoni, Riccardo Bertacco, and Josep Fontcuberta (2005), 'Enhanced magnetic moment and conductive behavior in $NiFe_2O_4$ spinel ultrathin films', Physical Review B 71, 134419.
51. Steven E. Rios, Anup K. Bandyopadhayay, Casey Smith, Carlos J. Gutierrez, 'The enhancement of magnetically ordered oxide layered structures using oxygen radical processing'.
52. P. Perera, A. G. Ayala, and C. J. Guiterrez (1999), 'Metastable permalloy monoxide based spin valves and pseudo-spin valves', Journal of Applied Phisics, Vol. 85, Number 8.
53. Safoura Seifikar, Bridget Calandro, Elisabeth Deeb, Edward Sachet, Jijin Yang, Jon-Paul Maria, Nazanin Bassiri-Gharb, and Justin Schwartz (2012), 'Structural and magnetic properties of biaxially textured NiFe2O4 thin films grown on c-plane sapphire', Journal of Applied Physics 112, 123910.
54. W. R. Grove, Philos. 'On the Electro-Chemical Polarity of Gases' Trans. Faraday Soc. 87 (1852).
55. I. Langmuir, 'Positive Ion Currents from the Positive Column of the Mercury Arc.' General Electric Rev. 26:731 (1923)
56. https://www.arl.psu.edu/mm_mp_ac_sputtering.php
57. G. K. Wehner, 'Sputtering of Metal Single Crystals by Ion Bombardment' Adv. Electron. Electron Phys. VII:253 (1955).
58. J. L. Vossen and J. J. Cuomo, 'Thin film Processes', J. L. Vossen and W. Kern, Eds., Academic Press, New York, (1978), Chapter II-1.
59. Edgar Alfonso, Jairo Olaya and Gloria Cubillos, 'Crystallization-Science and Technology', Edited by Marcello Rubens Barsi Andreeta, Chapter-15, p-398, (2012).
60. P.J. Kelly, R.D. Arnell, 'Magnetron sputtering: a review of recent developments and applications', Vacuum 56 (2000) 159-172.
61. J.A. Thornton and A.S. Penfold, "Cylindrical Magnetron Sputtering," in Thin Film Processes, edited by J.L. Vossen and W. Kern, Academic Press, NY 1978.
62. D. Depla, S. Mahieu, J. E. Greene, 'Sputter Deposition Process'.

63. J. Thornton, 'Influence of apparatus geometry and deposition conditions on the structure and topography of thick sputtered coating', J. Vac. Sci. Technol., Vol. 11, (1974) 666-670.
64. L.G. Christophourou, Atomic and Molecular Radiation Physics, Wiley-Interscience, New York (1971) 6.
65. L.G. Christophorou, D.L. McCorckle, A.A. Christodoulides, in: L.G. Christophorou (Ed.), Electron–Molecule Interactions and their Applications, Vol. 1, Academic Press, New York (1984).
66. E. Stoffles, W.W. Stoffels, D. Vender, M. Haverlag, G.M.W. Krosen, F.J. DeHoog, Contrib. Plasma Phys. 35 (1995) 331.
67. Y. Itikawa, A. Ichimura, K. Onda, K. Sakimoto, K. Takayanagi, Y. Hatano, M. Hayashi, H. Nishimura, S. Tsurubuchi, J. Phys. Chem. 18(1) (1989) 23.
68. The behavior of free and attached electron in oxygen, J. A. Rees, Australian Journal of Physics, 18(1), 41-58, 1965.
69. http://www-inst.eecs.berkeley.edu/~ee143/fa10/lectures/Lec_12.
70. R. M. A. Azzam and N. M. Bashara, Ellipsometry and Polarized Light, North-Holland, Amsterdam (1977).
71. H. G. Tompkins and W. A. McGahan, Spectroscopic Ellipsometry and Reflectromety: A User's Guide, John Wiley & Sons, Inc., New York (1999).
72. H. G. Tompkins and E. A. Irene, Eds, Handbook of Ellipsometry, William Andrew, New York (2005).
73. Hiroyuki Fujiwara, 'Spectroscopic Ellipsometry: Principles and Applications', John Wiley and Sons Ltd., England (2007).
74. William A. McGahan, Blaine Johs and John A. Woollam, 'Techniques for ellipsometric measurement of the thickness and optical constants of thin absorbing films', Thin Solid Films, 234 (1993) 443-446.
75. Mathias Schubert, 'Infrared Ellipsometry on Semiconductor Layer Structures: Phonons, Plasmons, and Polaritons', STMP 209, 1–6 (2004).
76. CompleteEase Data Analysis Manual, J. A. Woolam Co., Inc.
77. V. Holy, J. Kubena, I. Ohlidal, K. Lischka and W. Plotz, 'X-ray reflection from rough layered systems', Physics Review B, Volume 47, 15896 (1993).
78. L. G. Parrat, 'Surface Studies of Solids by Total Reflection of X-Rays' Phys. Rev. 95, 359 (1954).
79. Miho Yasaka, 'X-Ray Thin Film Measurement Techniques', The Rigaku Journal, 26(2), 2010.
80. Heinz Kiessig, "Interferenz von Röntgenstrahlen an dünnen Schichten" ANNALEN DER PHYSIK, 5. FOLGE, 1931, BAND 10, HEFT 7.
81. https://en.wikipedia.org/wiki/X-ray_reflectivity.
82. Rontgen's discovery of X-ray – The British library.
83. W.L. Bragg, "The Diffraction of Short Electromagnetic Waves by a Crystal", Proceedings of the Cambridge Philosophical Society, 17 (1913), 43–57.
84. Bruce C. Gates, Helmut Knoezinger, Friederike C. Jentoft. 'Advances in Catalysis', Volume 52, 1st edition, p298. (2009)
85. http://pd.chem.ucl.ac.uk/pdnn/peaks/size.htm

86. A.R.Stokes & A.J.C.Wilson, The diffraction of X-rays by distorted crystal aggregates; Proc. Physical Soc., 1944, 56, 174-181.
87. L. B. Valdes, 'Resistivity Measurements on Germanium for Transistors', Proc. I. R. E. 42, p. 420-427, (1954).
88. I. Miccoli, F. Edler, H. Pfnur, C. Tegenkamp, 'The 100th anniversary of the four-point probe technique: the role of probe geometries in isotropic and anisotropic systems', Journal of Physics, vol. 27, Number 22, (2015).
89. Brian Jones, ''Resistance measurements on play-doh TM,'' Phys. Teach. 31, 48–49 (1993).
90. Andrew P. Schuetze, Wayne Lewis, Chris Brown, and Wilhelmus J. Geerts, 'A laboratory on the four-point probe technique', Am. J. Phys. 72 (2), (2004).
91. Yadunaath Singh, 'Electrical Resistivity Measurements: A Review', International Journal of Modern Physics: Conference Series Vol. 22 (2013) 745–756.
92. M. Billardon, J Badoz, C. R. Acad. Bc. Paris 262, 1672 (1966).
93. Katsuaki Sato, Jpn. J. Appl. Phys. 20, 2403-2409 (1981).
94. William P. Van Drent, Takao Suzuki, IEEE Trans. Magn. 33, 3223-3225 (1997).
95. Baoliang (Bob) Wang, Jennifer List, Proc. of SPIE 5888, 438 (2005).
96. Baoliang (Bob) Wang, Emily Hinds, Erica Krivoy, Proc. of SPIE 7461, 746110-1 (2009).
97. Linda Hirschy, Bialong (Bob) Wang, Jacob Wolf, Bob Lakanen, Brittany Hartmann, Proc. of SPIE 8486, 848619-1 (2012).
98. G.A. N. Connell, D. Treves, R. Allen, M. Mansuripur, Appl. Phys. Lett. 42, 742-744 (1983).
99. Katsuaki Sato, Takayuki Ishibashi, IEEF T. Electr. Electr. 3, 399-403 (2008).
100. D. P. Shelton, Ruth E. Cameron, Rev. Sci. Instrum. 59, 430-433 (1988).
101. Arjun Joshua, V. Venkataraman, Rev. Sci. Instrum. 80, 023908-1 – 023908-6 (2009).
102. N.F. Borelli, R.A. Miller, Applied Optics 7, 745-750 (1968).
103. Theodore C. Oakberg, Proc. of SPIE 2265-192, 182 (1994).
104. Ernst Polnau, Hans Lochbihler, Opt. Eng. 35, 3331-3334 (1996).
105. T. C. Oakberg, Opt Eng. 34, 1545-1550 (1995).
106. S. Polisetty, J. Scheffler, S. Sahoo, Yi. Wang, T. Mukherjee, Xi He, Ch. Binek, Rev. Sci. Instrum. 79, 055107-1 – 055107-6 (2008).
107. Patrick Holland, Mary Kempton, Dustin Ragan, Steve Rios, Anup K. Bandyopadhyay, Archana Dubey, Wilhelmus J. Geerts, J. Magn. Magn. Mat. 250, L1-L5 (2002).
108. Claude Garrett, Patrick Holland, Wilhelmus J. Geerts, Dustin Ragan, Archana Dubey, Steve Rios, Anup K. Bandyopadhyay, J. Appl. Phys 93, 8624-8626 (2003).
109. M. Cormier, J. Ferre, A. Morigin, J. P. Crombieres, V. Klein, Rev. Sci. Instrum. 79, 033706-1 – 033706-6 (2008).
110. "Development of a scanning modulating Magneto-Optical Kerr Microscope", H.W. ten Brinke, technical report internship Texas State University (2004).

111. Jeroen Schoenmaker, Antonio Domingues dos Santos, Anotio Carlos Seabra, Yves Souche, Jean Pierre Jamet, Andre Thiaville, Jacques Ferre, J. Appl. Phys. 98, 086108-1 – 086108-3 (2005).
112. M. Savoini, F. Ciccacci, L. Duo, M Finazzi, Rev. Sci. Instrum. 82, 023709-1 – 023709-4 (2011).
113. J. Gray, P. Thomas, X.D. Zhu, Rev. Sci. Instrum. 72, 3714-3717 (2001).
114. J.C. Kemp,"Piezo-Optical birefringence modulators: New use for a long-known effect," J. Opt. Soc. Am. 59,950-954(1969).
115. K.W. Hipps and G. A. Crosby, J. Phys. Chem. 83, 555-562(1979).
116. Eugene Hecht, Optics, ISBN 0-8053-8566-5-90000.
117. Roy M. Waxler, G.W. Cleek, J. Res. Natl. Stand. Sec A 77A, 755-763 (1973).
118. Md Abdul Ahad Talukder, Wilhelmus J. Geerts, AIP Advances 7, 056719-1 through 6 (2017).
119. Fidele Twagirayezu, Thesis Texas State University San Marcos, Texas, July 2017.
120. J. C. Cotteverte, B. Bretenaker, and A. Le Floch, Appl. Opt. 30, 305-311 (1991).
121. Jerome Poirson, Thomas Lanternier, Jean-Charles Cotteverte, Albert Le Floch, Fabien Bretenaker, Appl. Opt. 34 6806-6818 (1995).
122. S. Rubin, T.O. Passell, E. Bailey, "Chemical Analysis of Surfaces by Nuclear Methods", Analytical Chemistry 29, p. 736(1957).
123. M. Nastesi, J. W. Mayer, Y. Wang, "Ion Beam Analysis Fundamentals and Applications", Chapter 5, p. 57, (2015).
124. M. Mayer, "Rutherford Backscattering Spectroscopy (RBS)", Workshop on Nuclear Data for Science and Technology, (2003).